CHALMERS
UNIVERSITY OF TECHNOLOGY

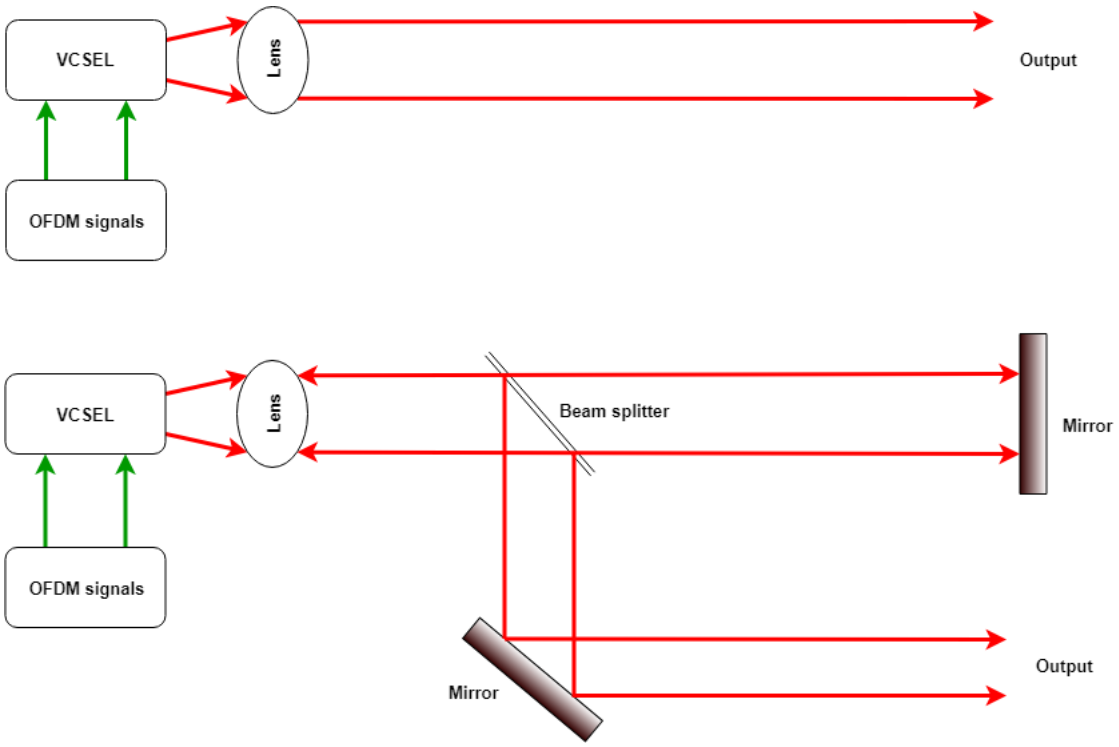

Investigation into the VCSEL nonlinearity in a RoF system and possible techniques of suppression

Master's thesis in Wireless Photonics and Space Engineering

Ghaiath Altrabulsi

Department of Some Subject or Technology
CHALMERS UNIVERSITY OF TECHNOLOGY
Gothenburg, Sweden 2019

Master's thesis 2019:09

Investigation into the VCSEL nonlinearity in a RoF system and possible techniques of suppression

GHAIATH ALTRABULSI

CHALMERS
UNIVERSITY OF TECHNOLOGY

Department of Microtechnology and Nanoscience - MC2
Photonics department
Chalmers University of Technology
Gothenburg, Sweden 2019

Investigation into the VCSEL nonlinearity in a RoF system and possible techniques of suppression
GHAIATH ALTRABULSI

Supervisor: Mark Holm, Huawei Gothenburg
Examiner: Anders Larsson, Department of Microtechnology and Nanoscience - MC2

Master's Thesis 2019:09
Department of Microtechnology and Nanoscience - MC2
Photonics department

Chalmers University of Technology
SE-412 96 Gothenburg
Telephone +46 31 772 1000

Cover: Optical feedback into VCSEL as a technique to suppress the nonlinearity.

Gothenburg, Sweden 2019

Investigation into the VCSEL nonlinearity in a RoF system and possible techniques of suppression.

GHAIATH ALTRABULSI

Department of Microtechnology and Nanoscience - MC2
Chalmers University of Technology

Abstract

The mobile communication networks in 5G and beyond aim to provide better reliability, improve the coverage, and increase the communication speed. The number of users increases drastically. In 5G, the number of base stations, called Transmission Reception Point (TRP) in 5G, will increase dramatically, and smaller sells will be used. The central station (CS) must be placed in an easily accessible and securely maintained location. Implementing this scenario will increase the cost rapidly and would be challenging to manage, troubleshoot, and monitor. As an alternative, the central station can be placed in a central location and can be accessed easily. Only the TRP will placed in the location. The TRP then should be connected to the central station using Radio over Fiber (RoF) links. The TRP unit should be as simple as possible since this will lower the cost and increase the reliability.

Orthogonal Frequency Division Multiplexing (OFDM) has been chosen as the main waveform to be implemented in 5G as a transmission technique. OFDM is compatible with Multiple Input Multiple Output (MIMO), which is the key factor in the new generation communication systems. The large bandwidth and spectrum allocation of OFDM are suitable for 5G requirements. However, the bandwidth of the wireless systems is still limited compared with very high bandwidth that can an optical transmission link provide.

Since the bandwidth of 5G antennas is very wide, it is possible to send multiple technologies in the same fiber link from the central station to the TRP unit. For instance, in the same link, WiMax, WiFi, 4G, and 5G signals can be transmitted simultaneously. In the TRP unit, all these signals can be optically received and wirelessly retransmitted at the same time. This approach will reduce costs dramatically, increase the reliability, and reduce the need to monitor and maintain each technology separately.

In the previous approach, a reliable light source that can provide high-speed rate is crucial. The best candidate in this situation would be the Vertical-Cavity Surface-Emitting-Laser (VCSEL). VCSEL has many advantages such as low fabrication and packaging costs, high performance, high efficiency, easy fiber coupling, and large modulation bandwidth.

However, VCSELs have some disadvantageous such as polarization instability, which is sometimes known as polarization switching, low output power, relative noise in-

tensity, and nonlinearity. Sending multiple signals into the same optical system (transmitter, fiber link, and photodetector) will create unwanted harmonics which will deteriorate the analogue performance drastically. The primary source of nonlinearity in the Rof link of is the VCSEL. The second-order harmonic distortion and third-order intermodulation distortion are considered to be the main drivers of nonlinearity inside the VCSEL.

To suppress the nonlinearities in the VCSEL or come around it. Multiple workarounds have been proposed. Different VCSELs have different harmonic distortion minima at different frequencies and different temperatures. Planing each OFDM signal to fall into the distortion valley will relieve the effect of the distortion on the signal. Another workaround is inherited from the WDM technology where each OFDM signal can be sent in one VCSEL in the VCSEL array.

Another solution is the selective optical feedback where a fraction of the output power injected back into the VCSEL after changing the polarization of the reinjected signal. This solution shows to be a good approach to suppress the nonlinearities related to polarization instability in VCSEL.

It has been shown that harmonic distortions strongly depends on the type of the polarization that injected back into the VCSEL since the Parallel Optical Feedback (POF) will increase the distortion and create new harmonics at higher frequencies. However, Orthogonal Optical Feedback (OOF) will suppress the harmonic distortion strongly.

Keywords: Orthogonal Frequency Division Multiplexing (OFDM), Radio over Fiber (RoF), Vertical-Cavity Surface-Emitting-Laser (VCSEL), VCSEL nonlinearity, Selective Optical Feedback (SOF).

Acknowledgements

I would like to thank my colleagues and especially to my supervisor Mark Holm and Ronald Nissel at Huawei Gothenburg, with whom I had great discussions and who were of a great help to complete this thesis. Thanks to all friends and family who were supporting me along the way!

Ghaiath Altrabulsi, Gothenburg, Septemper 2019

Acronyms

CS Central Station. v

MIMO Multiple Input Multiple Output. v

OFDM Orthogonal Frequency Division Multiplexing. v, vi
OOF Orthogonal Optical Feedback. vi

POF Parallel Optical Feedback. vi

RoF Radio over Fiber. v

TRP Transmission Reception Point. v, 3

VCSEL Vertical-Cavity Surface-Emitting-Laser. v

Contents

List of Figures

List of Tables

1
Introduction

Over the last 100 year, technology change has dramatically increased. Without any effort, people can contact with friends, sending photos/videos, watch an Ultra High Definition (UHD) movie in a train traveling at a speed of 150 km/h and streams 4K video game where millions see it simultaneously. GPS has become an essential part of our ability to navigate. All you need is a smartphone and internet access. These benefits are attracting more and more users every day. In 2018, 240 million new users had applied for mobile broadband services around the globe [1]. By the year 2024, the number of mobile broadband expected to increase to 8.4 million broadband subscriptions. Total traffic expected increased from 27 exabytes to 136 exabytes per month [1].

1.1 Orthogonal Frequency Division Multiplexing (OFDM)

FDM multiplexing is a method that allow multiple users to share one link by dividing available bandwidth into different non-overlapping sub-channels. Orthogonal Frequency Division Multiplexing (OFDM) as a variation of FDM. OFDM is a very popular multiplexing method used in many of the latest wireless and telecommunication standards such as Wi-Fi 802.11ac, 4G and 5G cellular phone technologies, WiMAX, satellite and many others. A guard band which is a narrow frequency range is inserted between adjacent sub-channels so that different signals travel separately and simultaneously without interfering with each other.

The Orthogonal frequency-division multiplexing (OFDM) belongs to the multicarrier modulation (MCM) family where the high data rate converted into multiple parallel pipes that have a lower data rate. Data in each pipe is carried over many subcarriers. The most important advantages of the OFDM are the robustness against the channel dispersion, and the channel estimation is relatively simple in the time varying environment.

In OFDM on the other hand, those sub-channels are closely spaced. Not only there is no guard band between them but actually they are overlapped. In the same available bandwidth, OFDM would allow more data transmissions than FDM.

OFDM will combine all channels closely together in a way they are orthogonal to each other. Orthogonality means the two or multiple channels act independently

so any neighbour signals in OFDM operate without dependence on, or interference with one another.

For instance, If there are three signals, when the middle signal reaches its peak, its two neighbor signals are at the zero point or null. The same is true for other signals. Therefor, orthogonal signals are multiplexed in a way that the peak of one signal occurs at null of the other neighbour signals.

At the receiving end, the de-multiplexer would separate incoming subcarriers based on this orthogonal feature. OFDM would better utilize available bandwidth, and thus offer high data transmission rate than FDM.

1.2 Vertical-Cavity Surface-Emitting-Laser (VCSEL)

The first Vertical-Cavity Surface-Emitting-Laser (VCSEL) was demonstrated in 1979 where GaInAsP/InP were used as an active region. VCSELs have a lot of electrical and optical properties that give advantages over other types of semiconductor lasers such as low threshold current, thigh modulation bandwidth, simple array integration and longitudinal single mode emission. Small beam divergence make the coupling efficiency to fiber very high. There are several other properties such as circular light mode, small switching transients, symmetrical output beam profile and very low power consumption [38].

VCSELs have some disadvantageous as well, the major drawback of the VCSEL is the complex transverse modal behaviour since at higher pump rates, higher order transverse mode are supported inside the cavity due to the two dimensional extension of the mirrors.

1.3 Radio-over-fiber systems (RoF)

Radio-over-Fiber (RoF) means to modulate the optical carrier with an RF signal to transmit over an optical fiber network. RoF gives many advantages compared to fully wireless systems such as large bandwidth,low loss, resistance to electromagnetic interference, reduced power consumption and improved security. RoF is considered to be a promising candidate to reduce the deployment and maintenance costs of the wireless systems and provide low power and large bandwidth at the same time.

Transmitting radio signals in an optical fiber is not a very new technology since using fibers to distribute radio communication signals was first mentioned in 1990 [2][3]. Utilizing optical fibers in order to distribute radio communication signals has gained attraction and nowadays, it is used in many applications and areas such as terahertz spectroscopy, electronic warfare and radio signal distribution [4]. The natural property of the fiber with very wide bandwidth and relatively low loss will

allow to distribute high-frequency radio signals over long distances.

This technique can simplify the base station unit by moving the main complex operations to the central core unit, which in turn communicate to multiple base-stations [5]. In a RoF system, the electrical radio signal modulates an optical source, then the signal is transmitted in an optical fiber to the remote unit, where the optical signal is converted back into an electrical signal using a photodetector. The optical fiber links provide a very low interference and attenuation communication medium. There are many different variants of RoF, and each has advantageous and disadvantageous. The most three most common implemented RoF setups are: Analog-Radio-over-Fiber, Digital-Radio-over-Fiber, and Sigma-Delta-over-Fiber.

In figure 1.1, we can see that the fiber optic link connects the central station to the Transmission Reception Point (TRP), and then a short radio link connects the RAP to the users [26]. The RF signal is a real analog signal that get modulated using a digital signal, in our case here, it is an OFDM signal. One more advantage of using Radio over fiber is to prepare the complex signal in the central station and then send it to the TRP unit using fibers. This will simplify the TRP unit since in the 5G, it is tended to use more peripherals in order to provide high rate and making the TRP simple will make it easier to implement, troubleshoot and decrease power consuming.

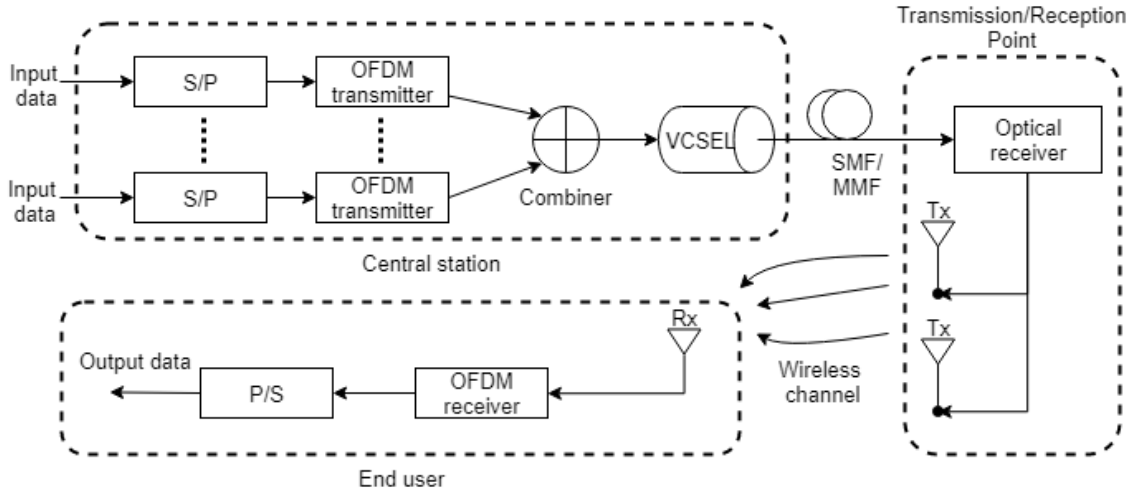

Figure 1.1: Radio-over-fiber system

RoF technology gets more interesting in 5G. There are two factors expected to be fundamental parts of 5G networks, increased number of small cells and rise of massive multiple-input multiple-output (MIMO) antennas [25].
Right now, each cell has its own base station. The moving to small cells means more base stations. Central station must be placed in a easily accessible and securely maintained location. Implementing this small cell scenario will increase the cost rapidly and would become difficult to manage, troubleshoot and monitor. The TRP unit then should be connected to the central station using a radio over fiber link. The TRP should be as simple as possible since this will lower the cost and gives

more reliability. The previous design can help to cover some difficult access places such as shopping mall, subways railways stations, airports or any place where there is insufficient coverage from the main outside cell.

1.4 A motivation to this work and outline of the thesis

The requirements on the optic link can be differ according to application. Designing the optic link should take into account the maximum transmitted signal power, acceptable link loss and minimum received power.
The light source used in the TRP unit is vertical-cavity surface-emitting laser (VCSEL) since some of its major advantages are low fabrication and packaging costs, high performance, high efficiency and large modulation bandwidth.
Low cost, high performance links can be constructed by assembling the fiber optic RF links using VCSELs with multimode fibers.

1.5 Simulation software

The software used in this thesis were combination between Matlab and OptiSystem from OptiWave. OptiSystem was chosen firstly because it is easy to build an optical link and it has a component that can run a snippet of Matlab code along with the simulation. However, Visualization and extracting data from it was a bit difficult. By help of Matlab, it was easier to manipulate with data and get better visualization results.

2
OFDM

2.1 OFDM principles

OFDM is a modulation method to encode digital data on multiple carrier frequencies. High spectral efficiency, efficient implementation and resistance against the inter-symbol interference (ISI) are main advantages that OFDM can provide. However, OFDM is sensitive to frequency and phase offset problems and it has high peak-to-average-power ratio (PAPR).

2.1.1 Single-carrier (SC) vs Multi-carrier (MC)

As all other transmission techniques, OFDM has two main problems in general. It has high PARR (Peak to Average Power Ratio) and it is very sensitive to phase and frequency noises. Although all benefits OFDM comes with and widely been implemented, there still a debate regarding whereas to use a single-carrier or multi-carrier. In optical domain, the debate is slightly different since in the single-carrier systems, a simple architecture is employed where discrete digital level modulation is fed into an QPSK modulator and I and Q signals component generated. Moreover, the information coded in the time domain, where in Coherent Optical OFDM (CO-OFDM), the information is encoded in frequency domain. The CO-OFDM transmitter include DSP module and DACs to generate a complex OFDM signal. The information is encoded into each individual sub-carrier [14]. Figure 2.1 presents the transmitter for both CO-OFDM and single-carrier systems.

Based on these two differences, a comparison of some key properties:

Ease of signal processing: Ability to communicate coherently can be done by channel estimation and signal estimation since in OFDM, we use pilot symbols. But in SC, a blind estimation is done using some decision feedback.

Higher order modulation: The CO-OFDM transmitter is more complex than Single carrier transmitter, but as long as we increase the modulation order more than 2, complexity in CO-OFDM does not scale that much compared with single-carrier transmitter.

Tight bounding of spectral components: As known, the OFDM spectral is tight and this gives more tolerance to the filter narrowing effect. The OFDM spectrum is rectangular-like spectrum and as long as the filter is wider, there will not

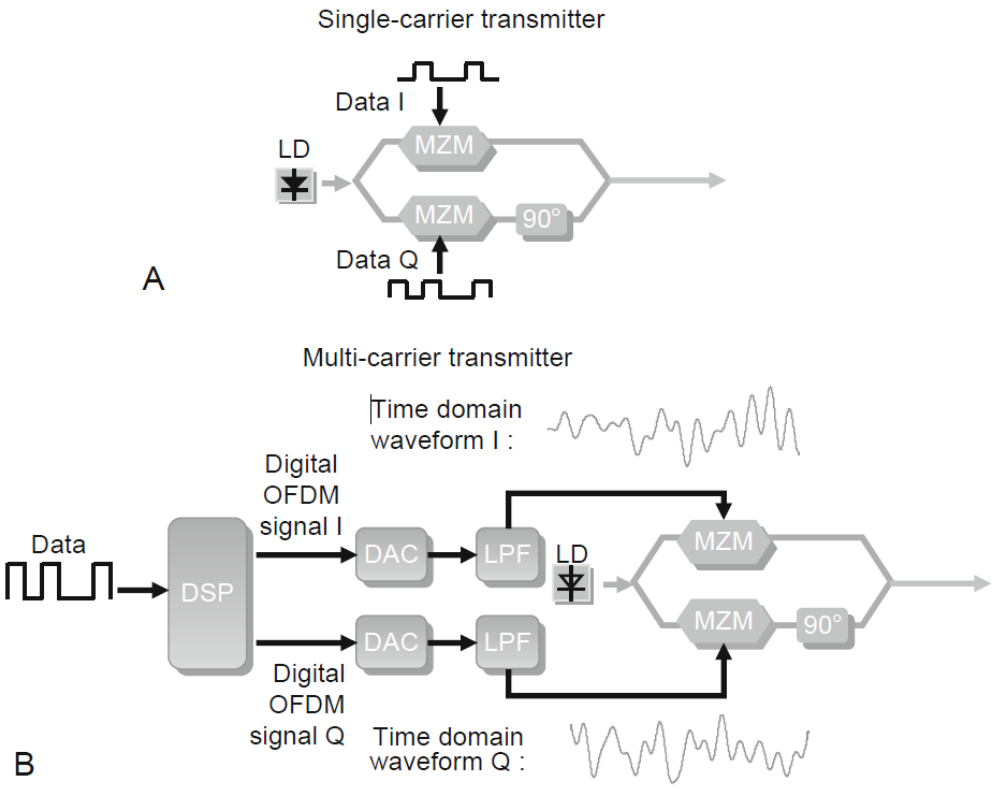

Figure 2.1: Transmitter architecture for (a) single-carrier systems and (b) multicarrier systems.

be any penalty on the OFDM signal.

Bandwidth scalability: Because the CO-OFDM signal generated in frequency domain, it is much easier to process the data in each sub-bands separately [6][7]. Practically, if we could guarantee the orthogonality between the adjacent bands, there will be no need for a frequency guard band, so no sacrifice in the spectral efficiency [6]. The single-carrier on the other hand do the encoding across the whole spectrum and this make it impossible to scale down the bandwidth.

Sub-wavelength bandwidth access for performance monitoring and multiaccess/multicast networks: Placing the DSP in the transmitter will give advantage in CO-OFDM since in CO-OFDM, there is a flexibility to allocate specific subcarriers for performance monitoring and channel estimation which is considered as an attractive feature in CO-OFDM.

Computation complexity: Chip design complexity and power computation depends a lot on the computation complexity. In the signal-carrier systems where IFFT/FFT is used, the computation complexity scales with N_x:

$$C_{\text{bit}} \propto \log_2 (N_{\text{sc}}) , N_{\text{sc}} = \alpha \cdot D \cdot B \tag{2.1}$$

Where N_x is the channel length, N_{sc} is the number of subcarriers in CO-OFDM and C_{bit} is number of multiplications required per bit. In case the signal-carrier system

	Mathematical Model	Nonlinearity	Speed
Wireless OFDM	Time domain multiple discrete Rayleigh fading	None	Can be fast for mobile environment
Optical OFDM	Continuous frequency domain dispersion	Significant	Medium

Table 2.1: Comparison between Wireless and Optical Channels

based on FIR equalization, the computation complexity scales as [8][9]:

$$C_{\text{bit}} \propto D \cdot B^2 \tag{2.2}$$

Sampling rate: It is always recommended to have sampling rate to be twice the signal band rate in single-carrier system since it is sensitive to sampling phase inaccuracy [10][11]. The oversampling is done by not filling the edge subcarriers in the CO-OFDM systems, that is why it is sufficient to oversample with $10-20\%$ [12][13].

Tolerance to the component imperfection: At high speed bit rate, > 100 Gb/s, the power amplifiers, ADC/DAC and IQ modulator quality will deviate from their perfect. The imperfection in CO-OFDM can be compensated and estimated using the signal processing in the transmitter and the receiver. The single-carrier system on the other hand depending on the drive voltage operating at the saturation and this make it is difficult to estimate and mitigate the imperfection [14]

Bit and power loading: The frequency domain can effectively manipulated using the CO-OFDM at the transmitter since this advantage can be more emphasized when the RF communication channel suffer from deep fading or a part from the spectrum notched out because of the severe multipath interference.

2.1.2 The Difference between RF OFDM and Optical OFDM Systems

It is a kind of mistake to make a direct one-to-one translation from the RF OFDM to the optical OFDM. There is a uniqueness of the optical channel along with the optical components at the transmitter and receiver ends. In the table 2.1, a general comparison between wireless and optical channels has been done.

2.2 Basic concepts

2.2.1 Mathematical presentation for OFDM signal

As mentioned before, the OFDM is a spacial case of the MCM class, In the figure 2.2, a generic implementation of the MCM system is depicted. The IQ modulator/demodulater is a common-used components in the MCM systems, the transmitted signal $s(t)$ give by:

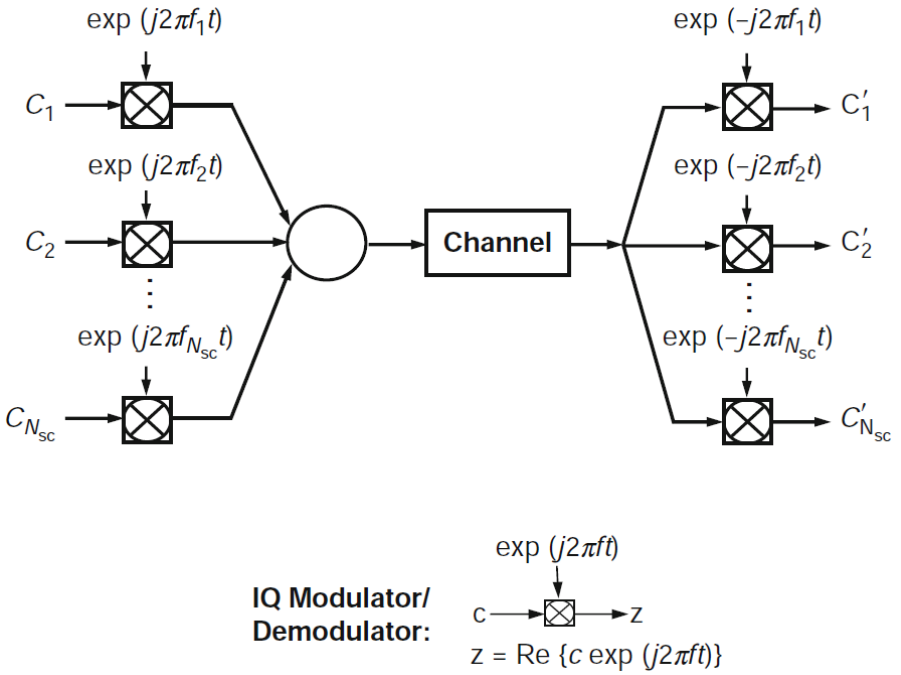

Figure 2.2: Conceptual diagram for a generic multicarrier modulation system.

$$s(t) = \sum_{i=-\infty}^{+\infty} \sum_{k=1}^{N_\infty} c_{ki} s_k \left(t - iT_\mathrm{s}\right) \tag{2.3}$$

$$s_k(t) = \Pi(t) e^{j2\pi f_k t} \tag{2.4}$$

$$\Pi(t) = \begin{cases} 1, (0 < t \leq T_\mathrm{s}) \\ 0, (t \leq 0, t > T_\mathrm{s}) \end{cases} \tag{2.5}$$

where s_k is the wave signal for the kth subcarrier, f_k is the frequency of the subcarrier, C_{ki} is the ith information symbol at the kth subcarrier, T_s is the symbol period and $\prod(t)$ is the pule shaping function.

2.2.2 Discrete Fourier Transform Implementation of OFDM

In OFDM, large number of subcarriers are needed so each transmission channel impact each subcarrier as a flat channel. This means that we need a very large number of oscillators and filters in both transmitter and receiver.
A great implementation of inverse discrete Fourier transform (IDFT)/discrete Fourier transform (DFT) can be done to modulate and demodulate the OFDM signal.
The mth sample of $s(t)$ from 2.3 equals to:

$$s_m = \sum_{k=1}^{N} c_k . e^{j2\pi f_k \frac{(m-1)T_s}{N}} \tag{2.6}$$

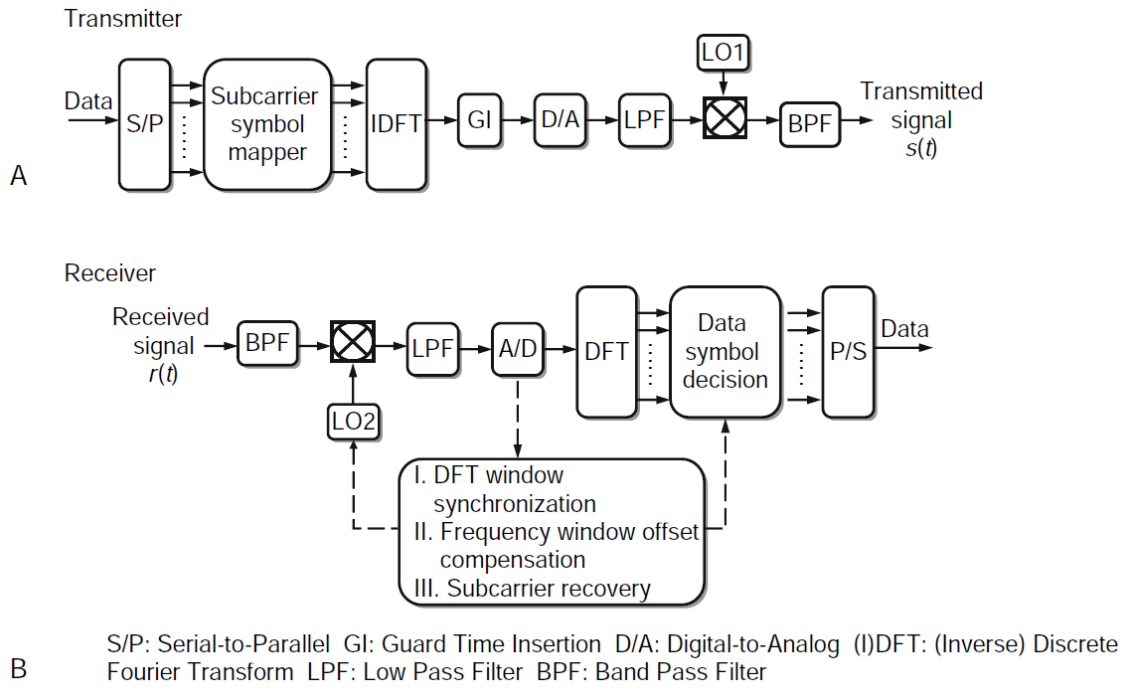

Figure 2.3: Conceptual diagram for (A) OFDM transmitter and (B) OFDM receiver

If the following condition satisfied, the two subcarriers are orthogonal to each other:

$$f_k - f_l = m\frac{1}{T_s} \tag{2.7}$$

Using the last equation, and assuming that $f_k = \frac{k-1}{T_s}$ and then substituting that in the equation 2.6:

$$s_m = \sum_{k=1}^{N} c_k . e^{j2\pi f_k \frac{(m-1)T_s}{N}} = \sum_{k=1}^{N} c_k . e^{j2\pi \frac{(m-1)(k-1)}{N}} = \mathfrak{F}^{-1}\{c_k\} \tag{2.8}$$

In the same fashion, the received information symbol c'_k can be obtained by Fourier transform the r_m:

$$c'_k = \mathfrak{F}\{r_m\} \tag{2.9}$$

Where r_m is the received signal sampled at the mth sample. The discrete value of OFDM signal s(t) is a simple N-point IDFT of the information symbol c_k, and received symbol c'_k is a simple N point DFT of the received signal. In order to implement DFT/IDFT, a digital to analog converter (DAC) is needed to convert the discrete value of s_m to continuous analog value of s(t) and an analog to digital converter (ADC) to convert the continuous signal r(t) to discrete sample r_m.

2.2.3 Cyclic Prefix

Cyclic Prefix is a very important technique in OFDM. Considering two consecutive OFDM symbols that experience a frequency selective channel with a delay t_d.

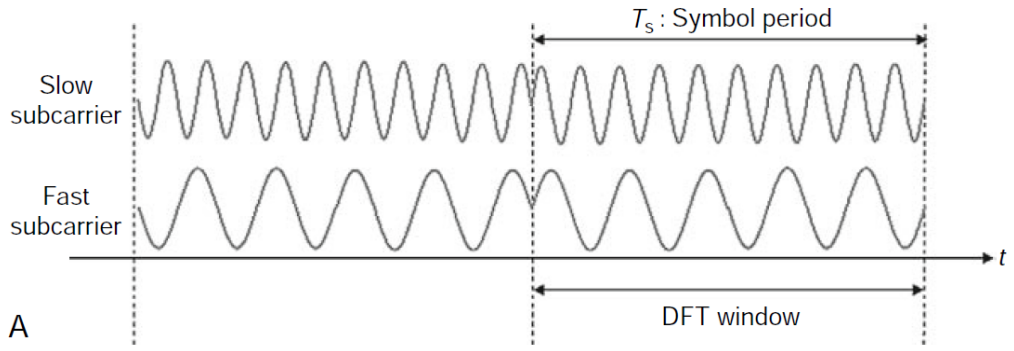

Figure 2.4: OFDM signal without cyclic prefix at the transmitter

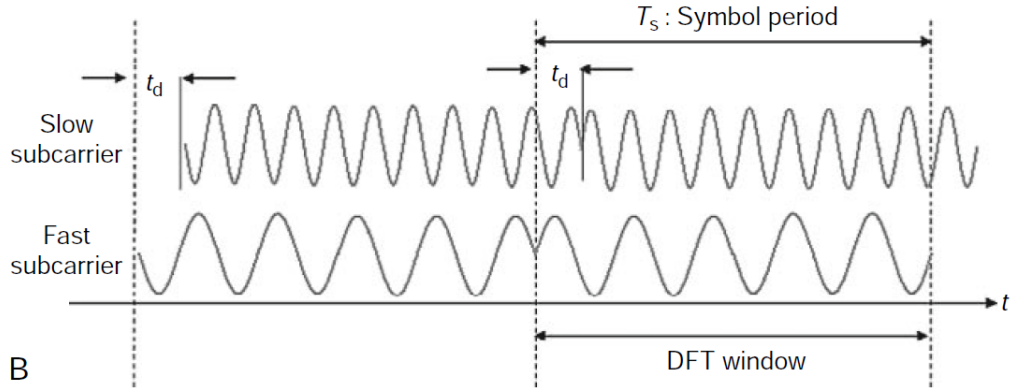

Figure 2.5: OFDM signal without cyclic prefix at the receiver

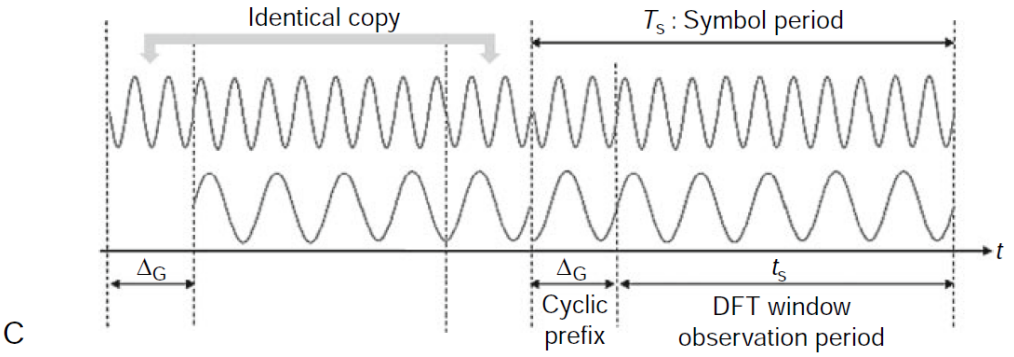

Figure 2.6: OFDM signal with cyclic prefix at the transmitter

Each of these OFDM symbols carried on only two subcarriers, one is fast and the other is slow subcarrier. within each OFDM symbol, the fast subcarrier and slow subcarrier are aligned with the transmission. Figure 2.5 shows the same OFDM signals at reception, where the slow carrier is delayed by t_d. We choose a DFT window that contains a complete OFDM symbol. Due to the channel dispersion, a part from the slow subcarrier will cross the symbol boundary, and this will lead to interference between two OFDM symbols causing Inter-Symbol-Interference (ISI) and Inter-Carrier-Interference (ICI) [15][16].

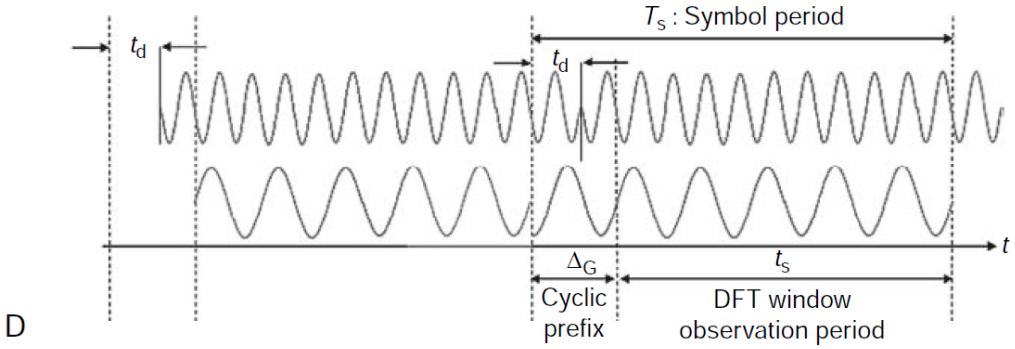

D

Figure 2.7: OFDM signal with cyclic prefix at the receiver

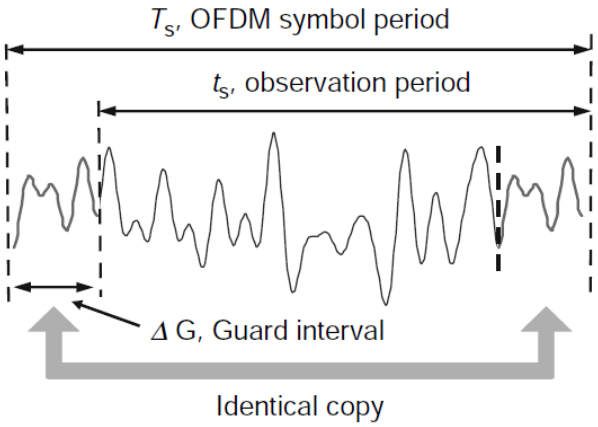

Figure 2.8: The time domain OFDM signal for one complete OFDM symbol

To get rid of ISI and ICI resulted from channel dispersion, a periodic prefix was proposed. Figures (2.4,2.5,2.6,2.7) show how cyclic prefix works. First we extend the OFDM wave into the guard interval Δ_G. The part of waveform is an identical copy of that in the DFT period but shifted forward by t_s. Figure 2.7 shows the cyclic prefix at the receiver. We choose the cycle prefix period to be larger than the maximum possible delayed subcarrier. So we prepending a copy of the last samples from the end to the beginning of the OFDM signal. At the receiver end, when the signal is demodulated, the N-points FFT will come always after the cyclic prefix.

In order to restore the OFDM signal in a good way, we have to select an appropriate DFT window and estimate the phase shift for each subcarrier.
To include the cyclic prefix in the transmitted signal s(t), pulse shape function need to be updated as following:

$$\Pi(t) = \begin{cases} 1, (-\Delta_G < t \leq t_s) \\ 0, (t \leq -\Delta_G, t > t_s) \end{cases} \tag{2.10}$$

The time domain OFDM signal is depicted in the figure 2.8 where it can be seen that one complete OFDM symbol that consists of the cyclic prefix and the observation period. Only the waveform inside the observation period will be used to recover the information symbols in the frequency domain.

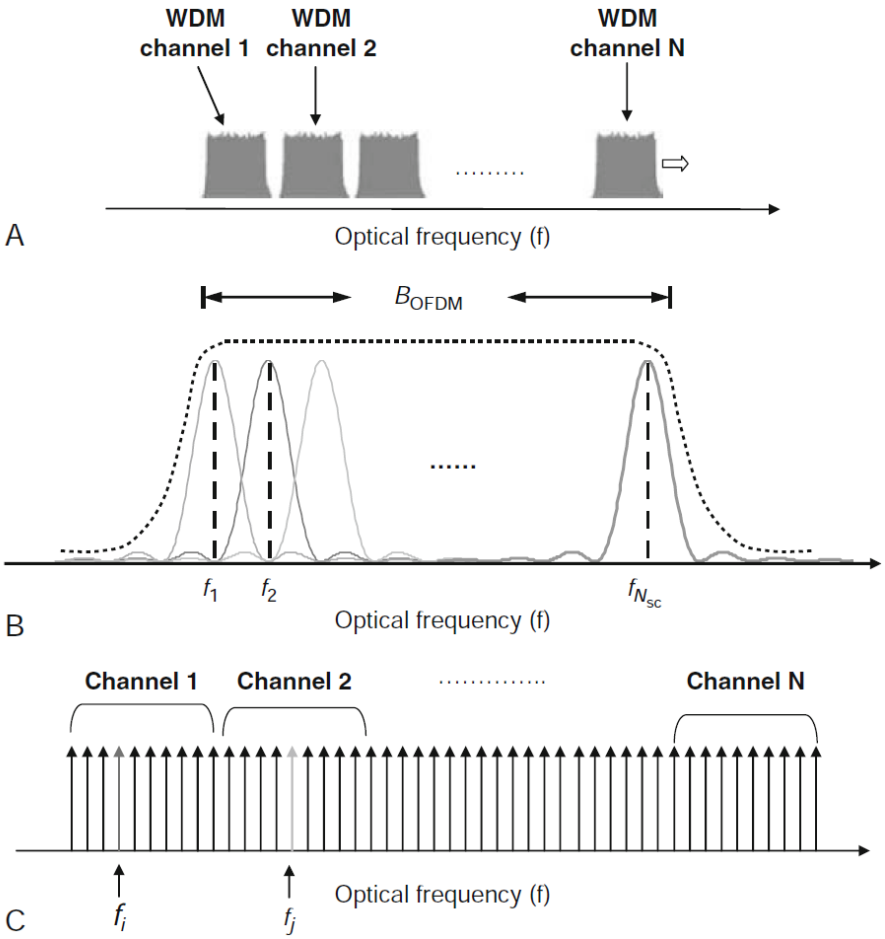

Figure 2.9: Optical spectra for (A) N wavelength-division multiplexed (WDM) CO-OFDM channels, (B) zoomed-in OFDM signal for one wavelength, and (C) cross-channel OFDM (XC-OFDM) without guard band.

2.2.4 Spectral Efficiency for Optical OFDM

In the optical domain, the optical spectral efficiency for OFDM is different from the RF spectrum since it depends on the implementation. In CO-OFDM systems, the number of subcarriers transmitted in each OFDM symbol is N_{sc}. Thus, the total CO-OFDM symbol rate R is given by:

$$R = N_{sc}/T_s \tag{2.11}$$

where T_s is the OFDM symbol period. The figure 2.9 shows the optical spectrum for every wavelength channel in the WDM. The OFDM bandwidth B_{OFDM} is then:

$$B_{OFDM} = \frac{2}{T_s} + \frac{N_{sc} - 1}{t_s} \tag{2.12}$$

t_s is the observation period. Introducing the bandwidth efficiency of OFDM η:

$$\eta = 2\frac{R}{B_{\mathrm{OFDM}}} = 2\alpha, \quad \alpha = \frac{t_{\mathrm{s}}}{T_{\mathrm{s}}} \tag{2.13}$$

The factor 2 in the equation 2.13 accounts for the vertical and horizontal polarizations in the fiber. The typical value of α is 8/9, then the optical spectral efficiency factor η is 1.8 Bd/Hz. This gives 3.6 bit/s/Hz if QPSK is used for each subcarrier. Higher order modulation will give better spectral efficiency [17][18].

2.2.5 Complex and Real Representations of an OFDM Signal

The baseband OFDM signal has a complex value at the very beginning and very end of the transmitter and receiver. In between and during the transmission, the OFDM signal becomes purely real signal. This happen when the upconversion and downconversion is done. This up/down conversion can be done using a mixer or an IQ modulator/de-modulator. The transmitted RF signal can be written as:

$$S_{\mathrm{RF}}(t) = \mathrm{Re}\left\{S(t)e^{j2\pi f_{\mathrm{RF}}t}\right\} = \mathrm{Re}\{S(t)\} \cdot \cos(2\pi f_{\mathrm{RF}}t) - \mathrm{Im}\{S(t)\} \cdot \sin(2\pi f_{\mathrm{RF}}t) \quad (2.14)$$

$S_{RF}(t)$ here is a real value signal. The carrier frequency here is f_{RF}. IQ modulator can be presented using two RF mixers and Local oscillators with 90 degree phase shift as can be seen in figure 2.10.

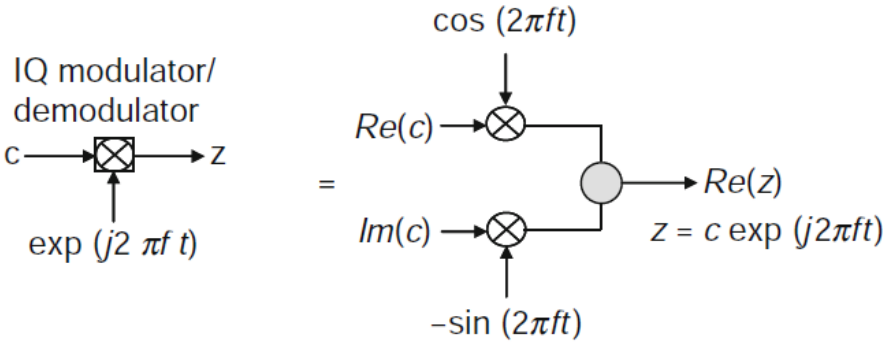

Figure 2.10: IQ modulator for upconversion of a complex-valued baseband signal c to a real-valued passband signal z. The downconversion follows the reverse process by reversing the flow of c and z.

The downconversion of the OFDM signal follow the reverse process where the conversion from the real to complex occur. The baseband c and passband signal z. Both the upconversion and downconversion can be seen in the figure 2.10.

2.2.6 Peak-to-Average Power Ratio of OFDM Signals

One of the main drawbacks of OFDM modulation is the high PAPR. In RF domain, the main problem occurs in the power amplifiers since the amplifier gain will saturate when the input power is high. The optical amplifier (EDFA) is a linear amplifier no matter the input signal power and this is because of its slow response time, usually milliseconds, but PAPR still exist in optical fiber domain due to optical fiber nonlinearity [19][20]. The transmitted waveform for one OFDM symbol in the time domain can be written as:

$$s(t) = \sum_{k=1}^{N_{\text{sc}}} c_k e^{j2\pi f_k t}, \quad f_k = \frac{k-1}{T_{\text{s}}} \tag{2.15}$$

PAPR for OFDM is defined as:

$$\text{PAPR} = \frac{\max\{|s(t)|^2\}}{E\{|s(t)|^2\}}, \quad t \in [0, T_s] \tag{2.16}$$

Using M-PSK as a modulation format $\Rightarrow |c_k| = 1$. The maximum PAPR is $10\log_{10}(N_{sc})$ by substituting $c_k = 1$ and t = 0 in equation 2.15. If the OFDM system has 256 subcarriers, then the maximum PARR equal to 24 dB which is very high. It is very clear that PAPR of OFDM signal is very high either for RF or optical systems. PAPR reduction should be implemented. Most common PAPR reduction approaches are:

- PAPR reduction with signal distortion.
- PAPR reduction without signal distortion.

2.2.7 Frequency Offset and Phase Noise Sensitivity

Phase noise and frequency offset is one of the most disadvantages of OFDM. Both of them lead to ICI and ISI. The symbol length of OFDM is relatively long compared to the symbol length in the single carrier and this will make OFDM signal more probable to suffer from frequency offset and phase noise [21][22]. In the optical domain, phase noise is quite critical and important because the laser phase noise is relatively large. The phase noise problem become more and more critical when the modulation format gets higher in order to get high spectral efficiency modulation.

2.2.7.1 Frequency Offset Effect

Frequency offset can be solved by frequency estimation and frequency compensation. We define ICI coefficient η_m as:

$$\eta_m = \frac{\sin(\pi(m+\delta))}{\pi(m+\delta)} e^{-j\pi(m+\delta)} \tag{2.17}$$

Where $\delta = \Delta f \cdot T_{\text{s}}$ is the normalized frequency offset. ICI coefficient for two frequency offset 0 and 0.25 can be seen in figure 2.11. When $\delta = 0$ or any integer, ICI coefficient equals to zero or integer m. but when δ equals to any non-integer value, then there will be a residual value of ICI coefficient for any number of m, and this cause to finite interference from one subcarrier to any other subcarrier [14].

2.2.7.2 Phase Noise Effect

Phase noise sensitivity can be resolved by careful design of RF local oscillators that satisfy the phase noise specification requirements. Introducing the phase noise in the ICI coefficient and assuming that the frequency offset has been compensated, the the ICI coefficient becomes:

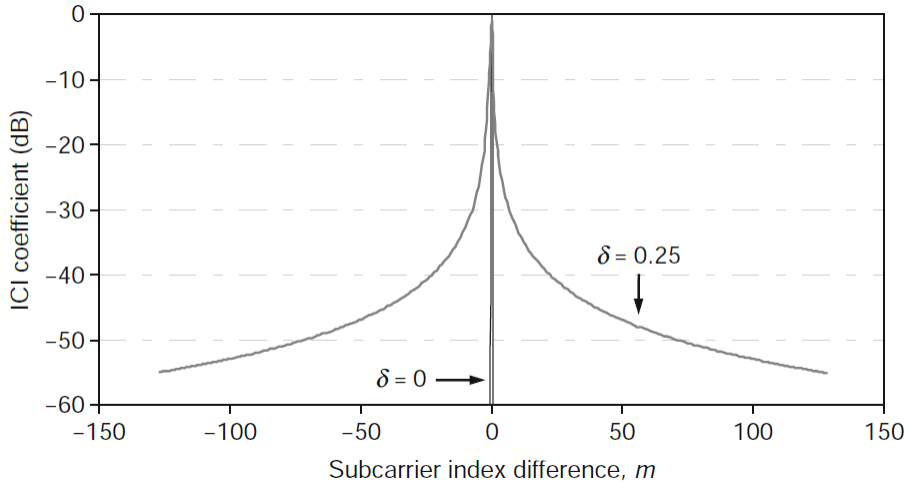

Figure 2.11: The ICI coefficient, η_m, as a function of the subcarrier index difference, m, while varying the frequency offset δ

$$\eta_m = \frac{1}{T_s}\int_0^{T_s} e^{j(2\pi' f_m t+\phi(t))}\mathrm{d}t, \quad f'_m = \frac{m}{T_s}, m = -\left(N_{sc}-1\right), \ldots, 0, 1, \ldots, N_{sc}-1 \tag{2.18}$$

where ϕ_0 is the common phase error (CPE). The major effect of phase noise is that the whole constellation diagram rotates which can be compensate by estimating and rectifying the skewed constellation using collective rotation.

2.3 Filter bank OFDM

In the 4G communication system which is also called Long Term Evolution (LTE), the waveform adopted was Cyclic Prefix OFDM, or CP-OFDM. In OFDM, frequency resource defined as subcarriers and time resource as OFDM symbols, and this provide a flexible structure for scheduling [23]. One of the most important advantageous of OFDM is that it transforms the frequency selective channel into many narrow parallel flat fading band channels which simplify the complex channel estimation. OFDM is very robust against inter-symbol interference (ISI) and inter-carrier interference (ICI) that caused by multi-path propagation with help of Cyclic Prefix (CP). OFDM can be implemented easily using fast Fourier transform (FFT) and inverse fast Fourier transform (IFFT), and due to its favorable characteristics, OFDM is widely applied in many of WiFi standards family applications and digital terrestrial broadcasting (DTB) [24].

CP-OFDM however has some drawbacks. The Cyclic Prefix (CP) decrease the spectrum and energy efficiency since CP contains no data. CP-OFDM is very sensitive to timing and frequency offsets between the subcarriers which tightening synchronization among the subcarriers. Additionally, CP-OFDM experience out of band leakage into adjacent channels and this requires wide guard band and coexistence

of different services on adjacent subcarriers becomes difficult.

As discussed before, in the fifth generation cellular communication system (5G), it is desired to enable coexistence of different services in the same transmission link. This requires a new waveform with low out of band leakage. Many waveforms are proposed such as filter bank multicarrier-offset quadrature amplitude modulation (FBMC-OQ AM), filtered OFDM (F-OFDM),universal filtered multicarrier (UFMC) and generalized frequency division multiplexing (GFDM). All previous mentioned waveforms reduce the out of band leakage nut hey have their own disadvantageous.

3

VCSEL

3.1 Vertical-Cavity Surface-Emitting Laser (VCSEL)

VCSEL was primarily demonstrated in 1979 where GaInAsP/InP used as an active region. VCSEL has a lot of electrical and optical properties that give some advantages over other types of semiconductor lasers. But first, what are semiconductor lasers and how they works.

3.1.1 Introduction to the Semiconductor lasers

In order to understand how VCSEL works, we should first understand how semiconductor lasers work in general then we take VCSEL as one type of semiconductor lasers. Semiconductor lasers are light sources where population inversion is established and they emit coherent radiation through stimulated emission of photons. Semiconductor laser used in a lot of applications such as fiber optical communications, DVD players, Blueray technology, a lot of sensing systems. The word LASER is a shortcut for Light Amplification by Stimulated Emission of Radiation. The light amplified when it propagates inside the medium where population inversion is established. The two main requirements to design a laser are an optical feedback and an optical gain.

Any laser should contains: 1- Optical gain medium where population inversion occur. 2- Optical resonator that provides the optical feedback, the most simple resonator can be designed by two plane-parallel mirrors. In figure 3.1 (a), the gain medium and optical feedback can be seen. In semiconductor laser, the active region is a direct band gap semiconductor and injecting of excess free carriers will provide population inversion.
Confinement of excess carriers can be done by surround the active region with higher band-gap material. This will also create an optical waveguide that confines the photons (guided optical mode) to the active region. The light gets amplified when it propagates along the waveguide.

Fabry-Perot laser is the most simple type of semiconductor lasers, figure 3.1 (b). The x directions define the transverse, y directions define the lateral and z-directions define longitudinal directions. Carriers and photons should be tightly confined to the same area in the xy plane. The two main designs of the transverse and lateral

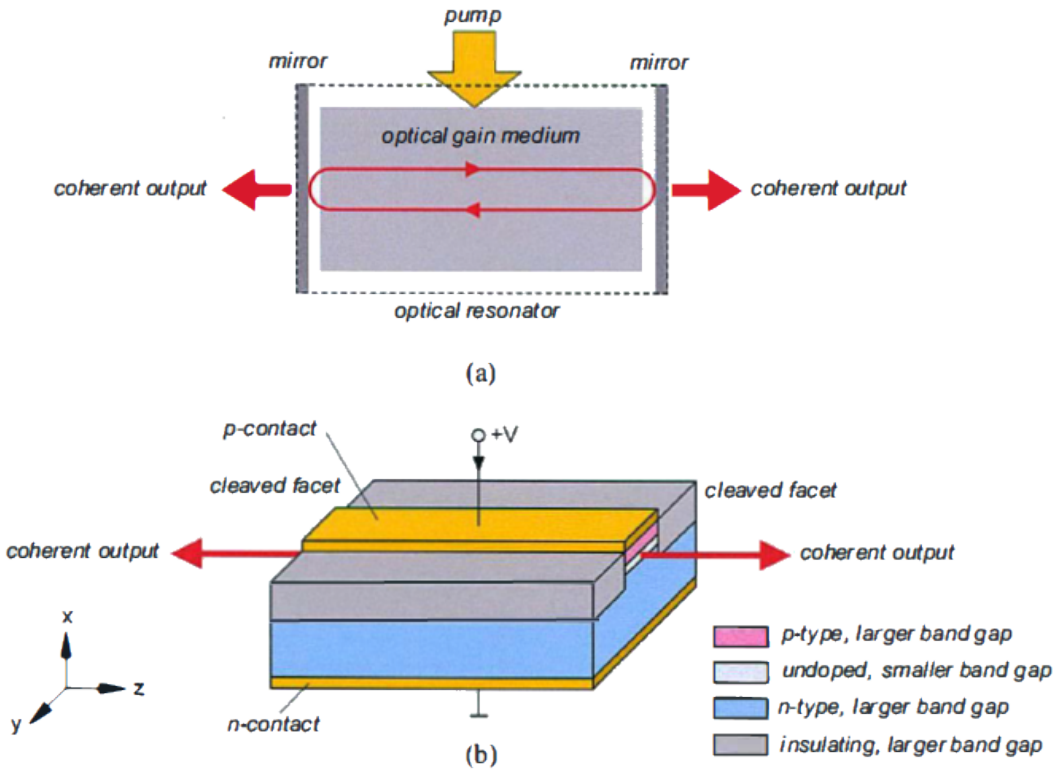

Figure 3.1: a) General design of a laser. b) A Fabry-Perot type of semiconductor laser.

confinement are the buried heterostructure laser and ridge waveguide laser.

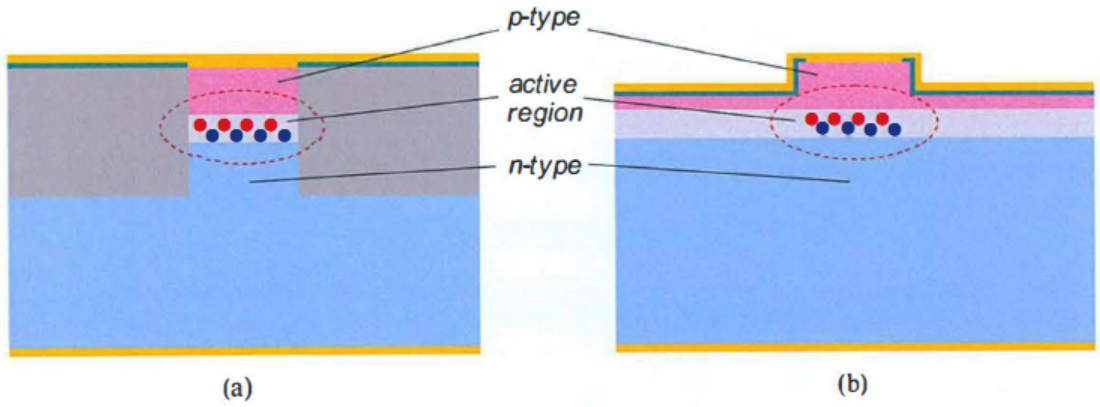

Figure 3.2: Cross-sectional view (xy-plane) of two commonly used laser structures. (a) Buried heterostructure laser. (b) Ridge waveguide laser. The spatial field distribution of the guided optical mode is indicated by the dashed red line and electrons and holes in the active region are illustrated by the blue and red bullets.

3.1.2 Optical gain, confinement and feedback

Injecting of the excess concentration of holes and electrons will establish a net optical gain in the active region, the net gain will start when the concentration exceeding the transparency carrier concentration. In the quantum well the peak gain is a sublinear dependence.

$$g(\Delta n) = g_0 \cdot \ln \frac{\Delta n}{\Delta n_{tr}} \quad ; \text{ for } QW_S \tag{3.1}$$

As seen from the figure 3.3, not all the guided optical mode overlaps the active region, but only a fraction of it. The overlapping fraction can be defined by the optical confinement factor:

$$\Gamma = \frac{\iint_{active-region} E_y^2(x,y)dxdy}{\iint_{everywhere} E_y^2(x,y)dxdy} \tag{3.2}$$

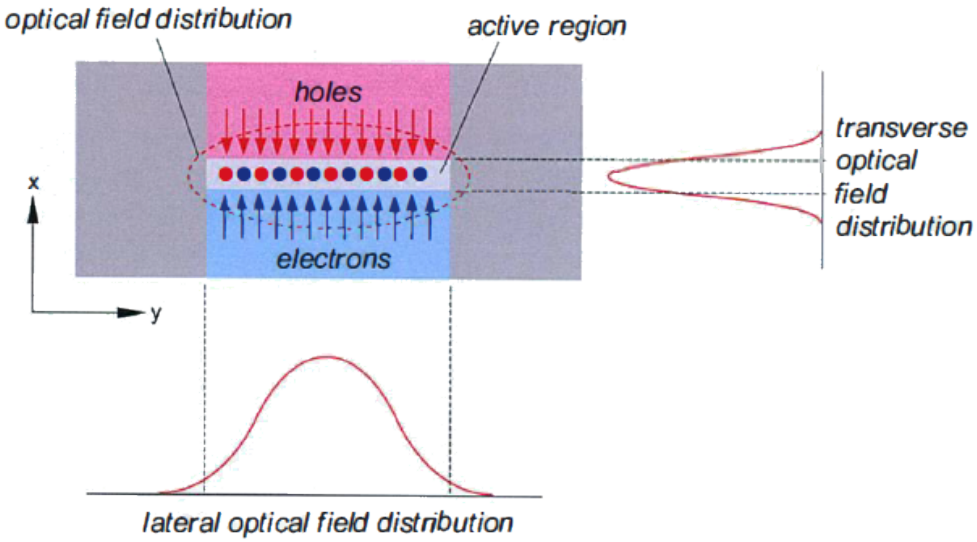

Figure 3.3: Carrier injection into the active region and the optical mode profile

Then, we can define the modal gain g_m, where g is the material gain and it is the maximum gain in the active region. The confinement factor in the QW is only a few percent.

Optical feedback usually provided by cleaving the sides perpendicularly and then the reflection occurs because of the difference between the effective refractive index of the guided mode n_{eff} and the air, figure 3.4.

$$R = \left(\frac{n_{eff} - 1}{n_{eff} + 1}\right)^2 \tag{3.3}$$

Without any type of coating, the power reflectively is around 30%, and then this value can be increased or decreased depends on the application.

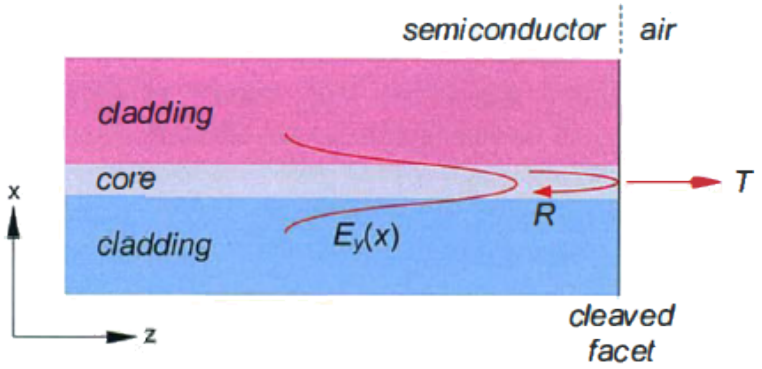

Figure 3.4: Optical reflection (R) and transmission (7) at the cleaved facet of a Fabry-Perot laser.

3.1.3 Lasing and threshold condition

The spontaneous and stimulated emissions occur simultaneously when the excess concentration of carriers injected in the active region. The net stimulated emission rate considering transitions between the conduction band and valence band can be written as:

$$R_{21}(\hbar\omega) - R_{12}(\hbar\omega) = B \cdot (f_n(E_2) - f_p(E_1)) \cdot \rho(\hbar\omega) \tag{3.4}$$

And the spontaneous emission rate will be:

$$R_{sp}(\hbar\omega) = A_{21} \cdot f_n(E_2) \cdot (1 - f_p(E_1)) \tag{3.5}$$

From equation 3.4, the optical gain occur when $f_n(E_2) > f_p(E_1)$ which is required for positive net stimulated emission rate and then the population inversion condition. This means that the difference between Fermi levels should be larger than the band gap energy $(E_{Fn} - E_{Fp}) > E_g$. This condition requires a large, coherent photon density. Spontaneous emission on the other hand is independent of the density of the photons, increasing the excess carrier concentration will increase the spontaneous emission rate.

The stimulated emission can be obtained by placing the gain material inside an optical resonator, figure 3.5. The light (optical mode) will propagate along the waveguide back and forth and it gets amplified. Outcoupling because of mirrors, absorption and scattering will cause a loss that the light will suffer from. Scattering loss rise from the imperfections along the waveguide, absorption loss rise from the free carriers absorption in the cladding layers. Absorption and scattering losses can be combined in one loss called internal optical loss and it accounted for as modal loss coefficient α_i.

The evolution of the carriers and photon densities with increasing the injection current J can be divided in four steps which can be seen in figure 3.6:

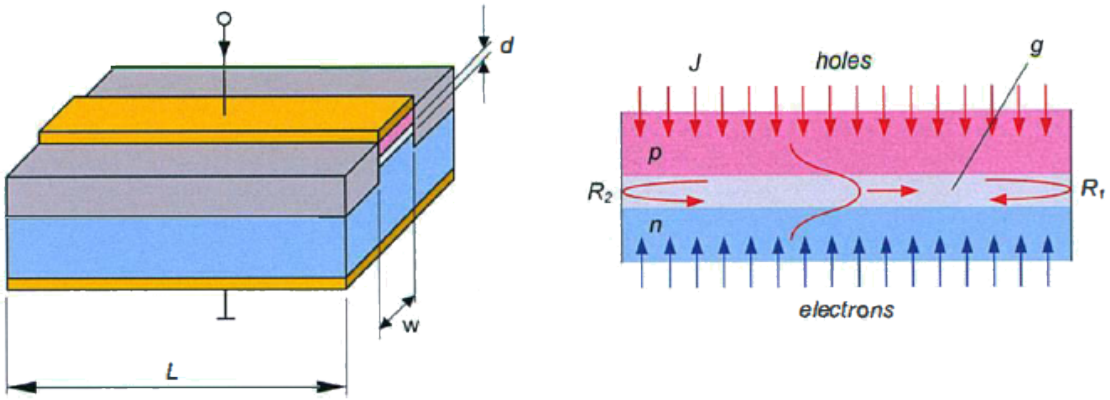

Figure 3.5: Left: The Fabry-Perot laser with dimensions indicated (L = length of the laser, w = width of the active region, d = thickness of the active region). Right: Cross-sectional view along the length of the laser (the xz-plane).

1- When current density is small, $(E_{Fn} - E_{Fp}) < E_g$, a net coherent photon density can not be established and the absorption is dominant. The only emission in this situation is spontaneous emission. The light is then incoherent and the beam divergence is large. However, a very small fraction of spontaneously generated photons will be able to escape the facets and thus the output power is very low.

2- Increasing the current density $(E_{Fn} - E_{Fp}) > E_g$, will increase the concentration of excess carriers and a net optical gain start to appear. But the gain is not that much high to overcome the losses. The emission is again incoherent but some concentration from spontaneous emission will make the spectral narrower and the beam divergence smaller. The out power still low.

3- More increasing of the current density will make the net optical gain compensates for the losses. This point called threshold gain. The emission at this point is mainly coherent with a very small fraction of spontaneous emission. The spectrum is quit narrow and divergence beam is low. The correspond excess carrier concentration is called the threshold carrier concentration.

4- After the injection current exceeds the threshold current, all excess carriers injected will immediately consumed by stimulated emission and the gain is saturated at this point, the output power increases with increasing the injected current above the threshold.

The spontaneous emission rate and excess carriers concentration increase linearly by increasing the injected current until the current reaches the threshold. After the threshold reached, they will reach a constant value even with increasing the current. This is illustrated in figure 3.7.

The optical field has to repeat itself after one round-trip. In other words, the amplitude should be the same and the phase should be an integer times of 2π. The

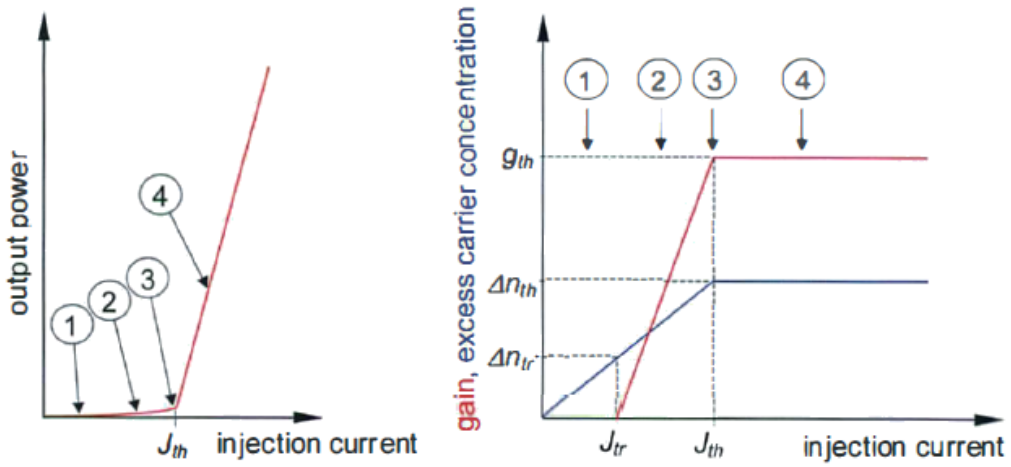

Figure 3.6: Left: Dependence of output power through the cleaved facets on the injection current density. Right: Dependence of gain and excess carrier concentration on injection current density.

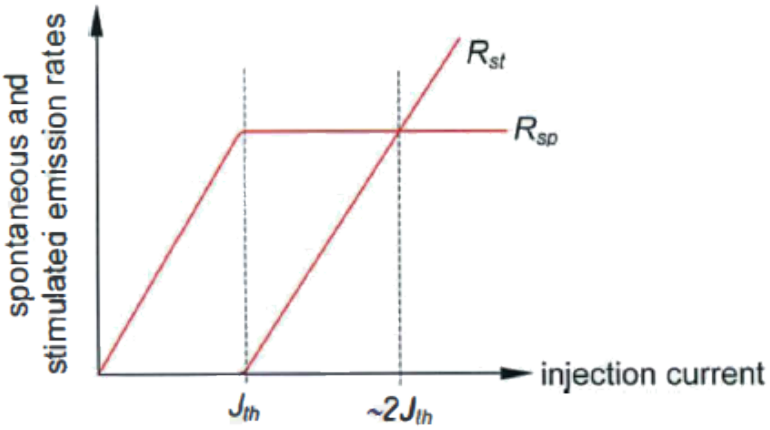

Figure 3.7: Spontaneous (R,p) and stimulated (R„) emission rates as a function of current

optical field polarized in y direction and propagating in z direction is given by:

$$E_y(x,y,z) = E_y(x,y) \cdot \exp(-j\beta z) \cdot \exp\left(\left(\Gamma\frac{g}{2} - \frac{\alpha_i}{2}\right) z\right) \tag{3.6}$$

where α_i is the internal optical loss, g represents the material gain and $E_y(x,y)$ is the transverse spatial field distribution. After one round-trip, the light propagates 2L, where L is the laser length, the optical field becomes:

$$E_y(x,y,z+2L) = \sqrt{R_1}\sqrt{R_2} \cdot E_y(x,y) \cdot \exp(-j\beta(z+2L)) \cdot \exp\left(\left(\Gamma\frac{g}{2} - \frac{\alpha_i}{2}\right)(z+2L)\right) \tag{3.7}$$

Where $R1$ and $R2$ are the reflectivities at the facets. The optical field should reproduce itself after one round-trip, this means $E_y(x,y,z+2L,t) = E_y(x,y,z,t)$. The two main conditions to get a coherent light emission are the amplitude and phase

condition. The amplitude condition is:

$$\sqrt{R_1}\sqrt{R_2}\cdot\exp\left(\left(\Gamma\frac{g_{th}}{2}-\frac{\alpha_i}{2}\right)2L\right)=1 \tag{3.8}$$

and this gives the threshold gain:

$$g_{m,th}=\Gamma g_{th}=\alpha_i+\frac{1}{2L}\ln\frac{1}{R_1R_2} \tag{3.9}$$

And the material threshold gain is then:

$$g_{th}=\frac{1}{\Gamma}\left[\alpha_i+\frac{1}{2L}\ln\frac{1}{R_1R_2}\right] \tag{3.10}$$

The last equation shows that after one round-trip, the material gain should compensate for the mirror and internal optical losses.
The second condition is the phase condition:

$$\exp(-j\beta 2L)=1\rightarrow\beta 2L=m\cdot 2\pi \qquad m=1,2,3,... \tag{3.11}$$

From that, we get:

$$n_{eff}\cdot L=m\cdot\frac{\lambda_0}{2}\rightarrow\lambda_0=\frac{2Ln_{eff}}{m} \tag{3.12}$$

The last equation shows that each m integer represents a standing wave of half wavelength along the resonator. Each standing wave represents a longitudinal mode of the resonator.
There is infinite number of longitudinal modes but only the modes that have the wavelengths within the gain spectrum are of interest because these modes are only the modes that contain coherent photons.
To get the spacing between the longitudinal modes we can use the last equation and derive it with respect to λ_0.

$$\frac{dm}{d\lambda_0}=\frac{2L}{\lambda_0}\cdot\frac{dn_{eff}}{d\lambda_0}-\frac{2Ln_{eff}}{\lambda_0^2} \tag{3.13}$$

$dn_{eff}/d\lambda_0$ represents the dispersion in the waveguide. Now if we increase m by 1, $\Delta m=1$, the longitudinal mode spacing is then given by:

$$\Delta\lambda_0=\frac{\lambda_0^2}{2Ln_{eff}}\left(1-\frac{\lambda_0}{n_{eff}}\cdot\frac{dn_{eff}}{d\lambda_0}\right)^{-1}=\frac{\lambda_0^2}{2Ln_{geff}} \tag{3.14}$$

The modal group index determines the longitudinal mode spacing and the mode index m determines the wavelengths of the longitudinal modes. From the last equation, we found that longitudinal mode spacing is around 0.4 [nm]. The gain spectrum is of tens of nm's. This means that a large number of longitudinal modes will at the same time contain coherent photons. And the laser is multi longitudinal modes laser. This is illustrated in the figure 3.8.

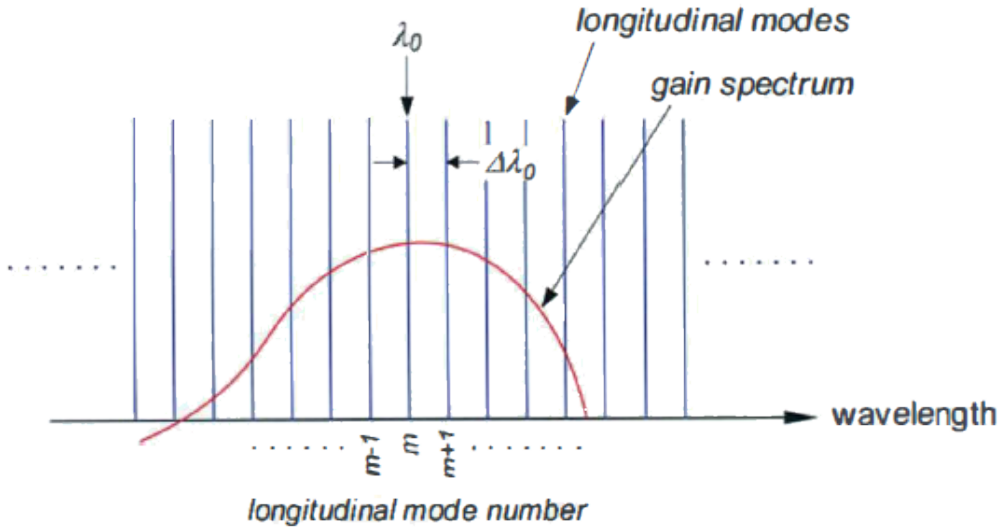

Figure 3.8: The longitudinal modes of a Fabry-Perot laser and the gain spectrum of the active region.

3.1.4 Threshold current, output power and efficiency

The threshold current considered as a performance parameter for semiconductor lasers and it can be calculated by equating the total spontaneous recombination rate to the generated excess carriers generated at the threshold current.

$$R_{sp}\left(\Delta n_{th}\right) = A \cdot \Delta n_{th} + B \cdot \Delta n_{th}^2 + C \cdot \Delta n_{th}^3 \tag{3.15}$$

$$\eta_i \frac{I_{th}}{qV_{act}} = R_{sp}\left(\Delta n_{th}\right) \Rightarrow I_{th} = \frac{qwLd}{\eta_i} \cdot R_{sp}\left(\Delta n_{th}\right) \tag{3.16}$$

Where $V_{act} = wLd$ is the volume of the active region. The fraction of the injected current that generates excess carriers is known as internal quantum efficiency η_i. The threshold current depends on the temperature exponentially since the A,B and C coefficients and Fermi-levels depends on the temperature.

$$I_{th} \propto \exp \frac{T}{T_0} \Rightarrow \frac{1}{T_0} = \frac{1}{I_{th}} \cdot \frac{dl_{th}}{dT} \tag{3.17}$$

All carriers injected above the threshold will contribute to coherent output power since the threshold carrier concentration recombine through stimulated emission.

$$P_{\text{internal}} = \eta_i \cdot \frac{I - I_{th}}{q} \cdot hv \tag{3.18}$$

The last equation shows the product between the number of excess carriers that reach the active region and the photon energy. The output power as a function to the mirror loss is given by:

$$P = \eta_i \cdot \frac{I - I_{th}}{q} \cdot hv \cdot \frac{\frac{1}{2L} \ln \frac{1}{R_1 R_2}}{\alpha_i + \frac{1}{2L} \ln \frac{1}{R_1 R_2}} \tag{3.19}$$

Defining the external differential quantum efficiency η_d as the fraction of the excess carrier that produces output photons:

$$\eta_d = \frac{\Delta(P/hv)}{\Delta\left((I - I_{th})/q\right)} \Rightarrow \eta_d = \eta_i \cdot \frac{\frac{1}{2L}\ln\frac{1}{R_1R_2}}{\alpha_i + \frac{1}{2L}\ln\frac{1}{R_1R_2}} \tag{3.20}$$

Defining the slope efficiency as the output power over the current above threshold and it has the unit [W/A]:

$$\left(\frac{\Delta P}{\Delta I}\right)_{\text{above threshold}} = \frac{hv}{q} \cdot \eta_i \cdot \frac{\frac{1}{2L}\ln\frac{1}{R_1R_2}}{\alpha_i + \frac{1}{2L}\ln\frac{1}{R_1R_2}} = \frac{hv}{q} \cdot \eta_d \tag{3.21}$$

The figure shows the output power P and the applied voltage V of a semiconductor laser as a function of injection current. Then we define the power efficiency η_p at a given bias current I as:

$$\eta_p = \frac{P}{VI} \tag{3.22}$$

The figure 3.9 shows the power/voltage with respect to the injected current J.

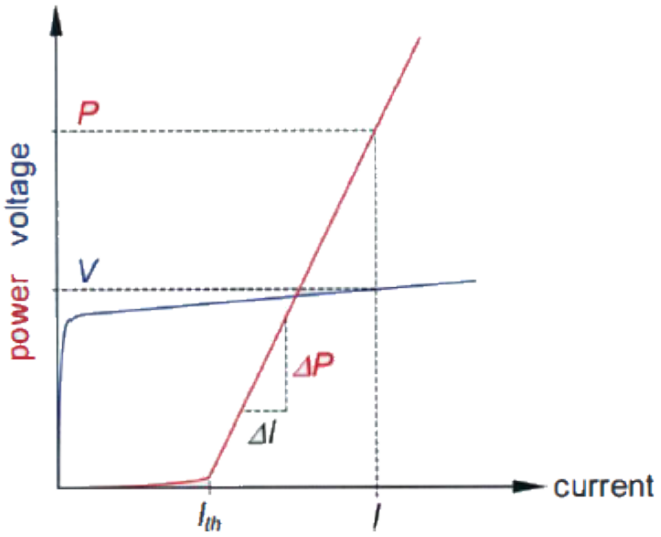

Figure 3.9: The output power and voltage of a semiconductor laser as a function of injection current.

3.1.5 Rate equation analysis

Performance characteristics of semiconductor laser can be analysed using rate equation. The two main rate equations used in semiconductor laser are excess carrier concentration in the active region and the photon densities in the longitudinal modes. Assuming that there is no noise, only the fundamental mode propagate, the peak gain linearly depends on the excess carrier density and the active region has bulk properties. The gain spectrum cab be expressed as:

$$g\left(E_{ph}, \Delta n\right) = g_0 \cdot \left(\Delta n - \Delta n_{tr}\right) \cdot \left[1 - \left(\frac{E_{ph} - E_{ph0}}{\Delta E_{ph}}\right)^2\right] \tag{3.23}$$

where ΔE_{ph} is the width of the gain spectrum and E_{ph0} is the photon energy at the peak. This can be considered as a good approximation of the gain spectrum (figure 3.10) as the multimode rate equations refer to the two rate equations for excess carrier concentration and photon densities and they given by:

$$\frac{d\Delta n}{dt} = \frac{\eta_i J}{qd} - \frac{c}{n_{geff}} \sum_m g_m S_m - \frac{\Delta n}{\tau} \tag{3.24}$$

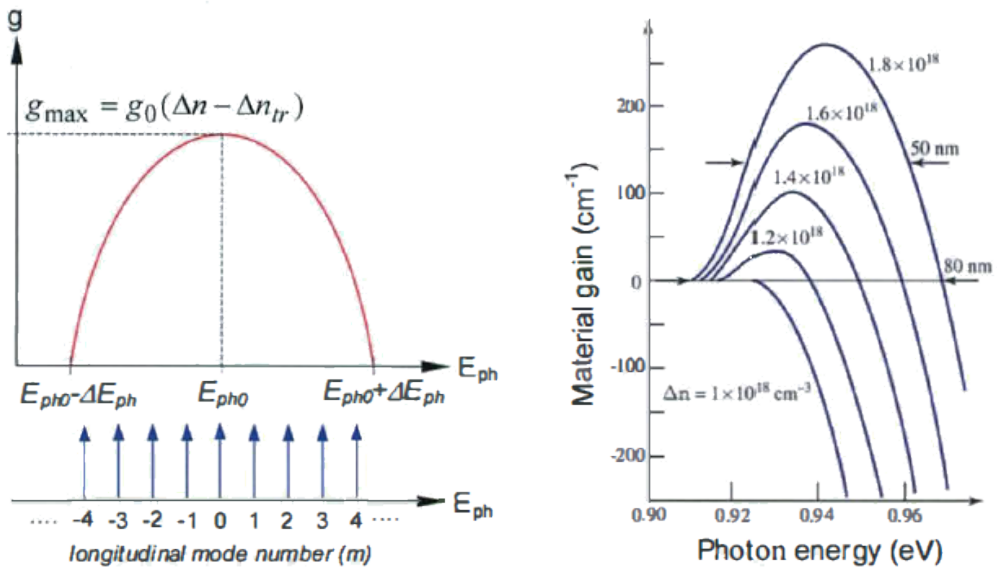

Figure 3.10: Left: Gain spectrum and dependence of peak gain on excess carrier concentration for the rate equation analysis. Right: Calculated gain spectra at different excess carrier concentrations for an LnGaAsP active region with bulk properties (from N.K. Dutta, J. Appl. Phys. 5 1 , 6095, 1 980).

$$\frac{dS_m}{dt} = \Gamma \frac{c}{n_{geff}} g_m S_m + \Gamma \beta_s \frac{\Delta n}{\tau} - \frac{S_m}{\tau_p} \tag{3.25}$$

where S_m is the photon density in the longitudinal mode m. Δn is the excess carrier density in the active region. J is the injected current density. d is the thickness of the active layer. g_m is the material gain of the mode m at the photon energy. $g_m S_m$ represents the loss of carrier due to stimulated emission in the mode m. c/n_{geff} The photons propagation speed in the material. $\Delta n/\tau$ represents the loss due to spontaneous emission. τ is the spontaneous emission lifetime.

The second equation describes the photon density evolution where the first term describe the photon density inside the mode m due to stimulated emission. Γ is the optical confinement factor since the photon density occupy larger volume than carrier density ($V_{act} = \Gamma \cdot V_{mode}$). There is some spontaneous emission added

to the stimulated emission and it has same amplitude and phase as the coherent light. β_s represents the spontaneous emission factor. The loss of photons through outcoupling and optical loss can be represented through the last term $\S_m/\tau_p$ where τ_p is the photon lifetime and it given by:

$$\frac{1}{\tau_p} = \frac{c}{n_{geff}} \left(\alpha_i + \frac{1}{2L} \ln \frac{1}{R_1 R_2} \right) \tag{3.26}$$

The spontaneous carrier lifetime is much larger the photon lifetime. The multimode rate equations can be converted to single rate equations by assuming one longitudinal mode:

$$\frac{d\Delta n}{dt} = \frac{\eta_i J}{qd} - \frac{c}{n_{geff}} gS - \frac{\Delta n}{\tau} \tag{3.27}$$

$$\frac{dS}{dt} = \Gamma \frac{c}{n_{geff}} gS + \Gamma \beta_s \frac{\Delta n}{\tau} - \frac{S}{\tau_p} \tag{3.28}$$

In figure 3.11, an illustration of the interaction between carriers and photons in the laser can be seen.

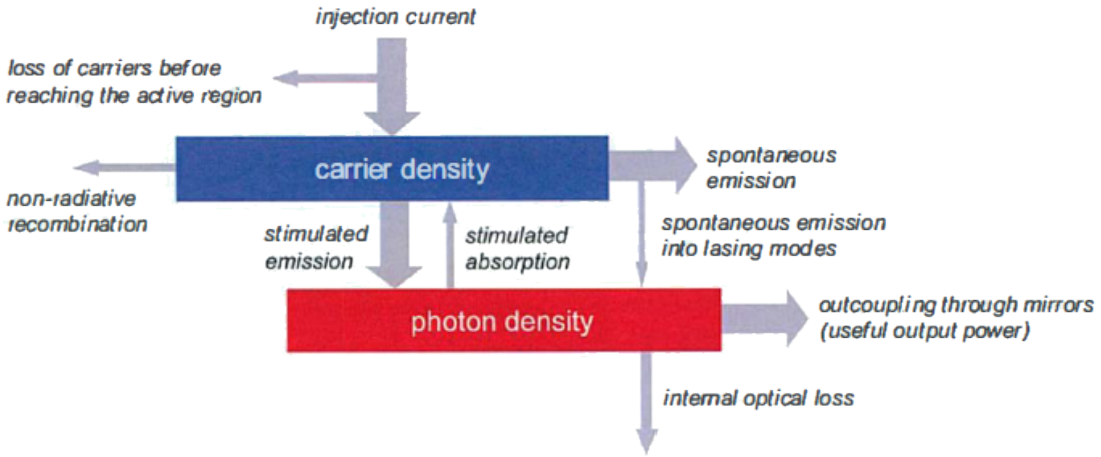

Figure 3.11: Illustration of the interaction between carriers and photons in a semiconductor laser through stimulated emission. The loss of carriers before reaching the active region is accounted for by the internal quantum efficiency, which is set to unity in the rate equation analysis. The difference between stimulated emission and stimulated absorption rates is the net stimulated emission rate, which provides the material gain.

3.1.6 Static performance characteristics

Known as steady-state as well. At the steady-state, the rate equations derivatives with respect to time equal to zero.

3.1.6.1 Power-current characteristics

Setting $dS/dt = 0$ in the photon evolution equation gives us the output power on the current density:

$$S = \frac{\Gamma\beta_s \frac{\Delta n}{\tau}}{\frac{1}{\tau_p} - \Gamma\frac{c}{n_{geff}}g} \tag{3.29}$$

Inserting S in the carrier evolution equation and setting the derivative to zero gives (assuming $g = g_{max}$):

$$\frac{\eta_i J}{qd} = \Delta n \left(\frac{\frac{c}{n_{geff}} g\Gamma\beta_s \frac{1}{\tau}}{\frac{1}{\tau_p} - \Gamma\frac{c}{n_{geff}}g} \right) + \frac{\Delta n}{\tau} \tag{3.30}$$

The output power from both mirrors equals to the total number of photons inside the mode times the photon energy times escape rate through the mirrors.

$$P = SV_{\text{mode}} \cdot \frac{c}{n_{geff}} \left(\frac{1}{2L} \ln \frac{1}{R_1 R_2} \right) \cdot \frac{hc}{\lambda_0} \tag{3.31}$$

$V_{mode} = V_{act}/\Gamma = Ldw/\Gamma$ is the mode volume. Figure 3.12 illustrates the output power with respect to the injected current and the dependency on the spontaneous emission factor β_s. Increasing the spontaneous emission factor means that more spontaneously emitted photon enters the lasing mode. When $\beta_s = 1$, the coherent light builds up from the dominant incoherent output power at low currents until the stimulated emission starts. Figure 3.13 shows the material gain for both the main mode and the side modes.

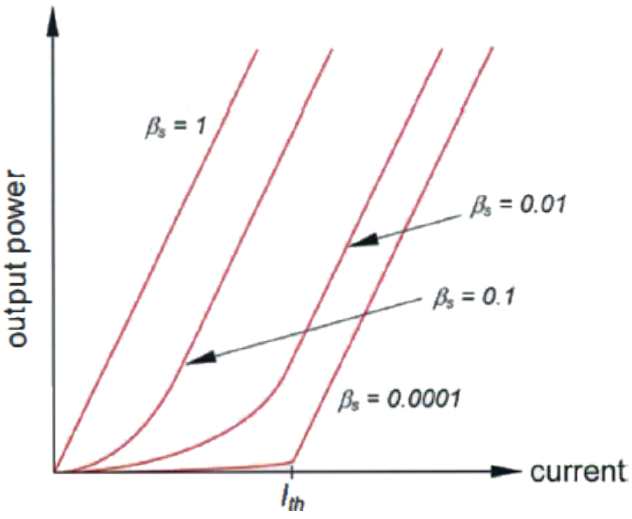

Figure 3.12: Output power vs. current for different values of the spontaneous emission factor.

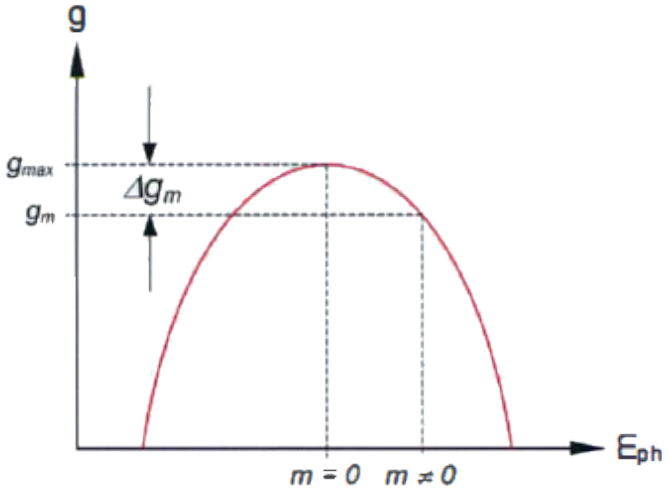

Figure 3.13: Material gain for the main mode and the side modes.

3.1.6.2 Spectral characteristics

Many closely spaced longitudinal modes exists in Fabry-Perot laser which gives wide emission spectrum. Larger portion of the total power overlaps only several modes. Again, the multimode equations at the steady-state are:

$$\frac{\eta_i J}{qd} = \frac{c}{n_{geff}} \sum_m g_m S_m + \frac{\Delta n}{\tau} \tag{3.32}$$

$$\Gamma \beta_S \frac{\Delta n}{\tau} = S_m \left(\frac{1}{\tau_p} - \Gamma \frac{c}{n_{geff}} g_m \right) \tag{3.33}$$

The last equation shows that the loss inside the laser will be compensated by the gain due to stimulated emission plus a small amount of spontaneous emission in the lasing mode. The photon density in mode m is then:

$$S_m = \frac{n_{geff}}{c} \cdot \frac{\beta_s \frac{\Delta n}{\tau}}{\frac{1}{\Gamma}\left(\alpha_i + \frac{1}{2L} \ln \frac{1}{R_1 R_2}\right) - g_m} \tag{3.34}$$

Assuming Δg_m is the gain difference between the mode under consideration (side mode) and the gain peak (main mode).

$$S_m = \frac{n_{geff}}{c} \cdot \frac{\beta_s \frac{\Delta n}{\tau}}{\frac{1}{\Gamma}\left(\alpha_i + \frac{1}{2L} \ln \frac{1}{R_1 R_2}\right) - g_{\max} + \Delta g_m} \tag{3.35}$$

The output power equals to the photon density inside the volume V_{mode}:

$$P_m = S_m r'_{m\alpha de} \cdot \frac{c}{n_{geff}} \left(\frac{1}{2L} \ln \frac{1}{R_1 R_2} \right) \cdot \frac{hc}{\lambda_0} \tag{3.36}$$

Contributing from all modes give the total power:

$$P = \sum_m P_m \tag{3.37}$$

Figure 3.14 shows that the photon densities almost equals for all modes. Increasing the current will cause a saturation in photon densities starting from the furthest side mode from the main mode. The spectral width decreases with the current and the multimode laser near the threshold becomes a single-mode far above the threshold.

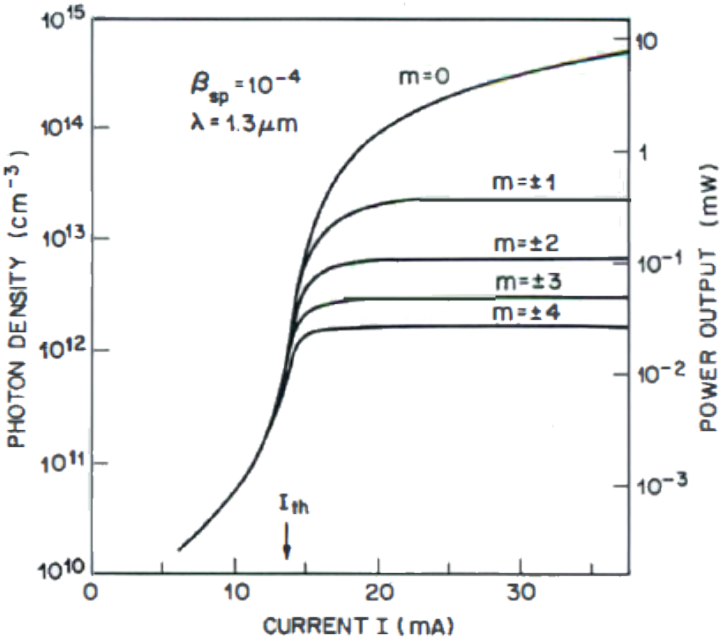

Figure 3.14: Photon densities and corresponding output powers from different longitudinal modes of a 1 .3 μm lnGaAsP Fabry-Perot t11ser with /J, = I 0-4 (from G.P. Agrawal and N.K. Dutta, Long Wavelength Semiconductor Lasers, Van Nostrand Reinhold, 1986).

The Side Mode Suppression Ratio (SMSR) defined as the ratio of the power in mode m to the power in the main mode:

$$SMSR_m = \frac{P_m}{P_0} = \frac{S_m}{S_0} = \frac{1}{1 + \frac{c}{n_{\text{geff}}} \frac{\tau}{\beta_s \Delta n} S_0 \Delta g_m} = \frac{1}{1 + \frac{S_0}{S_{\text{msat}}}} \tag{3.38}$$

where S_{mat} defined as:

$$S_{msat} = \frac{n_{geff}}{c} \frac{\beta_s \Delta n}{\tau} \frac{1}{\Delta g_m} \tag{3.39}$$

and it is the photon density in the mode m. In dB $SMSR$ is given by:

$$SMSR = 10 \cdot \log \frac{P_0}{P_{m,\max}} \tag{3.40}$$

SMSR is an important measure of the special purity of the laser. Usually, a single mode laser has SMSR > 30 dB and multimode laser has the SMSR < 30 dB. $P_{m,max}$ is the power value inside the most intense side mode. Strong suppression of side modes can be obtain by having a small spontaneous emission factor and large mode separation Δg_m. Narrower gain spectrum and larger longitudinal modes spacing will make the laser a single mode laser.

The photon density at mode m is given by:

$$S_m = \frac{n_{geff}}{c} \cdot \frac{\beta_s \frac{\Delta n}{\tau}}{\frac{1}{\Gamma}\left(\alpha_i + \frac{1}{2L}\ln\frac{1}{R_1 R_2}\right) - g_0\left(\Delta n - \Delta n_{tr}\right) \cdot \left[1 - \left(\frac{E_{ph}-E_{ph0}}{\Delta E_{ph}}\right)^2\right]} \tag{3.41}$$

The last equation shows that the mode envelope is a Lorentzian function and the gain spectrum is an inverted parabola. The figure 3.15 shows the approximation of the mode envelope which follow the Lorentzian function.

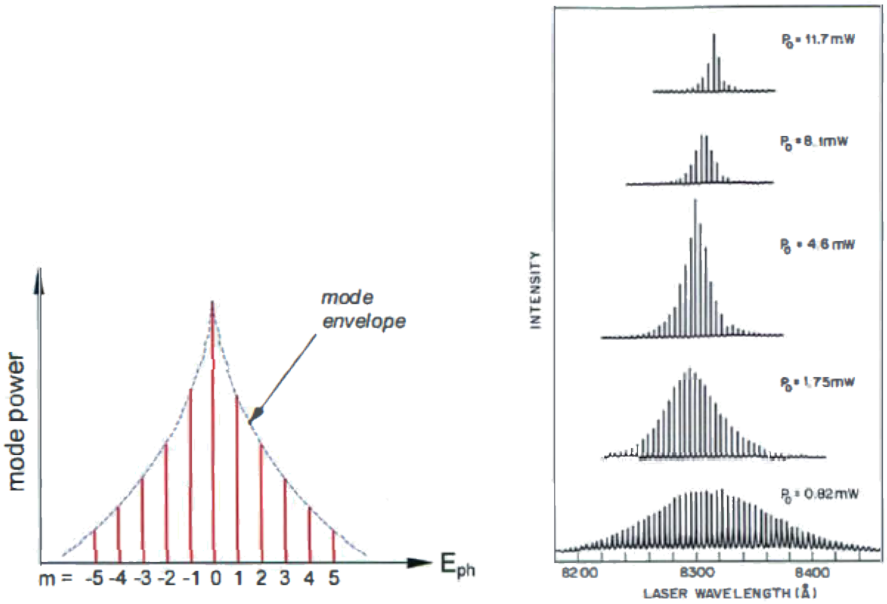

Figure 3.15: Left: Longitudinal mode spectrum of a Fabry-Perot laser with a Lorentzian mode envelope. Right: Measured emission spectra for an 830 nm AlGaAs laser at different currents above threshold (from W. Strei fer et al., Appl. Phys. Lett. 40, 305, 1 982).

3.1.6.3 Beam characteristics

The beam shape and its divergence of the laser is of great importance. The light wave is confined inside the laser, but as long as the laser beam leaves the laser, it starts to diverge due to diffraction. Fraunhofer diffraction theory can be used to analyse the divergence characteristics. Stronger confinement will give larger divergence. The divergence characteristics should be analyse in the far-field region since the cross-section of the laser waveguide is rectangular and then the divergence on in the transverse direction is greater than the one on the lateral direction. The resulting beam will have an elliptical shape.

The divergence can be characterized suing the divergence angles ($\Phi_x and \Phi_y$), these angles represent the divergence in the transverse and later divergence respectively.

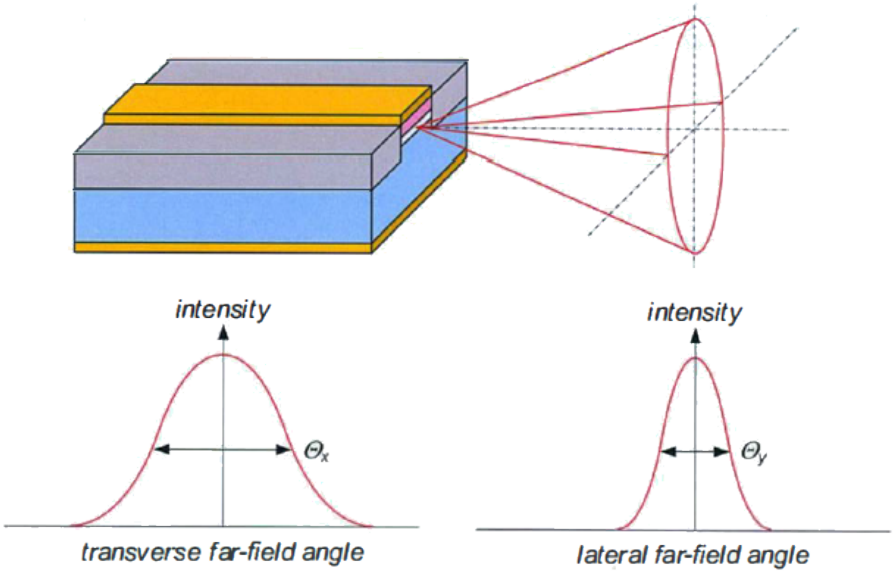

Figure 3.16: Beam characteristics of a semiconductor laser with a single mode waveguide, also showing the transverse and lateral divergence angles.

This is illustrated in the figure 3.16.

The Beam Parameter Product (BPP) defines the quality of a laser beam. BPP is the product between the beam divergence and its waist at the laser facet. Usually the comparison occur between the BPP of the laser beam and the BPP of an ideal Gaussian beam since the Gaussian beam has the smallest BPP. The ration known as M^2 value. The laser that has M^2 close to one is a very high quality laser. High quality beam is important in many applications since it can be focused to a small spot.

3.1.7 Dynamic performance characteristics

Modulating the output power of a laser is very important and it can be done by modulating the injected current. The upcoming analyses will describe the response of the laser to rapid change in the injected current, and this known as dynamic characteristics.

3.1.7.1 Transient dynamics

Applying a current step signal on the laser arise several important observations. At t = 0, the excess carrier density Δn start to increase. After a certain period, the carrier density start to saturate, this period known as turn-on delay time. The stimulated emission starts and the carrier density reaches the threshold. This means that the photon density in the longitudinal mode increases.

This stimulated emission will consume quickly the excess carriers injected in the active region and this will lower the carrier concentration under the threshold value

and the laser then turns off. This will get the carrier concentration to increase again until it reach the threshold and the laser turns on. The photon and carrier densities oscillate back and forth, and after some cycles, the laser reaches the steady-state. Figure 3.17 shows the output of a simulation of the multimode rate equations when applying a step current.

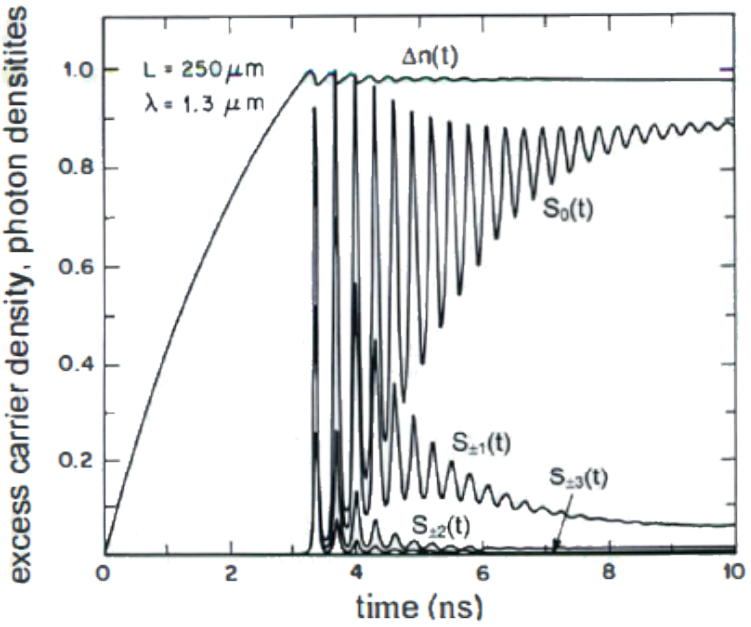

Figure 3.17: The response of a l .3 μm lnGaAsP Fabry-Perot laser to a current step (from G.P. Agrawal and N.K. Dutta, Long Wavelength Semiconductor Lasers, Van Nostrand Reinhold, 1986).

Relaxation oscillations is the damped oscillations that make the carrier and photon densities reach their steady-state. The relaxation oscillations occurs at the relaxation frequency. This means that the laser behaves as a second order damped system. During rapid current modulation, the carrier density is not clamped exactly at the threshold value, this small variations of the carrier density will cause a variation in gain and as a result, the operation state will be multimode and a big amount of photons density will be in several longitudinal side modes.

3.1.7.2 Turn-on delay

As discussed before, the turn-on delay time is the time needed for the excess carrier to reach the threshold. Before this time, the photon density equals to zero. Turn-on delay time can be calculated by setting $S = 0$ in rate equation for the carrier density.

$$\frac{d\Delta n(t)}{dt} = \frac{\eta_i \left(J_s + J_b\right)}{qd} - \frac{\Delta n(t)}{\tau} \tag{3.42}$$

J_b is the bias current and J_s is the current step. J_b used to near the threshold current so that the J_s will bringing the total applied current above the threshold as can be seen at figure 3.18.

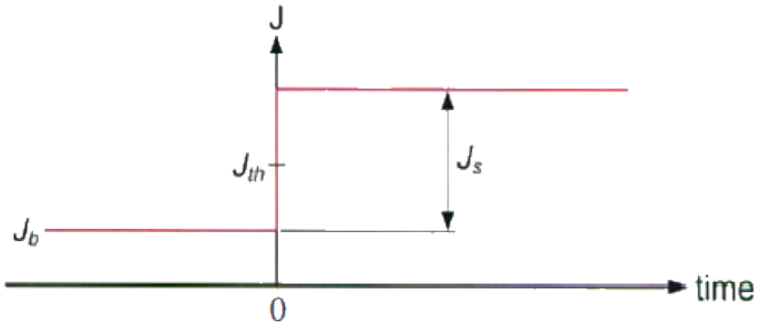

Figure 3.18: Currents involved when analyzing the tum-on delay time.

To get the turn-on delay time equation, equation 3.42 can be integrated fro $t = 0$ to $t = t_d$ and then the carrier density have to be integrated from Δn_b to Δn_{th} where Δn_b is the carrier density at the steady-state when the current is J_b.

$$\int_{\Delta n_b}^{\Delta n_{th}} \frac{d\Delta n(t)}{\frac{\eta_i(J_s+J_b)}{qd} - \frac{\Delta n(t)}{\tau}} = \int_0^{t_d} dt \Rightarrow t_d = \tau \cdot \ln\left(\frac{I_s}{I_s + I_b - I_{th}}\right) \tag{3.43}$$

When $I_b = 0$, $I_s = 1.5 \times I_{th}$ and $\tau = 2$ [ns], the turn-on delay time will be 2.2 [ns] and this considered as a very long time because it will limit the modulation speed of the laser. this problem can be relaxed by setting the bias current equals to threshold current.

3.1.7.3 Modulation response and bandwidth

The modulation response can be studied by analyzing the response of output power with respect to the injected current. The small signal analyses can be done under some assumptions:
1- The optical gain is constant around the bias current point:

$$g = g_b + \frac{dg}{d\Delta n} \cdot \delta\Delta n = g_{th} + \frac{dg}{d\Delta n} \cdot \delta\Delta n \tag{3.44}$$

where $dg/d\Delta n$ is the differential gain around the bias point.

2- The spontaneous emission coefficient is neglected in the lasing mode ($\beta_s = 0$).
3- The biasing current I_b is above the threshold current.
4- The carrier density, photon density and current density deviations from the steady-state values are very small. i.e. $\delta J << J_b$, $\delta\Delta n << \Delta n_b$ and $\delta S << S_b$.
Re-writing the rate equations of the single mode:

$$\frac{d}{dt}\Delta n = \frac{\eta_i J}{qd} - \frac{c}{n_{geff}} \cdot g \cdot S - \frac{\Delta n}{\tau} \tag{3.45}$$

$$\frac{d}{dt}S = \Gamma \cdot \frac{c}{n_{geff}} \cdot g \cdot S - \frac{S}{\tau_p} \tag{3.46}$$

And then substituting the assumed values: ($d/dt = 0$, $J = J_b$, $\Delta n = \Delta n_b = \Delta n_{th}$ and $S = S_b$), the rate equations become then:

$$S_b = \frac{n_{geff}}{cg_b} \cdot \left(\frac{\eta_i J_b}{qd} - \frac{\Delta n_{th}}{\tau} \right) \tag{3.47}$$

$$\Gamma \cdot \frac{c}{n_{geff}} \cdot g_b = \frac{1}{\tau_p} \tag{3.48}$$

Superimposing the small signal terms inside the steady-state equations can be done using perturbation analysis:

$$J(t) = J_b + \delta J(t) \tag{3.49}$$

$$\Delta n(t) = \Delta n_b + \delta \Delta n(t) = \Delta n_{th} + \delta \Delta n(t) \tag{3.50}$$

$$S(t) = S_b + \delta S(t) \tag{3.51}$$

The time derivative of the steady-state values equal to zero, substituting the previous equations on the rate equations will give the following:

$$\frac{d}{dt}\delta \Delta n = -\frac{1}{\Gamma \tau_p}\delta S - \left(\frac{c}{n_{geff}} \cdot \frac{dg}{d\Delta n} \cdot S_b + \frac{1}{\tau} \right) \delta \Delta n + \frac{\eta_i}{qd} \cdot \delta J \tag{3.52}$$

$$\frac{d}{dt}\delta S = \Gamma \cdot \frac{c}{n_{geff}} \cdot \frac{dg}{d\Delta n} \cdot S_b \cdot \delta \Delta n \tag{3.53}$$

taking the time derivative of the second equation and substituting it in the first equation gives:

$$\frac{d^2}{dt^2}\delta S + \gamma \frac{d}{dt}\delta S + \omega_r^2 \delta S = \frac{c}{n_{\text{geff}}} \cdot \frac{dg}{d\Delta n} \cdot \Gamma S_b \cdot \frac{\eta_i}{qd} \cdot \delta J \tag{3.54}$$

which is a second order differential equation where ω_r is the resonance frequency and γ is the damping rate and they are given by:

$$\omega_r = \sqrt{\frac{c}{n_{geff}} \cdot \frac{dg}{d\Delta n} \cdot \frac{S_b}{\tau_p}} \quad ; \quad f_r = \frac{\omega_r}{2\pi} = \frac{1}{2\pi} \cdot \sqrt{\frac{c}{n_{geff}} \cdot \frac{dg}{d\Delta n} \cdot \frac{S_b}{\tau_p}} \tag{3.55}$$

$$\gamma = \frac{c}{n_{geff}} \cdot \frac{dg}{d\Delta n} \cdot S_b + \frac{1}{\tau} = \tau_p \cdot \omega_r^2 + \frac{1}{\tau} = 4\pi^2 \tau_p \cdot f_r^2 + \frac{1}{\tau} \tag{3.56}$$

The second order differential equations describe the output power response (photon density response) with respect to the variation of the injected current and as described before, the laser act as second order system with resonance frequency and γ damping rate γ.

The second order system is considered to be under-damped because of damping rate. The second order system reaches its own steady-state every time it experience the damping oscillation. The damping oscillation known as relaxation oscillations since it does relax (damps) the system to the steady-state. The resonance frequency is

slightly larger than the relaxation oscillations due to damping.

Last two equations show that increasing the photon density will increase both the resonance frequency and damping oscillation rate. We saw that $J/qd = I/qV_{act}$ and $(\eta_l J_{th}/qd = \Delta n_{th}/\tau)$ and substituting these in the equations 3.47 and 3.48 will give the dependence of the resonance frequency on current.

$$f_r = D \cdot \sqrt{I_b - I_{th}} \quad \text{where} \quad D = \frac{1}{2\pi}\sqrt{\frac{\eta_i \Gamma}{qV_{act}} \cdot \frac{c}{n_{geff}} \cdot \frac{dg}{d\Delta n}} \tag{3.57}$$

D-factor determines the rate at which resonance frequency changes with the current. The resonance frequency can be related to damping rate by the K-factor that given by:

$$\gamma = K \cdot f_r^2 + \gamma_0 \quad \text{where} \quad K = 4\pi^2 \tau_p \quad \text{and} \quad \gamma_0 = \frac{1}{\tau} \tag{3.58}$$

The gain is assumed to be linear in the active region but the gain is reduced at high photon density because of high stimulated emission and at this point, the gain get saturated.

$$g_b = \frac{g_{b,\text{ uns}}}{1 + \varepsilon \cdot S_b} \tag{3.59}$$

where ε is known as gain compression factor and $g_{b,ths}$ is the unsaturated gain, i.e. the gain at low photon densities. The K-factor becomes then:

$$K = 4\pi^2 \left(\tau_\rho + \frac{\varepsilon}{(c/n_{geff}) \cdot (dg/d\Delta n)}\right) \tag{3.60}$$

Assuming that the injected current is modulated using a sinusoidal signal that has frequency ω. The second order system equation 3.54 can be solved in frequency domain by changing each $\delta/\delta t$ with $j\omega$, this will give the photon density dependency on the modulation frequency.

$$\delta S(\omega) = \frac{\frac{c}{n_{geff}} \cdot \frac{dg}{d\Delta n} \cdot \Gamma S_b \cdot \frac{\eta_i}{qd}}{\omega_r^2 - \omega^2 + j\gamma\omega} \cdot \delta J \tag{3.61}$$

The last equation can be written as $\delta S(\omega) = \delta S(0) \cdot H(\omega)$ where $\delta S(0)$ is the low frequency value of the modulated photon density and expanding this equation will give:

$$\delta S(0) = \frac{\frac{c}{n_{geff}} \cdot \frac{dg}{d\Delta n} \cdot \Gamma S_b \cdot \frac{\eta_i}{qd}}{\omega_r^2} \cdot \delta J \quad \text{and} \quad H(\omega) = \frac{\omega_r^2}{\omega_r^2 - \omega^2 + j\gamma\omega} \tag{3.62}$$

where $H(\omega)$ is the complex transfer function, the amplitude represents the frequency response of the power modulation which called the modulation response:

$$|H(\omega)| = \frac{\omega_r^2}{\sqrt{\left(\omega_r^2 - \omega^2\right)^2 + \gamma^2\omega^2}} \tag{3.63}$$

Figure 3.19 shows the modulation response of a semiconductor laser with respect to the bias current. Frequencies below the resonance frequency, the response is flat, at the resonance frequency, the response experiencing a peak and then it starts to decay dramatically at frequencies greater than the resonance frequency. The frequency where the modulation response is 3 [dB] below the low frequency value is known as the modulation bandwidth. As seen in the equation 3.57, the resonance frequency and damping rate increase with increasing the current. This means that the bandwidth will increase, but the damping rate increases at same time, this make the damping rate faster than the resonance frequency. As a consequence, there is a current where the maximum modulation bandwidth is reached. The maximum damping limited bandwidth given by:

$$f_{3dB,\text{ damping}} = \frac{2\pi\sqrt{2}}{K} \tag{3.64}$$

And it is known as the intrinsic modulation bandwidth.

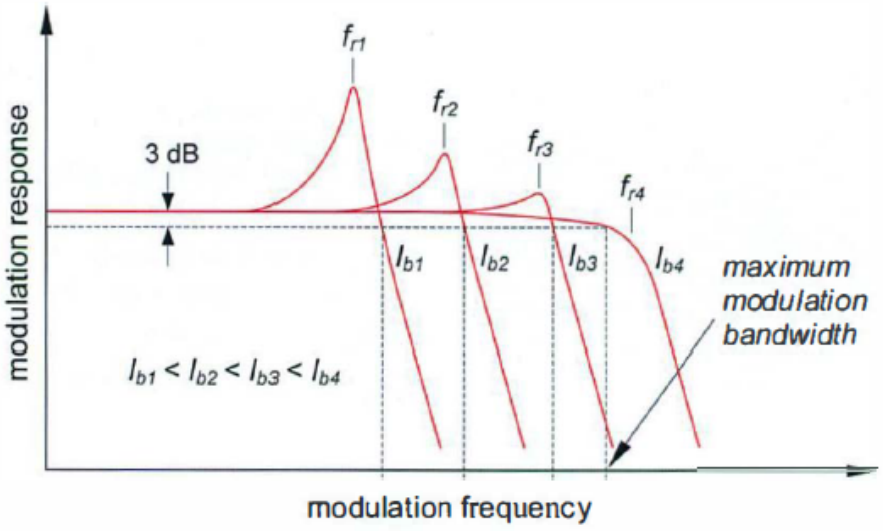

Figure 3.19: The modulation response of a semiconductor laser and its dependence on bias current.

As seen from the K-factor equation, to get a high speed laser, K-factor should be as small as possible, this can be achieved by having a short photon lifetime, high differential gain and small gain compression factor. The high differential can be achieved by using multiple quantum wells in the active region. A short cavity will guarantee a small photon lifetime. The damping considered as to be the reason for intrinsic limitation of the bandwidth, but there is extrinsic limitation as well due to thermal effects. The temperature increases with increasing the bias current since the heat dissipated in the resistive elements of the semiconductor materials. This increment in temperature will reduce the differential gain and increase the threshold current and as a consequence, the photon density will get saturated and therefore the resonance frequency at high currents.

The capacitance effect between n and p sides will cause an extrinsic limitation as well since this capacitance will form with the series resistance a low pass filter. The capacitance called the parasitic capacitance and this low pass filter will cut-off the modulation current for frequencies above the cut-off frequency. The equivalent electrical circuit of the laser shown on figure 3.20. This circuit is applied only when the bias current is above the threshold.

When calculating the frequency response of the laser, both intrinsic and extrinsic limitations should be taken into account. The complex transfer function become then:

$$H(f) = \left(\frac{f_r^2}{f_r^2 - f^2 + j\frac{f}{2\pi}\gamma}\right) \cdot \left(\frac{1}{1 + j\frac{f}{f_p}}\right) \tag{3.65}$$

Figure 3.20 shows the equivalent electrical circuit of the laser if it biased above the threshold, moreover the figure illustrates the reason behind the parasitic capacitance of a buried heterostructure laser.

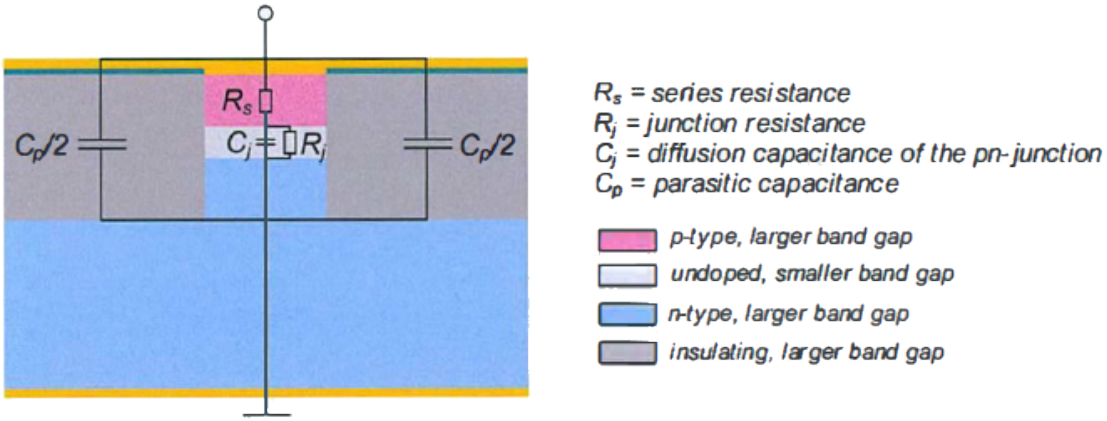

Figure 3.20: Schematic illustration of the parasitic capacitance and other electrical elements of a buried heterostructure laser, also showing an equivalent electrical circuit.

The first term accounts for the intrinsic response and the second term accounts for the capacitance effect due to RC-filter that has a cut-off frequency f_p.

A careful design of the laser will give a high modulation bandwidth which is needed to support high speed data rate communication in optical fiber communication. State of the art for Fabry-Perot laser is 40 GHz. This can be done by using multiple quantum wells which will improve the differential gain, photon lifetime can be achieved by shortening the length the cavity, heat sinking will minimize the resistance and using thick dielectric material layers will minimize the capacitance.

The other type of semiconductor laser is the surface emitting lasers which are very good choice when power efficiency and the cost are of the most importance. The modulation bandwidth is smaller than the edge emitting laser because the resistance

is much higher which will make the thermal effects is more severe which will lower the modulation bandwidth.

3.1.7.4 Large signal modulation

The previous discussions was mostly for the small signal modulation to study the high speed modulation capabilities of the laser. Small signal modulation means that the applied current is too small so that we can ignore the induced small perturbations in the photon densities and then the output power. However, in the real systems, a large signal current is applied to the laser input which cause a large variation in the output power.

Under the large signal modulation, the rise-time, fall-time and ringing appears as important features in the time domain. These features can be referred as transient behaviours. At frequencies near the resonance frequency or above, the suppression of side modes gets smaller. This will increase the spectral width and as a result, the pulse broadening will increase as the pulse propagates along the fiber. This will also increase the spectral width of each longitudinal mode as the variation of carrier density cause changes in the refractive index and therefore changes of the longitudinal mode frequencies. This phenomena of emission lines broadening known as frequency chirp.

Figure 3.21 shows the large signal analog modulation where the modulation current is superimposed on the bias current which in turn create a modulation depth of the output power.

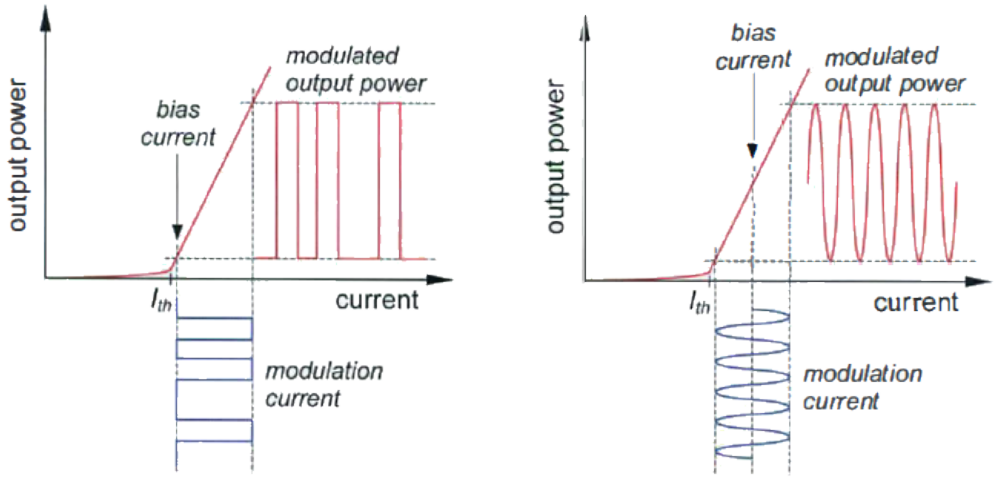

Figure 3.21: Digital (left) and analog (right) modulation of a semiconductor laser.

Figure 3.22 illustrates the transit behaviour where the ringing due to the relaxation oscillation, rise time and fall time can be seen.
In this study, we were focusing on the transmitting the RF signals along the fiber, this could be done by varying the output power with respect to the RF signal varia-

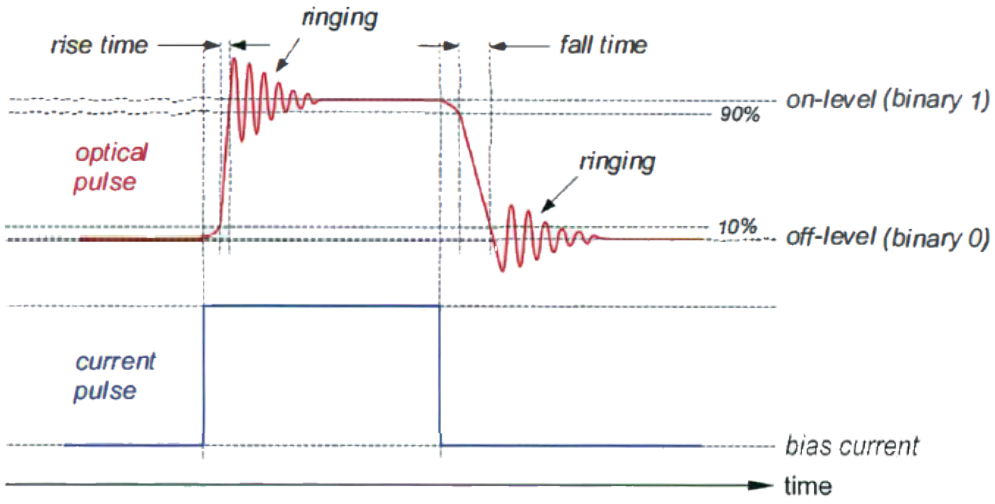

Figure 3.22: Response of a semiconductor laser to a current pulse.

tion. In this case, the bias current above the threshold current, and the modulation current has the bias current as a minimum value. One of the most important characteristics of this type of modulation is the intensity noise and the linearity of the laser since avoiding the nonlinearities in the laser will make it easier to analyse the nonlinearities for the whole system. Any nonlinearity on the output power with respect to the injected current will cause a distortion of the transmitted RF signal.

The main problem arises when using RF OFDM signals for driving the laser is the nonlinearity since it generates new frequency components at multiples of the modulation frequency known as harmonic distortion ($2f_1$, $2f_2$, $3f_2$...). If two RF signals used at the same time to drive the laser, then what known as intermodulation distortion appears since nonlinearities generate additional frequency components at the sums and differences of the modulation frequencies. The ratio between the RF power in the harmonic/intermodulation components compared to the RF power at the modulation frequency known as the degree of distortion.

3.1.7.5 Noise

The output optical wave from the single longitudinal mode laser has a constant amplitude and phase and then a fully coherent output light. But in reality, there are fluctuations on both amplitude and phase due to noise that comes mainly from the spontaneous emission in the laser. The phase fluctuations the spectral width of the emission line which known as linewidth. The amplitude fluctuations cause a the intensity noise.

As said before, the main reason of the noise is "the randomness in the carrier generation and recombination processes and the randomness of spontaneous emission into the lasing mode" [3]. Representing the electric field on the phasor form helps to understand the effects of spontaneous emission on the amplitude and phase of the light wave. This phasor is a vector that has E and Φ as an amplitude and phase

respectively. This noise adds to both amplitude as $(E + \Delta E)$ and to the phase as $(\Phi + \Delta\Phi)$. The resulting electric field that has ω_0 as the frequency of the coherent light wave can be given by:

$$E(t) = (E + \Delta E(t)) \cdot \exp j\,(\omega_0 + \Delta\Phi(t)) \tag{3.66}$$

Figure 3.23 shows the effects of the spontaneous emission on the laser field.

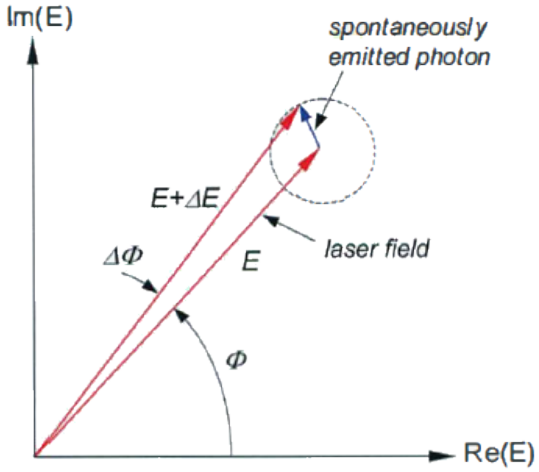

Figure 3.23: Phasor representation of the laser field and the effects of a spontaneous emission event.

The last equation shows that the field vector could be anywhere in a circle since the field amplitude variation $\Delta E(t)$ cause the intensity noise and the phase variation causes an optical frequency noise and therefore a finite linewidth since $(\Delta\omega = \delta/\delta t(\Delta\Phi))$.

3.2 Surface emitting lasers

The laser has been discussed before was edge-emitting laser where the light emitted through the cleaved edge of the cavity. This means that each laser has to be mounted and prepared before testing, which will increase the manufacturing costs. On the other hand, surface-emitting lasers where light emits perpendicularly to the surface of the wafer; this allows to test and process a batch of lasers at the wafer level. Along with other advantageous, this type of lasers is used widely in many applications and produced in large quantity.

3.2.1 VCSEL

The most popular surface emitting laser is the Vertical-Cavity Surface-Emitting Laser (VCSEL). VCSEL consists of a vertical resonator sandwiched between two Distributed Bragg Reflectors (DBRs). The upper DBR is the p-type and the lower one is n-type. The active region between these DBRs consists of multiple quantum wells (QWs) that provide optical gain. Carriers injected by forward biasing the p-n junction. DBRs utilise the constructive interference between successive reflections

in a multilayer structure. This structure consists of alternating high and low index layers where the thickness of each layer is $\lambda/4$, in this way, all reflections add in phase and the reflectivity can reach 99.9%. Multiple QWs are used to increase the efficiency of the carriers injection in the active region and this will increase the material gain for a given carrier density and increase the differential gain.

The threshold current and power consumption of the VCSEL is very small due to the small volume it has. The circular shape of the optical gain medium emits a circular beam with low divergence which ease the coupling with the optical fibers. Low fabrication and testing cost make the VCSEL a very good choice for data communication networks.

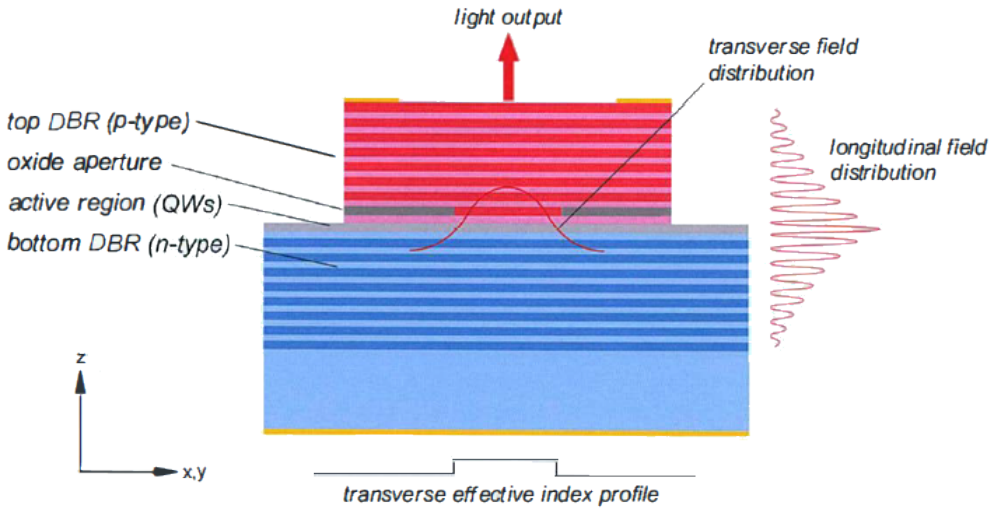

Figure 3.24: Constructions of a vertical cavity surface emitting laser of cylindrical symmetry, also showing the transverse (x-y) and longitudinal (z) optical field distributions of the fundamental transverse mode.

3.2.2 Materials and emission wavelengths

The material composition and the thickness of the QWs determine the wavelength of the VCSEL. The most common VCSEL wavelengths are 650, 780, 850, 980, 1300, and 1550 [nm]. The most used materials in the VCSEL laser are listed in the table 3.1.

The 850 [nm] VCSEL have been commercially available since 1996 and usually used for short distances fiber optic links. The 780 [nm] VCSEL used in optical storage. The 650 [nm] VCSEL used as a light source in plastic optical fiber (POF) links, sensing and printing. Higher wavelengths such as 1300 [nm] and 1550 [nm] used for longer distances fiber optic communication systems since at these wavelengths, the loss is very low.

Wavelength	Substrate	Mirrors (DBRs)	Active region
650 nm	GaAs	AlGaAs / AlGaAs	InGaP / AlGaInP
780 nm	GaAs	AlGaAs / AlGaAs	AlGaAs / AlGaAs
850 nm	GaAs	AlGaAs / AlGaAs	GaAs / A1GaAs
980 nm	GaAs	GaAs / AlGaAs	InGaAs / AlGaAs
1300 nm	GaAs	GaAs / AlGaAs	GaInNAs / GaAs
1550 nm	InP	InAiAs / InGaAiAs	InGaAs / InGaAsP

Table 3.1: Common VCSEL materials used at different wavelengths.

3.2.3 Modal behaviour

As mentioned before, the vertical structure defines the cavity and light is emitted either through the top or the bottom. The cavity length in VCSELs is not well defined since the DBRs are distributed reflectors and the effective length of the cavity is a bit longer than the cavity between the DBRs. This very short cavity makes the VCSELs single longitudinal mode laser which improves the noise and beam divergence characteristics.

One main difference between the edge-emitting laser and VCSEL is the length of the cavity. In VCSEL, the distance between the DBRs defines the cavity length which is much shorter than the cavity length of the edge-emitting laser. This makes the distance between the longitudinal modes very large and one longitudinal mode lay under the gain spectrum and VCSEL considered as single mode laser. This longitudinal mode has the field distribution as seen in the figure 3.24 and thus, the VCSEL designed so the active region placed at the field maximum in order to get maximum optical gain.

The gain inside the VCSEL cavity is very low because the optical field only get amplified when it passes through the very thin active region. The losses then should be very low as well and the DBRs have very high reflectivity to decrease the loss, and this will allow low threshold currents.

The size of the oxide aperture and the transverse effective index step determine the transverse mode characteristics. One fundamental transverse mode can be obtain by having small aperture. Larger aperture enable several transverse modes and the VCSEL then considered as multimode laser. The fundamental mode and some higher order modes can be seen in figure 3.25.

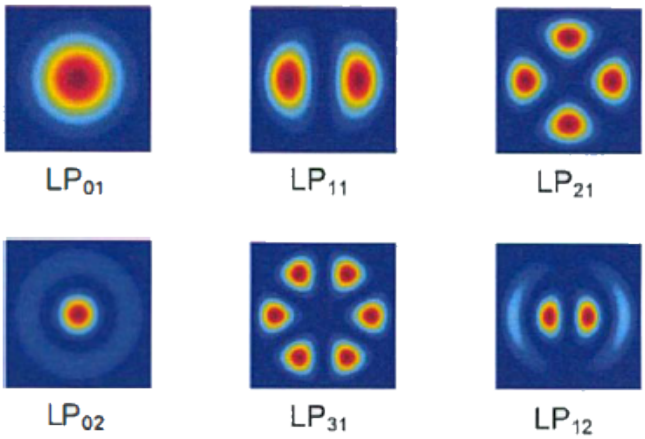

Figure 3.25: Optical field distribution in the xy-plane for the lower order transverse modes of an oxide confined VCSEL. The LP01 mode is the lowest order, fundamental mode.

The transverse modes depends on the shape, size and nature of the transverse carriers and photons confinements. The transverse optical confinement can take a form of thermal lensing, gain guiding and index guiding.

3.2.4 Techniques for current and optical confinement

The confinement of the light and current is essential for efficient operation in VCSEL. The most common four techniques for confinements are Air-post, buried heterostructure, ion-implanted and oxide confinement. In the air-post technique, the top mirror is formed as a pillar. It called like that because the index step between air and the pillar is large which guides the optical modes and confine the injected current. The air-post structured by etching a circular mesa and thus, the diameter of the active volume is defined by the mesa diameter. The index guiding is strong between the air and the semiconductor, and to ensure single transverse mode, the diameter should be very small and this causes optical scattering from the sidewall roughness. Figure 3.26(a).

Single transverse mode operation can be achieved with larger mesa using a buried heterostructure. The mesa in this case is surrounded by another semiconductor material with lower refractive index. The advantageous of this method are giving lower index guiding and passivate the active region sidewalls. The semiconductor is better heat conductor than air which improves the thermal characteristics. Figure 3.26(b).

The idea in the ion-implanted technique is to create region of high resistivity by creating a crystal vacancies in the material outside the centre region and this will provide concentration of the injected current into the centre region. Figure 3.26(c).

The confinement of carriers and photons can also be done using a selective oxidation of the AIGaAs layer. This layer has high Al concentration that placed between

the top DBR and the active region. This layer is electrically isolated and therefore guides the carriers throw the aperture structured by the oxide layer. The photons confinement can be done using this layer where the refractive index is smaller than the other layers and this provides a transverse index step that create an optical waveguide which in turn confines photons. Figure 3.26(c).

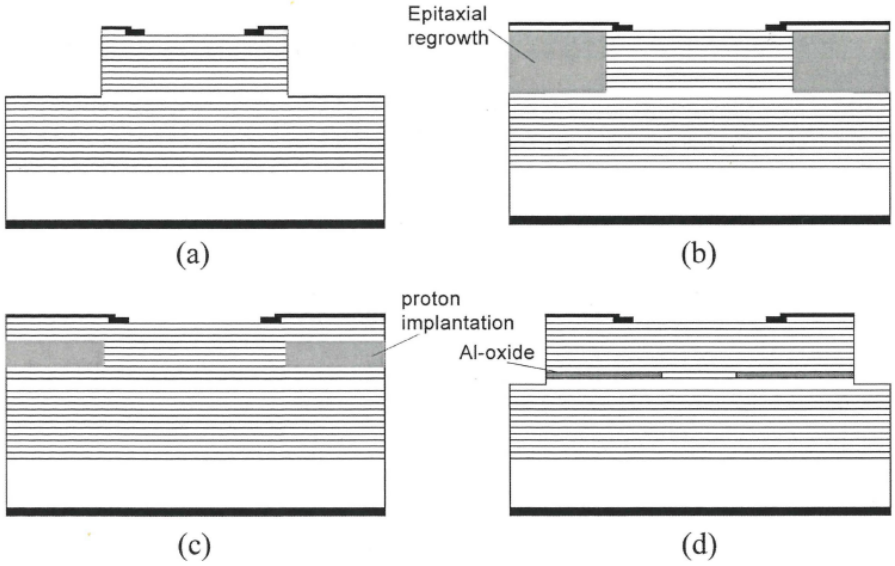

Figure 3.26: Cross sections of basic VCSEL designs: a) air-post, b) buried heterostructure, c) ion-implanted, d) oxide confined.

4

The simulation setup and the arisen problem

4.1 Introducing the problem

Figure 4.1 illustrates the system setup where, the signal generation occur in the Matlab where multiple signals have been investigated. The Matlab output block will be injected in a user defined VCSEL block, after that, the fiber link and the photo detector is inserted. The output of the photodetector is injected in a Matlab block to simulate and evaluate the results.

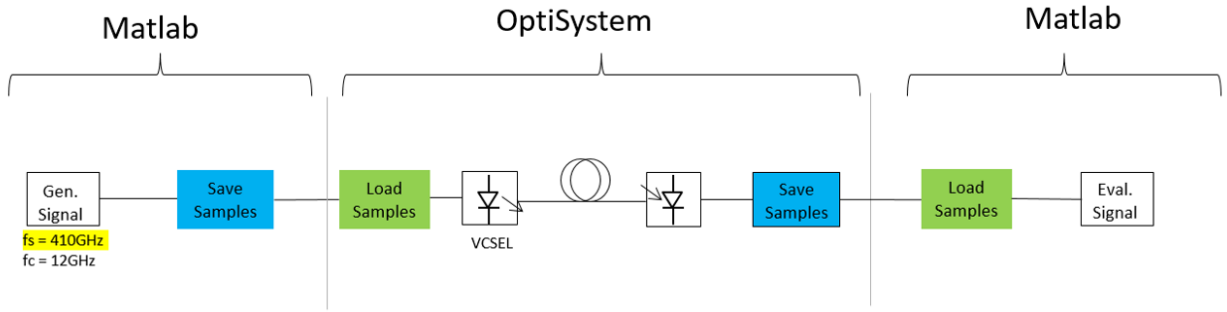

Figure 4.1: System setup

4.1.1 One tone evaluation

The first signal injected into the system is one tone sinusoidal signal. Figures 4.2 and 4.3 show the input and the output signals. In figure 4.2, the bias current is 10 [mA] and the modulation current is $\sim$ 1.4 [mA]. The input signal has the same amplitude, but the frequency increased gradually.

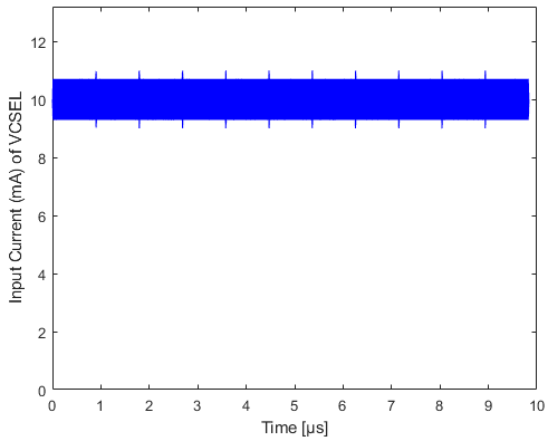

Figure 4.2: Input One Tone signal

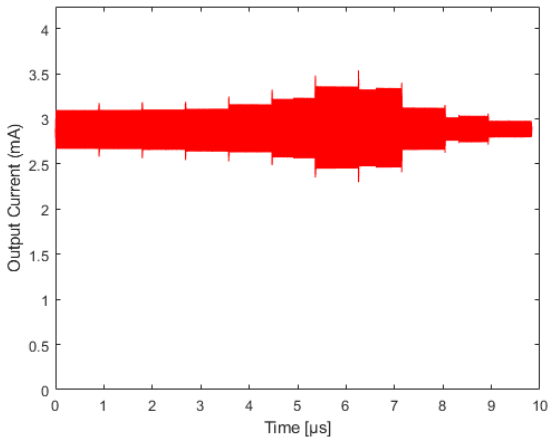

Figure 4.3: Output One Tone signal

Apparently, the output signal get distorted at frequencies between 15 and 24 [GHz]. The signal gets amplified from ~ 6 [GHz] until frequency 18.2 [GHz], then it starts to decay and compressed for frequencies > 18.2 [GHz]. To confirm this behaviour, S_{21} plot would help understanding what is going on. Figure 4.4 illustrate the S_{21} plot confirming that the amplification starts ~ 6 [GHz] and the decay around 18.2 [GHz].

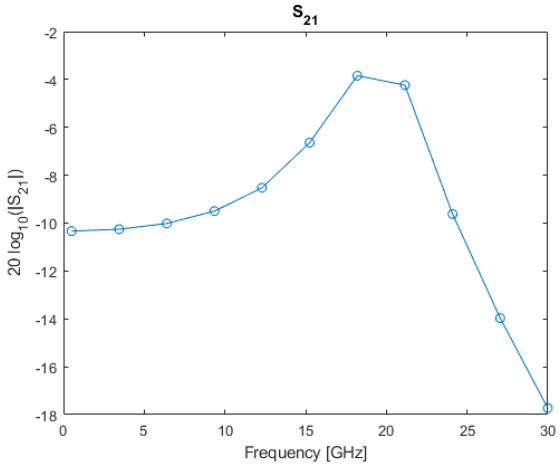

Figure 4.4: S_{21} of one tone signal

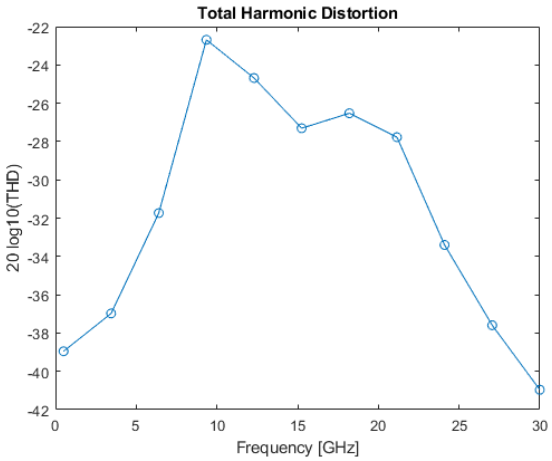

Figure 4.5: THD of the output signal

It would be helpful to illustrate the Power Spectral Density (PSD) of the input and output at a frequency where a signal get distorted, figures 4.6 and 4.7. The frequency chosen is 15.2 [GHz]. As been seen, many unwanted harmonics have been appeared at frequencies of $2f$, $3f$, $4f$ etc.

Total Harmonic Distortion (THD) would give good indicate how the signal is distorted and at which frequencies. Figure 4.5 illustrates the THD of the output signal. As seen, the max distortion occur at ~ 9.3 [GHz] and it decreased with increasing the frequency.

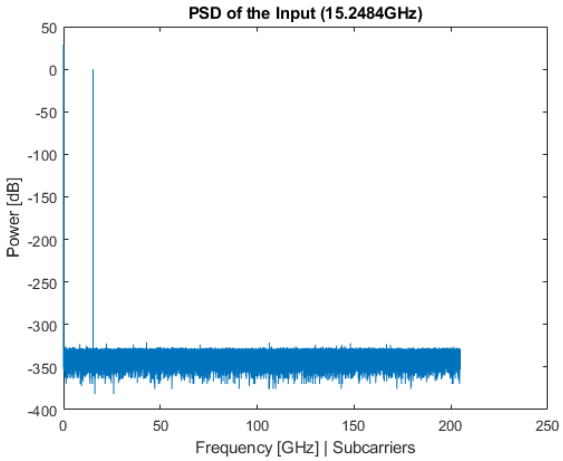

Figure 4.6: PSD of the input signal at frequency = 15.2 [GHz]

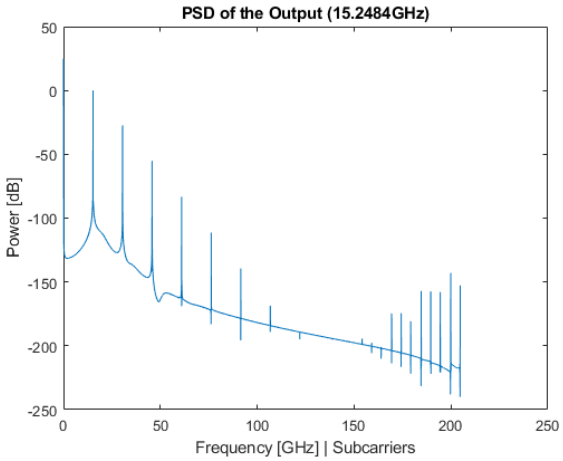

Figure 4.7: PSD of the output signal at fundamental frequency = 15.2 [GHz]

4.1.2 Two tone evaluation

The second signal injected into the system are two tone sinusoidal signals. Figures 4.8 and 4.9 show the input and the output signals. The input signal is two sine wave signals at frequencies of 4.4496 [GHz] and 4.5504 [GHz] where two tones are 100.8 [MHz] apart. The amplitude of the input signal increase gradually to check how the modulation depth can affect the performance and to be able to plot IIP3 and OIP3 later.

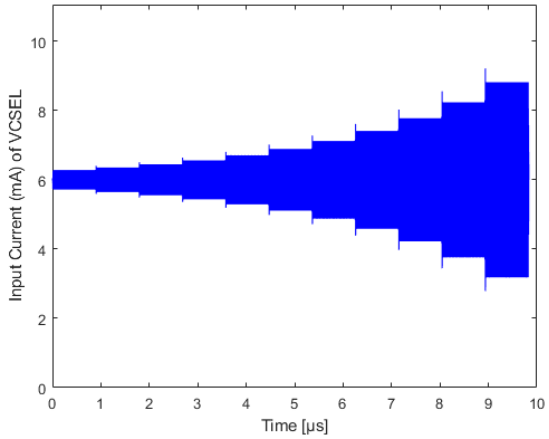

Figure 4.8: Input signal of two tones sinusoidal signals

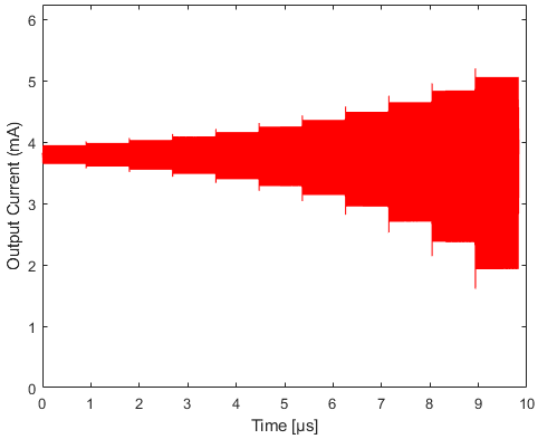

Figure 4.9: Input signal of two tones sinusoidal signals

In the same fashion as the one tone case, the output signal gets distorted because of the new harmonics appears at the output.

Figures 4.10 and 4.11 illustrate the PSD for the input and the output signals. The input signal is basically two tones sinusoidal signals with 100.8 [MHz] apart. Addi-

tionally to the harmonics appears at $2f_1$, $2f_2$, $3f_1$, $3f_2$, $4f_1$, $4f_2$ ..., it can be seen new harmonics at $2f_1 - f_2$, $2f_2 - f_1$, $2f_1 + f_2$, $f_1 + 2f_2$, etc. These harmonics called for intermodulation distortions.

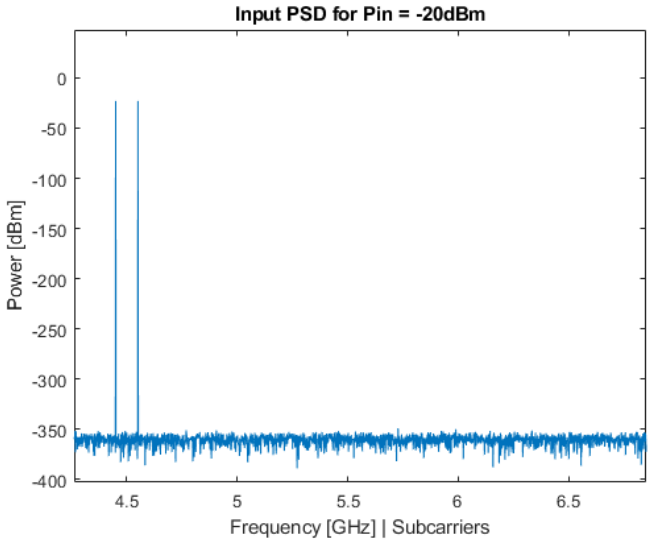

Figure 4.10: PSD of the input signal

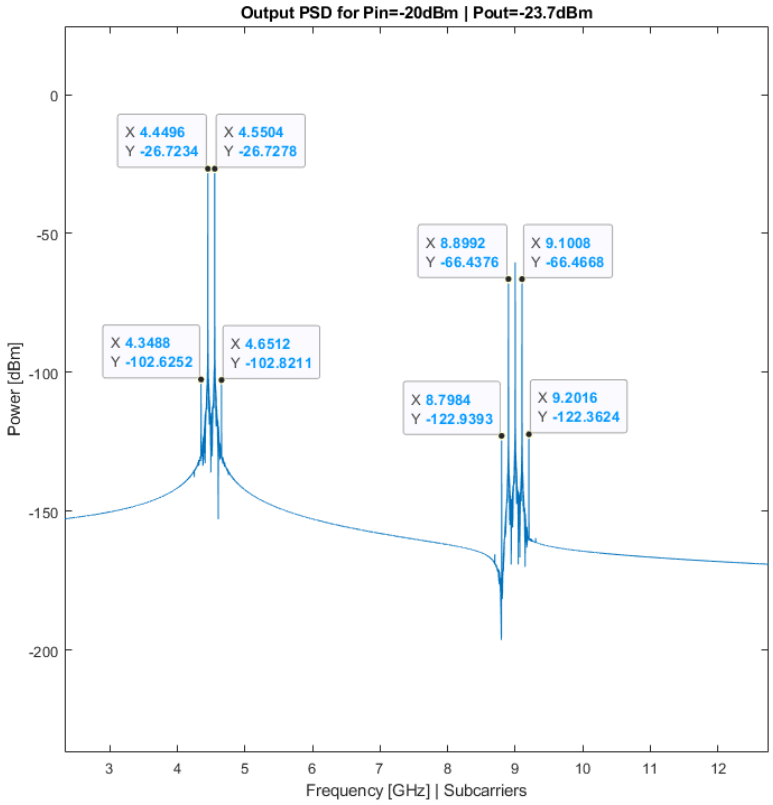

Figure 4.11: PSD of the output signal

Figure 4.12 illustrates the Output Second-order intercept (OIP2), point, Input Second-order intercept point (IIP2), Output Third-order intercept point (OIP3) and Input Third-order intercept point (IIP3). As can been seen, IP2 affects the fundamental signal before IP3 which means that the second order harmonics have more effect on the output signal than the third order harmonics.

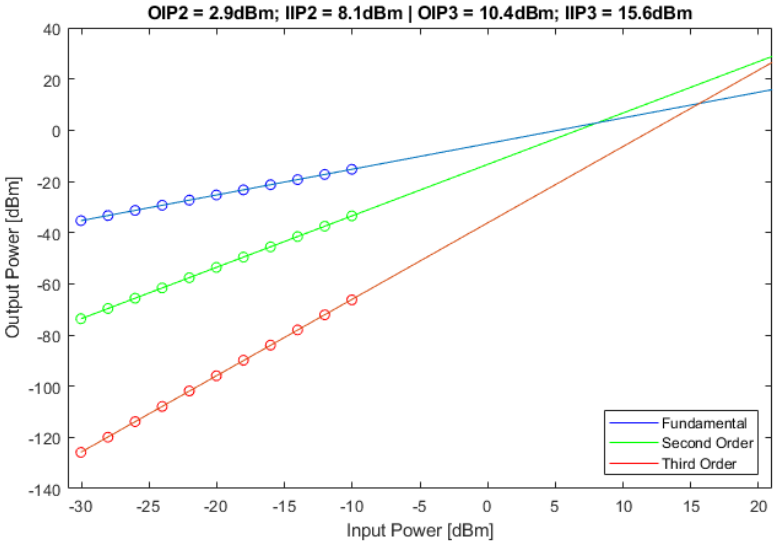

Figure 4.12: OIP2 and OIP3 of the output signal

4.1.3 One OFDM signal evaluation

In the same fashion, the signal inserted in the same RoF system is one OFDM signal at 3 [GHz]. Figure 4.13 presents the setup of the system where the Matlab block generates the OFDM signal which injected into the VCSEL. The VCSEL output injected in a multimode fiber. A photodetector converts the signal back from optical to electrical which injected into a Matlab block to evaluate the output signal.

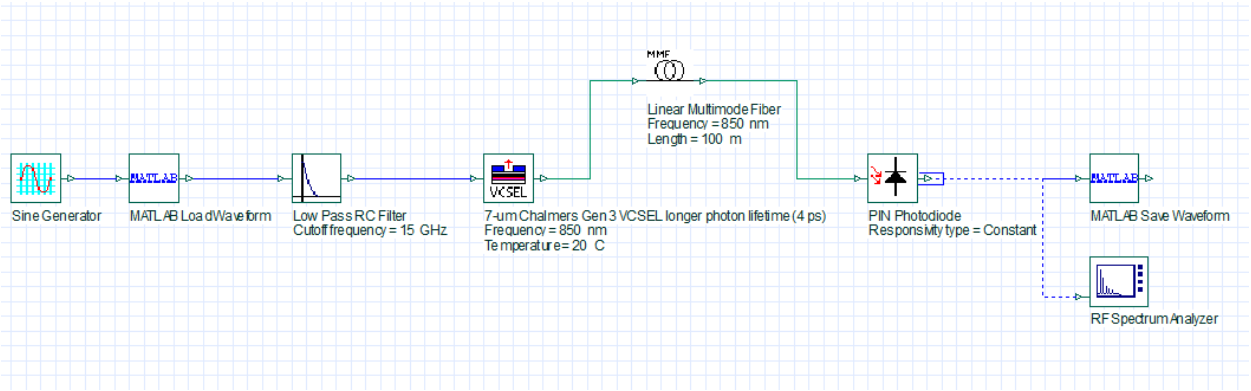

Figure 4.13: System setup in OptiSystem

The input and output signals illustrated in figures 4.14 and 4.15. It can be shown

that the output signal get distorted due to nonlinearities occur along the system.

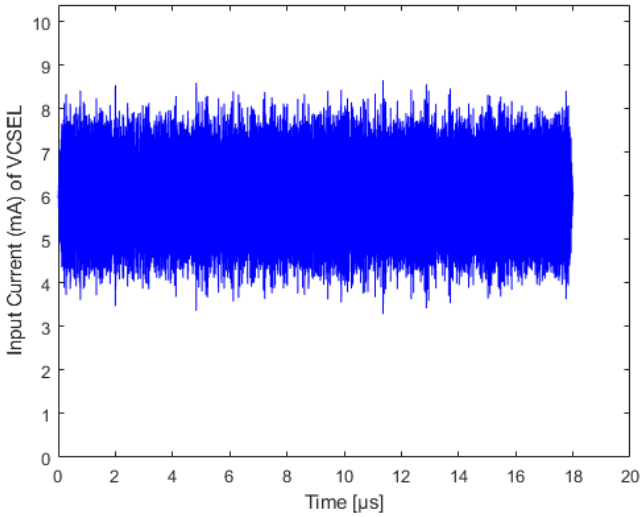

Figure 4.14: Input signal of one OFDM signal

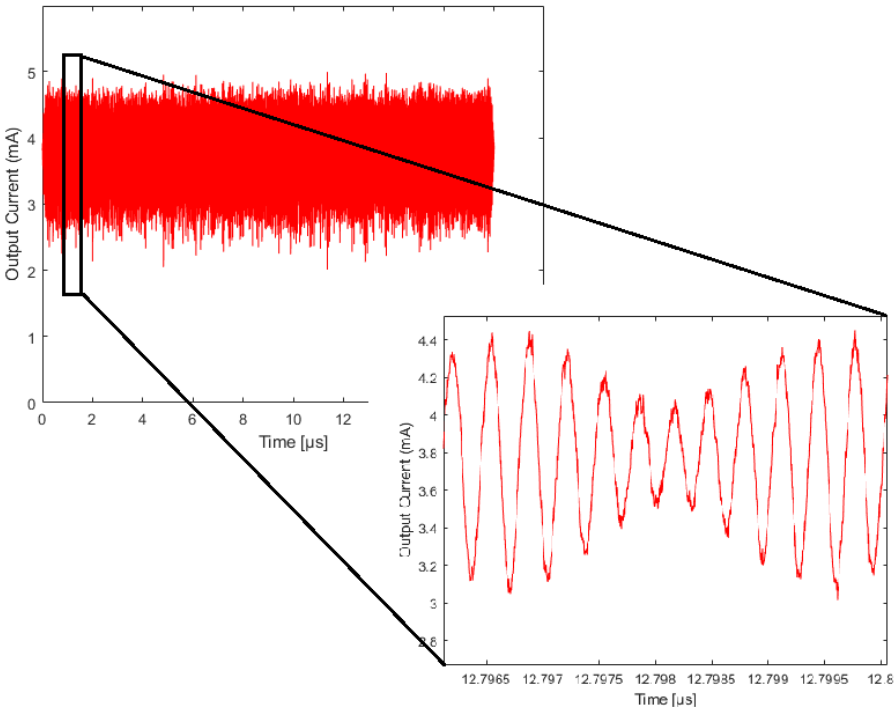

Figure 4.15: Output signal and distortion affect the signal

Error Vector Magnitude (EVM) is a measure used to check the performance of a digital transmitter or receiver. Figure 4.16 illustrates the EVM of the output signal at 3 [GHz].

$$EVM(dB) = 10\log_{10}\frac{P_{error}}{P_{reference}} \tag{4.1}$$

$$EVM(\%) = \sqrt{\frac{P_{error}}{P_{reference}}} \times 100\% \tag{4.2}$$

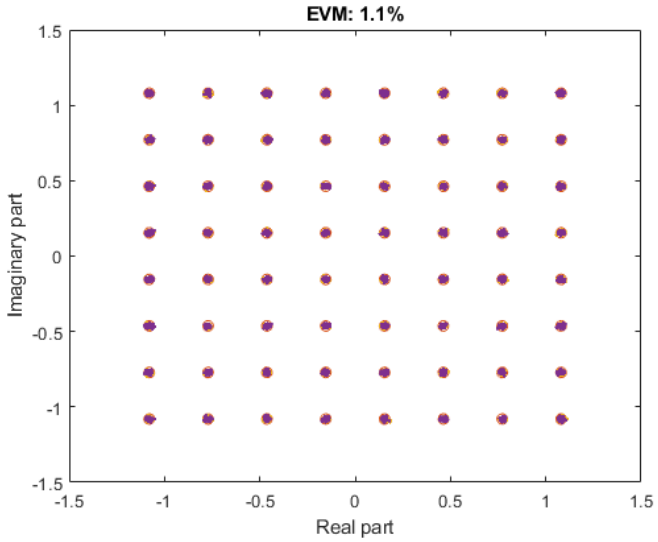

Figure 4.16: Error Vector Magnitude of one signal OFDM

Adjacent Channel Power Ratio (ACPR) is the ratio between the total power of the adjacent channel to the reference channel's power. ACPR is illustrated in figure 4.17 of the output signal.

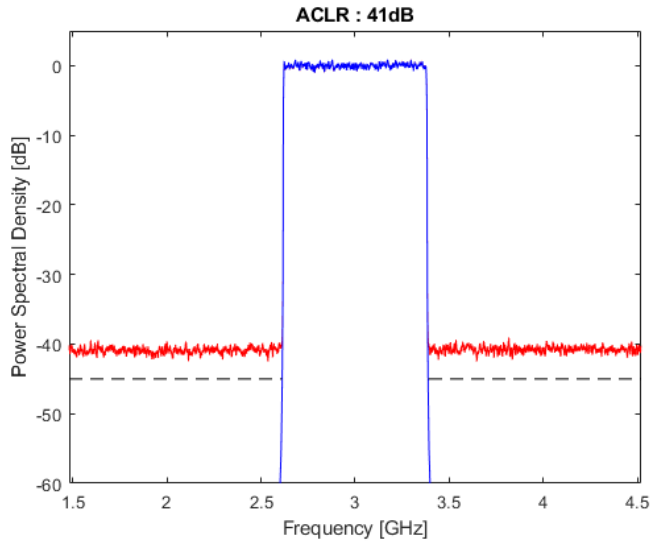

Figure 4.17: Adjacent channel power ratio for one OFDM signal at 3 GHz

Increasing the frequency to 6.5 [GHz] will cause more distortion, figure 4.18. The reason behind this increment will become more clear at chapter 5.

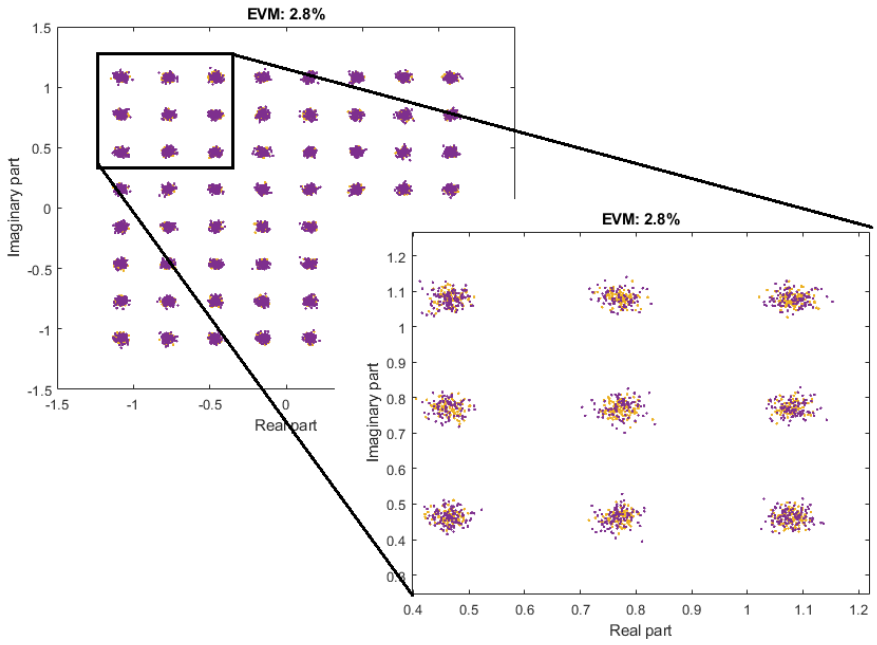

Figure 4.18: Adjacent channel power ratio for one OFDM signal at 6.5 GHz

4.1.4 Two OFDM signals evaluation

The input signal here is two OFDM signals. Apparently as the two tone case, new harmonics are created at $2f_1$, $2f_2$, $f_1 + f_2$, $f_2 - f_1$. Signals transmitted at these products will see additional distortion, figure 4.19.

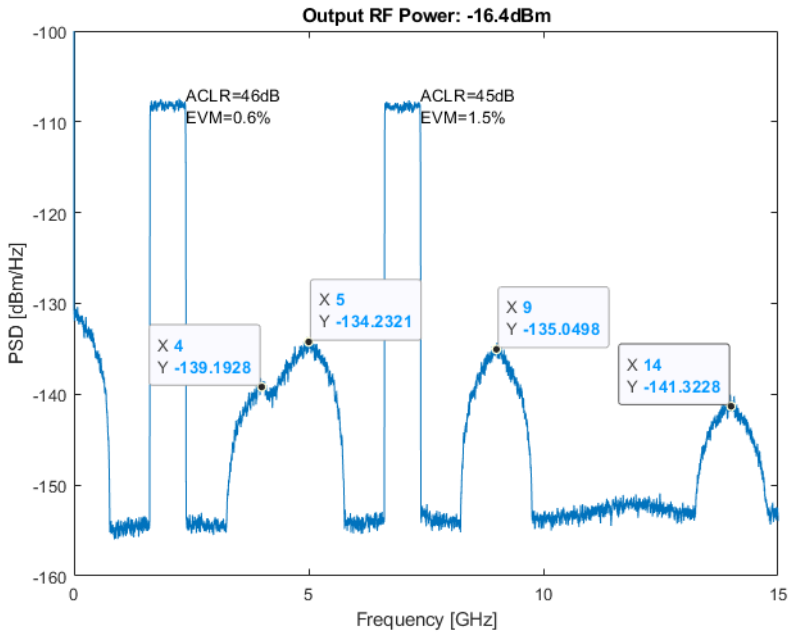

Figure 4.19: Output signal of two OFDM signals at the input

A comparison between the one OFDM and two OFDM signals can be seen in figure 4.20. Adding more OFDM signals will produce more harmonics which will degrade the performance.

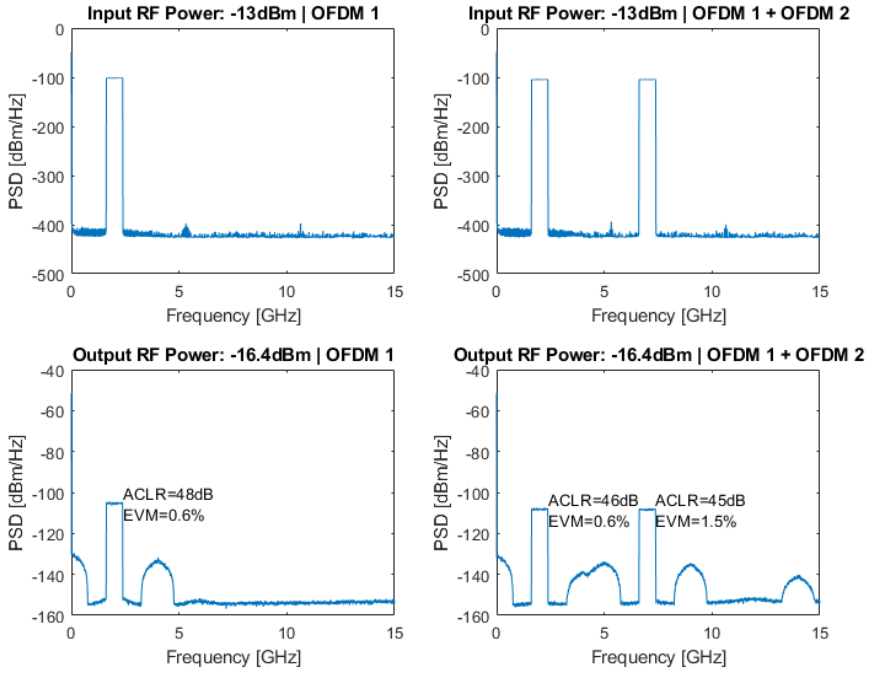

Figure 4.20: Distortion comparison between one and two OFDM signals

EVM of one OFDM signal, OFDM1 and OFDM2 for the first signal and OFDM1 and OFDM2 for the second signal can be seen in figure 4.21. Apparently EVM get larger by adding more signals to the system.

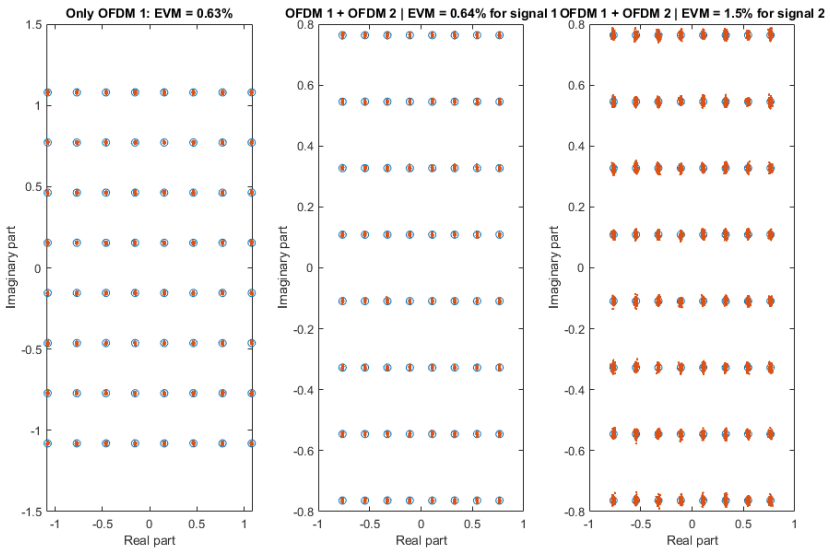

Figure 4.21: EVM for two OFDM signals

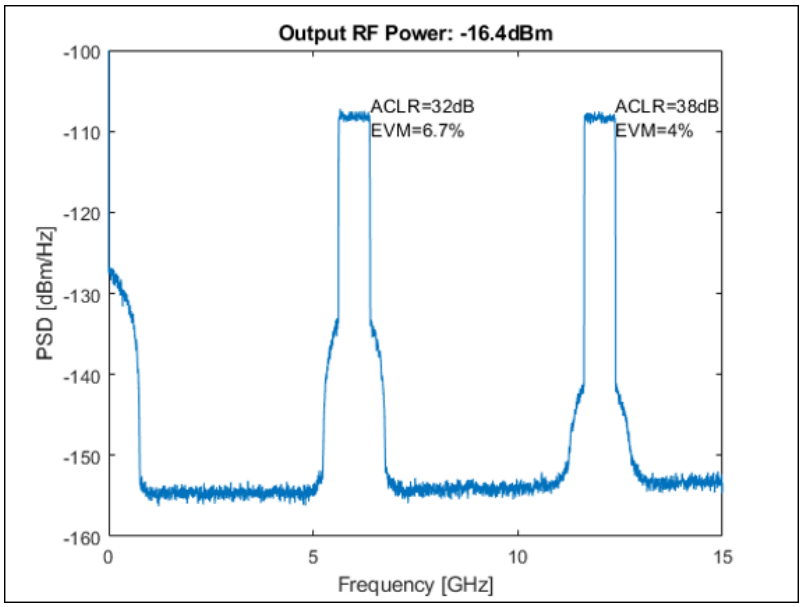

Figure 4.22: EVM for two OFDM signals

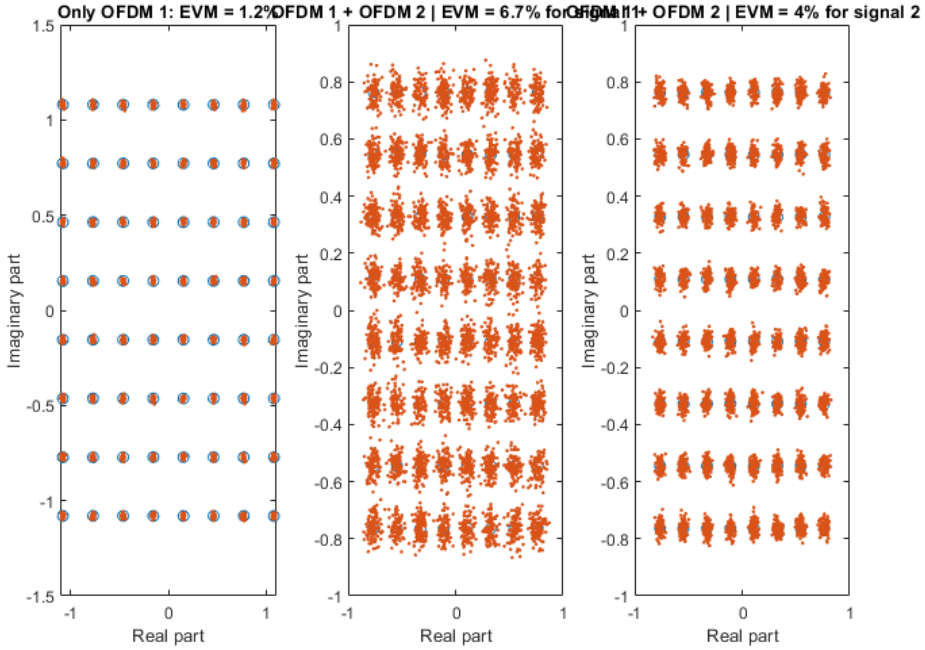

Figure 4.23: EVM for two OFDM signals

In the first case, OFDM signals get send at 2 and 7 [GHz] respectively. It can been seen that new harmonics get generated at 4, 5 9 and 14 [GHz]. However as long as the OFDM signal does not overlap another signal product, the performance and quality still very good since the ACLR $\sim$ 46 [dB] and EVM $\sim$ 1.5% at its maximum.

In the second case, OFDM signals get send at 6 and 12 [GHz] respectively. It can been seen that the signals get distorted dramatically since the ACLR decreased to

32 dB comparing with 42 [dB] at the first case. This is obvious because each signal now overlap the new harmonics generated from the other signal. This degraded the performance since as can be seen from the EVM that it increased from 0.64% to 6.7%.

The question now, where this nonlinearity comes from, is it from the laser, the optical fiber or from the photodetector? This is what will be discussed in next chapters.

5

VCSEL Nonlinearity

In Radio over Fiber (RoF) networks, fiber optic is used to distribute radio frequency signals. Small cell size in 5G is required to improve the coverage and get high capacity and this means increasing in the number of the RoF links which will increase the costs. Making the unit cell simple and using low cost components for each link will lower the costs dramatically. As we discussed before, VCSEL offer a very good solution for Laser-Fiber coupling. Using high bandwidth multimode fiber along with VCSEL can provide a very good dynamic range that is needed for various mobile communication networks [27].

5.1 VCSEL Nonlinearity

The most nonlinearity effects in the VCSEL laser represented in the second-order harmonic distortion and third-order intermodulation distortion. At a specific modulation frequency, the nonlinearity distortion will get its minimum. Before that frequency, the distortion is come mainly from Spatial Hole Burning (SHB) effect. After that frequency, the distortion is dominated by the relaxation oscillation effect. At this frequency, these two types of distortions cancel out, and this results a significantly low distortion.
This behaviour is slightly different between single mode and multimode lasers, since in multimode, the behaviour is more unpredictable due to mode competition. The distortion comes from one mode can be much larger than the distortion of total output power. This explain why it is important to avoid mode-selective losses in multimode applications.

In RoF links, the analogue signals distortion comes from the nonlinearities. The main physical processes that cause nonlinearities are; the relaxation oscillation, spatial hole burning, gain suppression and leakage currents [28].

5.2 Harmonic Distortion

The performance of the RoF system depends on the nonlinearity of the system. The main source of nonlinearity in the RoF link is the laser diode that exhibits a relatively large nonlinear behavior. The two most nonlinearity drivers in the VCSEL are Spatial Hole Burning (SHB) and Relaxation oscillation (RO).

5.2.1 Spatial hole burning

Spatial hole burning: "A distortion of the gain shape in a laser medium (or the loss spectrum in a saturable absorber medium), caused by saturation effects of a standing wave" [31]. And SHB implies a non-uniform transverse carrier density distribution in the quantum wells which caused by non-uniform transverse photon density distribution in the cavity. This non-uniformity will gives rise of modal gain and modal loss which depends on the photon density. The fluctuations in the free carrier density is significantly non-uniform at low frequencies due to perturbation of the current. However, in the central region, this fluctuation is suppressed because the differential carrier lifetime is rather small. In the centre region (< 3 micron), the photon density is high and this cause to an intense stimulated recombination. This short differential carrier lifetime will prevent any significant change in the carrier density with changing the modulation current. Outside the core region (> 3 micron), the differential carrier lifetime is rather long because of low photon density. This will cause large fluctuations in the carrier density with changing the modulation current.

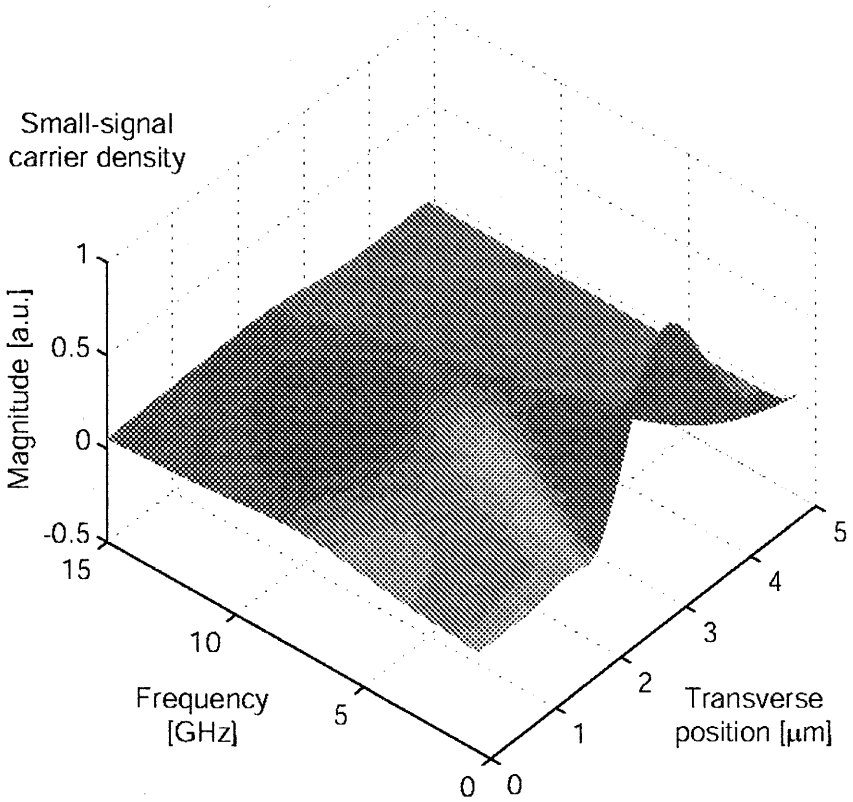

Figure 5.1: Magnitude of the small-signal carrier density distribution in the quantum wells for the single-mode VCSEL [29]

At high frequencies, the modulation period is much shorter than the differential carrier lifetime and this means that the carriers captured in the quantum wells survive a full modulation period. The carrier density fluctuation is only determined by the number of carriers provided by the small signal current. This number decreases the modulation period and then the carrier density fluctuation decreases with frequency.

As can been seen in figure 5.1, fluctuations in carrier density is very small at every transverse position for frequencies above 2 [GHz]. This frequency is called the cutoff frequency for spatial hole burning and it is in a range of 1-3 [GHz] [30].

5.2.2 Relaxation Oscillation

In semiconductor lasers, the distortion has its maximum value near the relaxation oscillation frequency (f_r), as can be seen from figures (5.3, 5.4 and 5.5). f_r is around 4, 12 and 10 [GHz] respectively. The second harmonic distortion in the first region is characterized by a narrow bump and in the second region, it is characterized by a broad double peak structure. This peaks located at f_r and $f_r/2$. The shape of these peaks (smoothness and strength) depends on the carrier diffusion and the gain suppression.

It has been noticed that increasing the bias current will cause the transition between the two regions shifts to the higher frequencies as well as the distortion reduced. These peaks in the second region start to be less distinguishable as bias current increases and the reason is larger photon density will lower the fluctuations in the carrier density distribution and increase the damping process of the relaxation oscillation.

However, increasing the bias current will not decrease the distortion forever. At very high bias current, the photon density will cause the gain suppression becomes the dominant distortion source. Finally, in the single mode, increasing the modulation depth will increase the distortion.

As discussed before, the dip occurs at lower frequency and shifts a bit to higher frequencies when the bias current is increased. In multimode case, lower photon density will cause reducing the f_{SHB} and relaxation oscillation as well at lower bias currents. On the other hand and at higher bias currents, f_r has higher values than single mode case because of the low gain suppression. In this case, the distortion in the first region is low and the mode competition cause unpredictable distortion behaviour. In the second region, the distortion is higher comparing with single mode case because the lower photon density reduces the damping of the relaxation oscillation.

As can be seen in figure 5.2 where a comparison between the total HD2 and the individual HD2 of the three most modes in the multimode VCSEL. The output power of LP_{21} is much higher the average output power of LP_{02} and LP_{01}. The mode LP_{21} in the first region has the lowest distortion because of the high photon density. However the distortion comes from individual mode is much higher the sum from all modes.

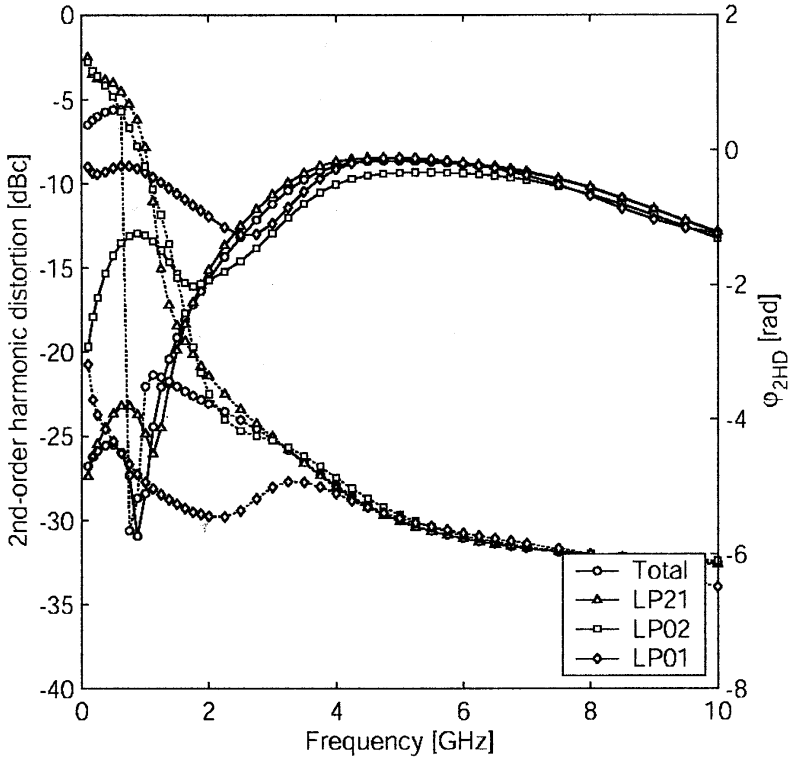

Figure 5.2: Simulated second-order harmonic distortion of the individual LP_{21}, LP_{02}, and LP_{01} modes in the multimode VCSEL [29]

One mode can influence another modes strongly. However, the total output is unaffected which means that the distortion from one individual mode is unlikely to be lower than that of all summed modes. Most sensitive modes are those that have a large overlap of their respective mode profiles and when the spatial distribution of carriers vary significantly during a one cycle of the current modulation. That is why the influence of mode competition is more pronounced at low frequencies (spatial hole burning region). While at high frequencies (relaxation oscillation region), the individual modes start to be more independent of each other which cause the distortion behaviour is similar to single mode in the second region.

It is very important to collect power from all modes in case of multimode VCSEL. Because as been discussed, one mode individually can cause more distortion than the distortion comes from all modes. And this is more important in subcarrier multiplexing applications (SCM) [32]. In these applications, high level of distortion comes from relaxation oscillation is unacceptable, that is why the transmission band should be well below the relaxation oscillation frequency.
The lower and higher frequency regions are characterized by a narrow bump and a broad double-peak structure, respectively.

5.2.3 Second Order Distortion - HD2

Figures (5.3, 5.4 and 5.5) present the second order distortion for three different VCSELs. As can be seen, a sudden change in HD2 and Φ_{HD2} will separate HD2

distortion graph into two regions, the left one is the distortion mainly comes from spatial hole burning (SHB) where it starts roll off due to the large time constant it has. The right part is then the distortion dominated by the relaxation oscillation. At this sudden change point, a dip in distortion can be seen. And this is because of the out of phase between the spatial hole burning and the relaxation oscillation. At very low frequencies, less than 1 MHz, the output modulation will be the projection of the input modulation on to the light-current curve.

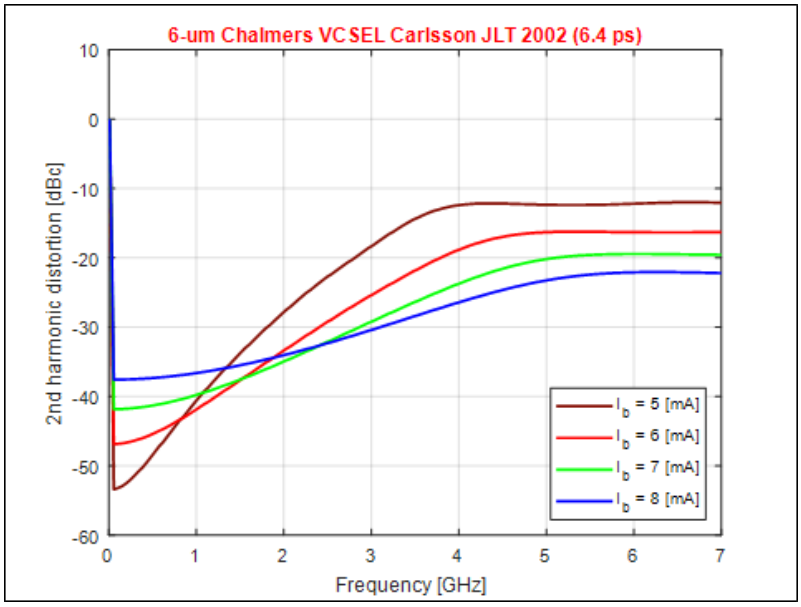

Figure 5.3: Simulated HD2 as a function of modulation frequency for the VCSEL: 6-um Chalmers VCSEL Carlsson JLT 2002 (6.4 ps)

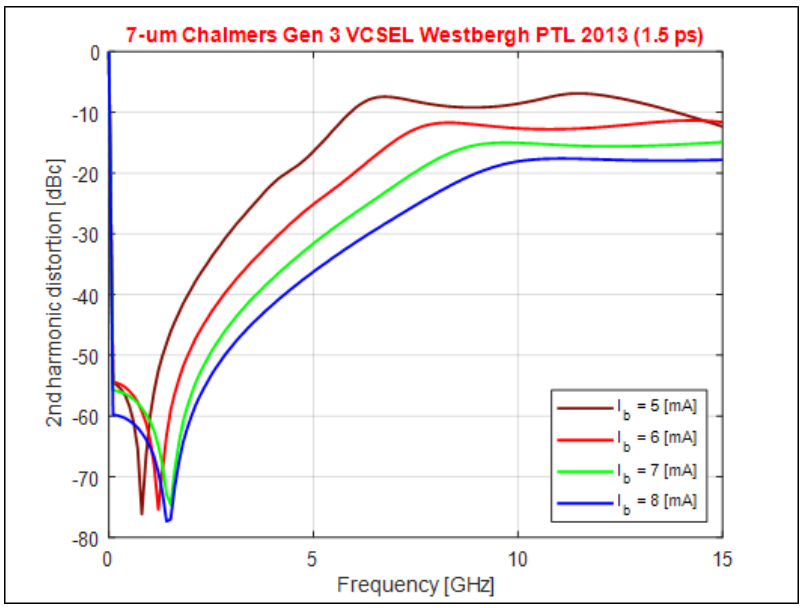

Figure 5.4: Simulated HD2 as a function of modulation frequency for the VCSEL: 7-um Chalmers Gen 3 VCSEL Westbergh PTL 2013 (1.5 ps)

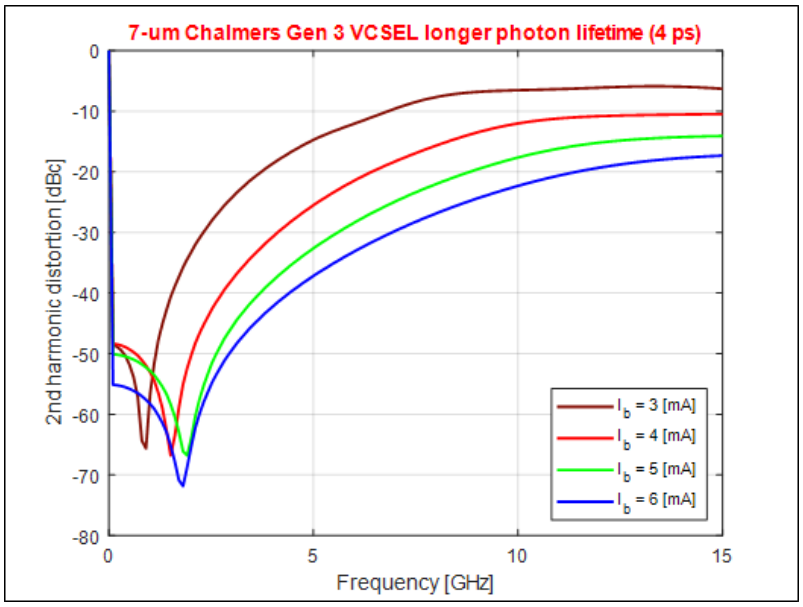

Figure 5.5: Simulated HD2 as a function of modulation frequency for the VCSEL: 7-um Chalmers Gen 3 VCSEL longer photon lifetime (4 ps)

The previous analysis was mainly for SHB and RO. The influence of gain suppression results an identical distortion curve at frequencies below the cut frequency and at higher frequencies. The relaxation oscillation gets slightly dampened which results a low distortion with few dBs.

5.2.3.1 Second Order Distortion with respect to temperature

Figure 5.6 presents the second-order modulation distortion with respect to the temperature. It is change from VCSEL to VCSEL but taking "7-um Chalmers Gen 3 VCSEL Westbergh PTL 2013 (1.5 ps)" as example, it can be seen that there is a dip or a minima in the IMD3 profile at specific temperature and this dip shifts to the lower temperatures when increasing the bias current. This most probably happens because of the de-tuning inside the active region where the gain profile and the longitudinal mode do not shift in wavelength in the same rate when changing the temperature. It seems that the longitudinal mode meets the maximum of the gain spectrum at these specific temperatures.

5.2.4 Third-order Intermodulation Distortion - IMD3

Intermodulation distortion defined as the spectral power at the sum and subtract frequencies of modulation frequencies. Sometimes, the sum and difference located very close to the modulation frequencies and it can fall within the narrow transmission band. That is why the intermodulation distortion is very important in multicarrier applications such SCM or OFDM.
We define the frequencies in intermodulation distortion as two closely spaced frequencies (f and $f + \Delta f$). Using Fourier transform, the spectral power can be

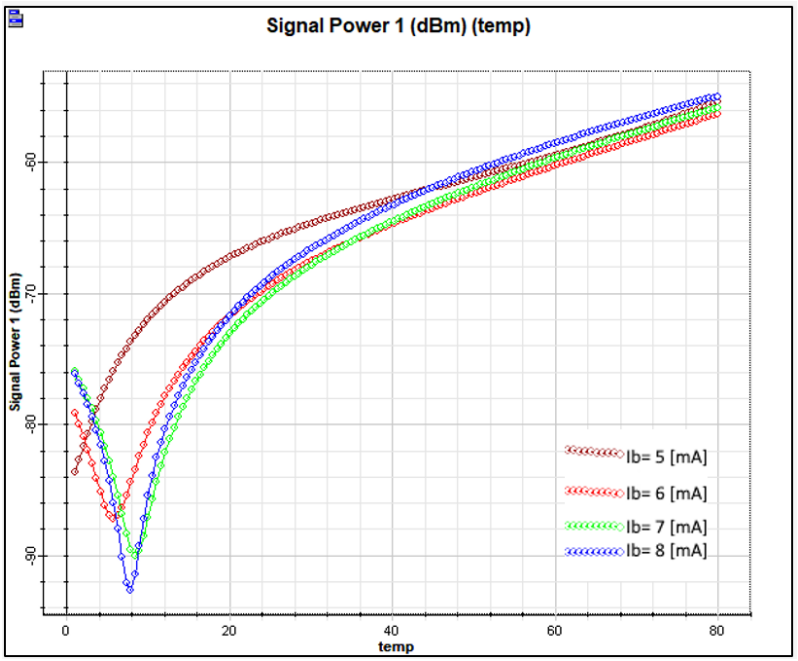

Figure 5.6: Simulated HD2 as a function of temperature @ 2 [GHz] for the VCSEL: 7-um Chalmers Gen 3 VCSEL Westbergh PTL 2013 (1.5 ps)

obtained. The third-order intermodulation distortion (IMD3) will be the spectral power at $f - \Delta f$ and $f + 2\Delta f$.

The distortion behaviour with respect to frequency of IMD3 and HD2 is similar. Figures (5.7, 5.8 and 5.9) present the third order intermodulation distortion for the same three different VCSELs. In the same fashion as HD2, a sudden change in the IMD3 will separate IMD3 distortion graph into two regions, the left region at low frequencies caused mainly by SHB and the right region at higher frequencies caused mainly because of the relaxation oscillation. In the first region, IMD3 characterized by a narrow bump and a broad single-peak structure in the second region. This broad single-peak located at f_r and if the damping of the relaxation oscillation is low, then the second peak will start to be distinguishable. and it will be located at $f_r/2$ [33][34].

The average power at the new generated frequencies $f - \Delta f$ and $f + 2\Delta f$ is given by dBc which is decibels to the carriers at f and $f + \Delta f$ respectively. Similar to HD2, the distortion in the first region is dominated by the SHB and by the RO in the second region.

Figure 5.10 illustrates the simulated IMD3 with respect to the modulation frequency for single mode and multimode VCSEL at different modulation depths and bias currents. In the same fashion as HD2, a dip around 1-2 [GHz] can be seen which will separate the frequency domain into two regions. Again, as HD2, the distortion is dominant by the spatial hole burning and the relaxation oscillation in the first and second region respectively. Increasing the bias current and the modulation depth

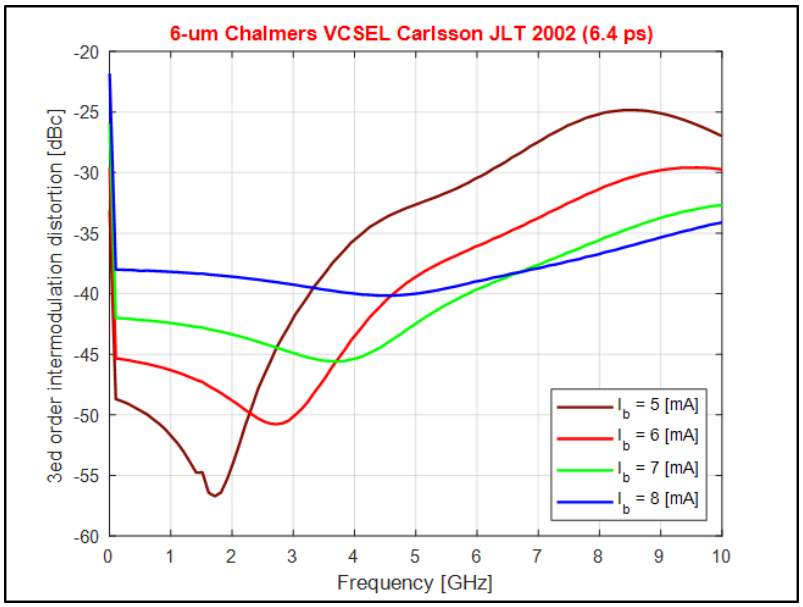

Figure 5.7: Simulated IMD3 as a function of modulation frequency for the VCSEL: 6-um Chalmers VCSEL Carlsson JLT 2002 (6.4 ps)

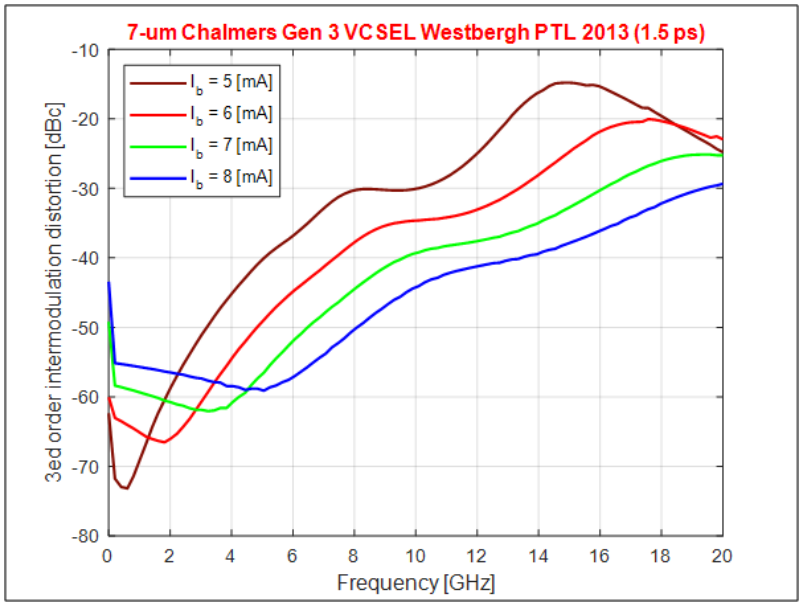

Figure 5.8: Simulated IMD3 as a function of modulation frequency for the VCSEL: 7-um Chalmers Gen 3 VCSEL Westbergh PTL 2013 (1.5 ps)

will give the same behaviour as HD2, figure 5.10 (a) and (c). Increasing these values in the multimode case 5.10 (b) and (d) shows similar differences compared to the single-mode case as does the HD2.

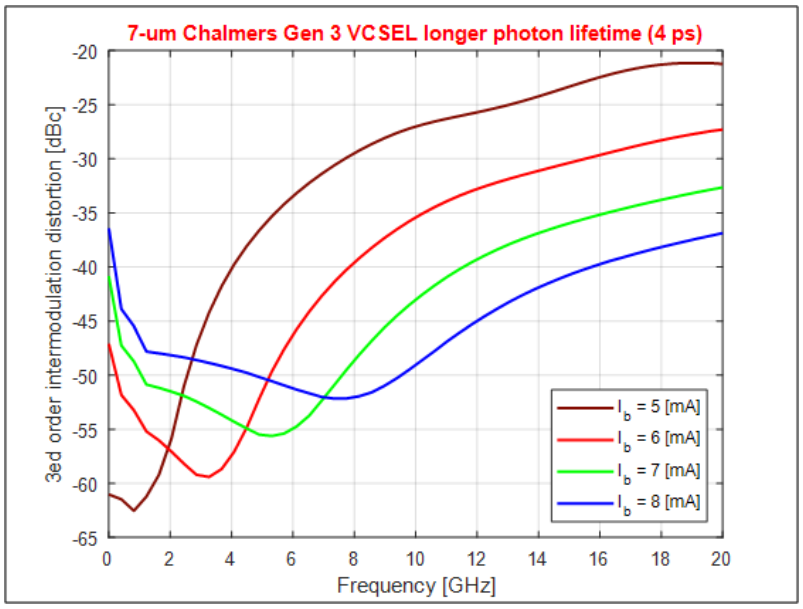

Figure 5.9: Simulated IMD3 as a function of modulation frequency for the VCSEL: 7-um Chalmers Gen 3 VCSEL longer photon lifetime (4 ps)

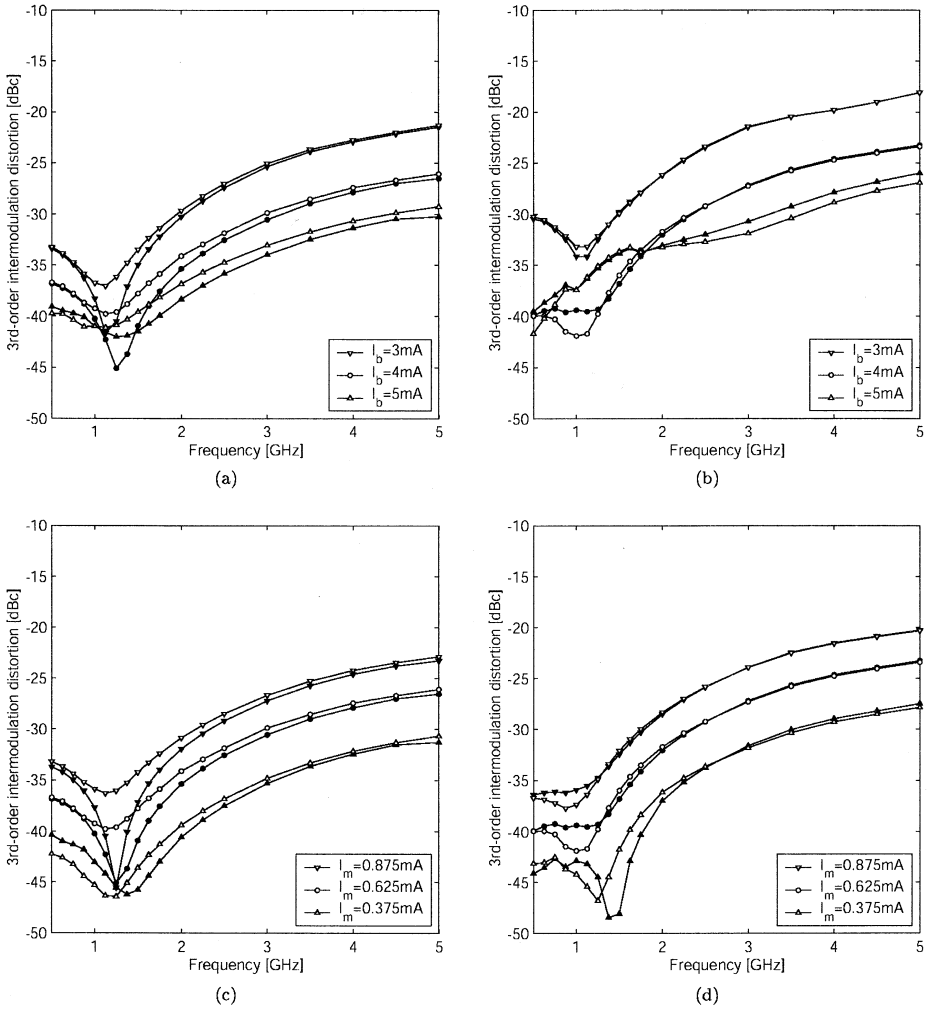

Figure 5.10: Simulated IMD3 for $\Delta f = 10$ MHz as a function of modulation frequency. [29]

5.2.4.1 Third-order Intermodulation Distortion with respect to temperature

Figure 5.11 presents the third-order intermodulation distortion with respect to the temperature. It is change from VCSEL to VCSEL but taking "7-um Chalmers Gen 3 VCSEL Westbergh PTL 2013 (1.5 ps)" as example, it can be seen that there is a dip or a minima in the IMD3 profile at specific temperature and this dip shifts to the lower temperatures when increasing the bias current. This is most probably because of the de-tuning inside the active region where the gain profile and the longitudinal mode do not shift in wavelength in the same rate when changing the temperature. It seems that the longitudinal mode meets the maximum of the gain spectrum at these specific temperatures.

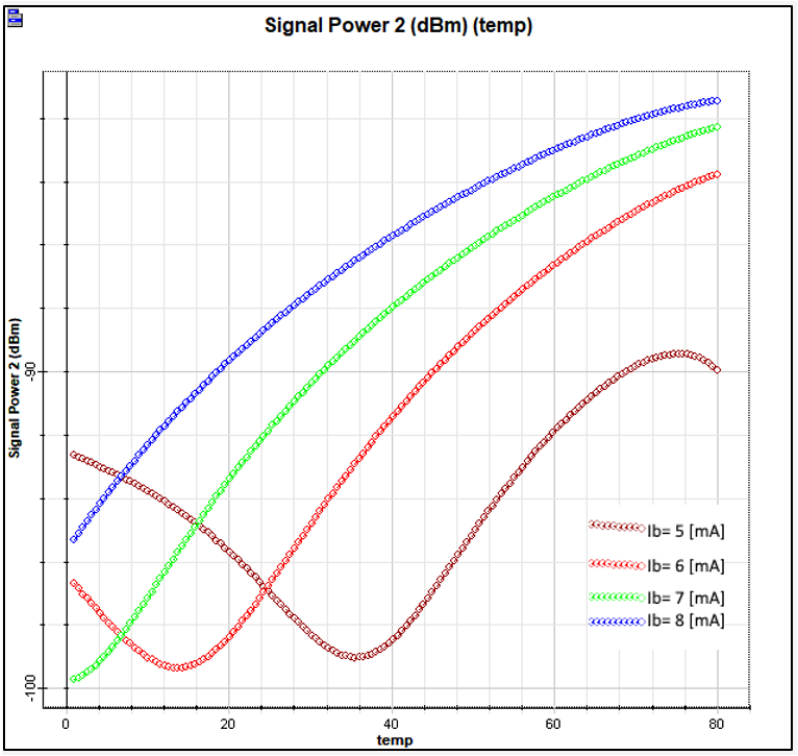

Figure 5.11: Simulated IMD3 as a function of temperature @ 2 [GHz] for the VCSEL: 7-um Chalmers Gen 3 VCSEL Westbergh PTL 2013 (1.5 ps)

5.2.5 Other sources of distortion

Nonlinearity sources (drivers) in the laser are: gain comparison, current leakage, relaxation oscillation and spatial hole burning. How much they contribute to the nonlinearity depends on dimensions, material, laser design, composition, modal behaviour. Here comes some of the most important nonlinearity drivers in VCSEL:

Gain compression: The gain in VCSELs is mostly depends on the carrier density and wavelength at thermal equilibrium as long as the carrier distribution in the conduction band and valence band. At high bias levels above threshold, gain distribution is inhomogeneous. This cause high power levels at one or a few discrete

wavelengths and then the stimulated emission will cause rapid recombination of the free carriers at particular energy levels in the bands. This will produce a disruption of the thermal equilibrium distributions.

Carrier heating: Carrier heating causes similar gain compression and this phenomenon occurs when the simulated recombination of carriers with energy below the quasi-Fermi levels. This will cause non-thermal distribution which is resolved by heating the remaining carriers. Adding extra term which is the gain compression factor ϵ to the gain expression will account for gain compression. $g = g_o/\left(1 + \varepsilon N_p\right)$ which accounts for the dependence of the photon density of the gain. Gain compression will cause an increment of the carrier density with power increasing. Increasing power will increase the internal loss and the spontaneous carrier recombination which in turn cause a distortion in the modulation response caused by gain compression.

Leakage current: Not all the injected current contribute to the output power. A portion of the injected current will leak across the active region or diffuse out of the active region. The leakage across the active region depends on the temperature, barrier heights in the QWs and separate confinement regions. These leaked currents are not linearly dependent on the injected current which cause a nonlinear current in the rate equation of the carrier density.

Spatial hole burning: The injected carrier density below the threshold has its maximum value at the centre of the active region. Stimulated emission starts to deplete the carrier density in the centre while the carrier density at the periphery continues to rise because it is not clamped by the stimulation emission. This will cause a hole in the carrier distribution profile in the centre and this phenomenon called spatial hole burning which will cause a dynamic change in the laser waveguide parameters. As a consequence, the lateral confinement of the main mode will decrease and increase the overlap with side-modes, which increase the number of the modes or mode-jumps. During the modulation, the depth of the hole varies which in turn will affect the dynamic response of the VCSEL. As discussed in the beginning of this chapter, the spatial hole burning dominates at low frequencies up to 2[GHz], after this frequency, the relaxation oscillations start to dominate.

5.3 Static characteristics and performance measures

The static characteristics of VCSEL are important when using VCSELs in Radio-over-Fiber links. The differential increment in output power (ΔP) with increasing the current (ΔI) is defined as the slope efficiency.

$$s_l = \frac{\Delta P}{\Delta I} \tag{5.1}$$

The slope efficiency is a measure of the electrical to optical power conversion efficiency as long as the VCSEL is modulated at frequencies far below the relaxation

oscillation. That is why it is desired to have very high slope efficiency in order to minimize the RF loss of the link. Increasing the internal quantum efficiency will increase the slope efficiency. Optical losses can come from free carrier absorption, absorption in the material outside the active region and from scattering [35]. Lowering the optical losses will increase the slope efficiency. Both internal quantum efficiency and optical losses are temperature, carrier concentration and dimensions dependent. This cause lowering in the slope efficiency for single mode devices.
The differential increase in voltage drop (ΔV) with an increase in drive current (ΔI) above the threshold is defined as the differential resistance:

$$r_d = \frac{\Delta V}{\Delta I} \tag{5.2}$$

r_d represents the series resistance in the device at the operating current. In VCSELs, the differential resistance comes from low electrical conductivity in the DBR mirrors due to the potential barriers. The temperature is increased at high differential resistance which in turn lowers the output power and the modulation bandwidth. This increment in differential resistance will create an impedance mismatch with the laser driver causing more RF loss at analogue modulation.
The ratio between the optical output power to the electrical input power is known as the wall-plug efficiency and it can be obtained by lowering the differential resistance and this will lower the power consumption as well.

$$\eta_{wp} = \frac{P_o}{P_{in}} = \frac{P_o}{IV} \tag{5.3}$$

The beam characteristics are very important factors in optical losses since they determine the efficiency of coupling the output beam with the optical fiber. High coupling efficiency can be obtained by having small beam divergence which depends on the dimensions of the waveguide, the number of the transverse modes and the strength of the optical waveguide in the VCSEL. As mentioned before, the number of transverse modes is the most important factor for the beam divergence since higher order modes produce more beams with more divergence than the fundamental mode. Single mode VCSELs provide the highest fiber coupling efficiency.

As has been seen, relaxation oscillation is the main reason of distortion around the resonance frequency. Two-tone modulation products can characterize the nonlinearity of the relaxation oscillation. Using two tone injection current and inject it in the single mode rate equations:

$$I(t) = I_0 + \left(i_1 e^{j\omega_1 t} + i_2 e^{j\omega_2 t}\right) \tag{5.4}$$

This gives the ratios of the second order harmonic (HD2) and the third order intermodulation products (IMD3) with respect to the fundamental frequency respectively.

$$\frac{HD2}{C} = m^2 \cdot |FR\,(2f_1)|^2 \cdot \left(\frac{f_1}{f_r}\right)^4 \tag{5.5}$$

$$\frac{IMD3}{C} = \frac{1}{4}m^4 \cdot |FR(f_1)|^2 \cdot |FR(2f_1)|^2 \tag{5.6}$$

$$\left[\left\{\left(\frac{f_1}{f_r}\right)^4 - \frac{f_1^2}{2f_r^2}\right\}^2 + \left(\frac{f_1}{f_r}\right)^2 \left\{\frac{1}{4\pi f_r \tau_n} - \left(\frac{f_1}{f_r}\right)^2 \left(2\pi f_r \tau_p + \frac{3}{4\pi f_r \tau_n} + \frac{3\varepsilon N_p}{2\pi f_r \tau_p}\right)\right\}^2\right] \tag{5.7}$$

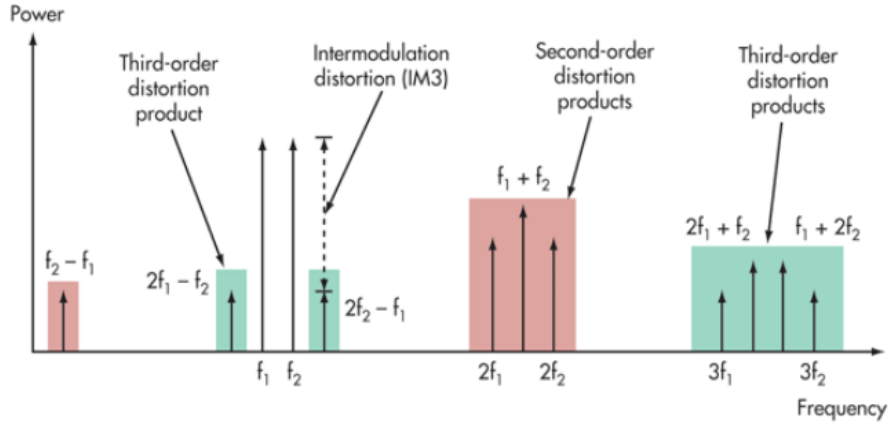

Figure 5.12: Illustration of the second (HD2), third order (HD3) harmonic distortion and the third order intermodulation distortion (IMD3)

where FR represents the small signal frequency response. ϵ accounts for the gain comparison coefficient, m is the optical modulation index and τ_n is the electron lifetime. Both second order harmonic (HD2) and the third order intermodulation products (IMD3) are proportional to m^2 and m^4 respectively. HD2 has its maximum value at the half of the resonance frequency due to FR$(2f_1)^2$ and that the IMD3 products exhibit a peak at resonance frequency and a sub-peak at the half of the resonance frequency [36].

5.4 Relive the effects of nonlinearity

Three workarounds have been proposed to alleviate the effect of nonlinearity.

The first one would be systematically by designing a VCSEL array consisting of different VCSELs where each VCSEL has different cutoff frequency than the other VCSELs, i.e. each VCSEL has different minimum distortion at different frequencies as has been seen in the HD2 distortion figures for three different VCSELs figure 5.13.

In this way, each OFDM signal would sent at the frequency where the minimum distortion frequency (distortion valley) located. Next step would be combine all the VCSELs output in a combiner and then inject the combiner output into the RoF system, figure 5.14.

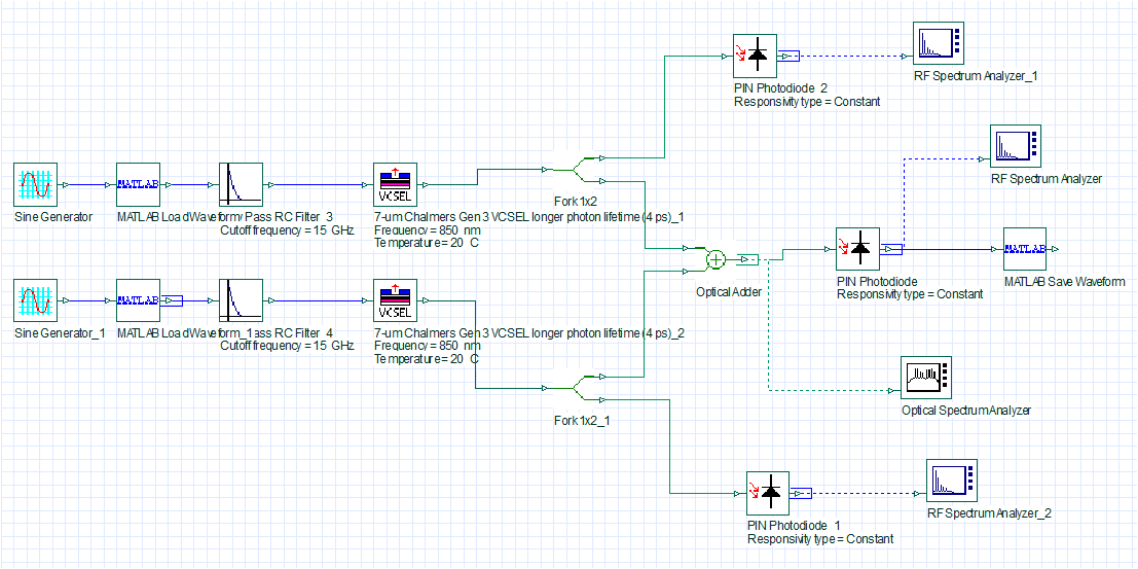

Figure 5.13: Combining two VCSELs output in a combiner before transmitting in the fiber

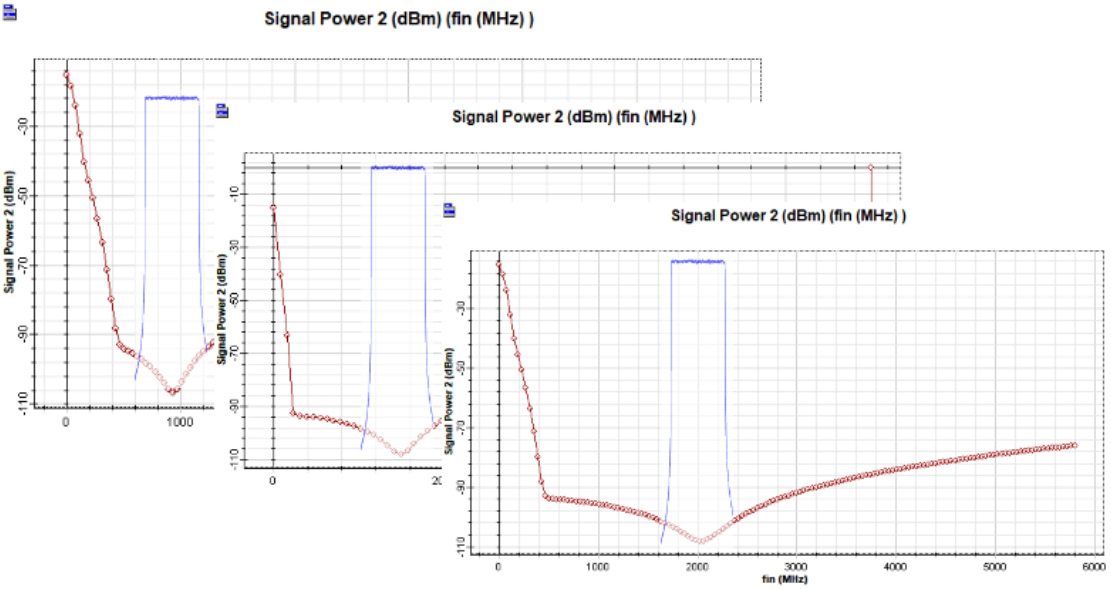

Figure 5.14: Illustration of sending three OFDM signals at the cutoff frequencies of three VCSELs

Another version of this workaround is inherited from WDM, an array of VCSEL lasers where each VCSEL has different wavelength than the other VCSELs in the array. Figure 5.15 shows the block diagram of this workaround. Two OFDM signals are sent into two different VCSELs where the wavelength difference is 0.05 [nm]. The output of the PIN photo-detector is the OFDM signals at 1.8 and 3 [GHz] respectively. the down-conversion of the cross-talk between these two wavelengths will have its maximum around 21[GHz] which equals to 0.05[nm]. This intermodulation can be filtered out using low pass filter which can pass only the frequencies desired of the OFDM signals. However, the wavelength separation is pretty small and it is

tricky to achieve. Increasing the separation will shift the optical intermodulation to much higher frequencies which is good where it will be much easier to filter it out.

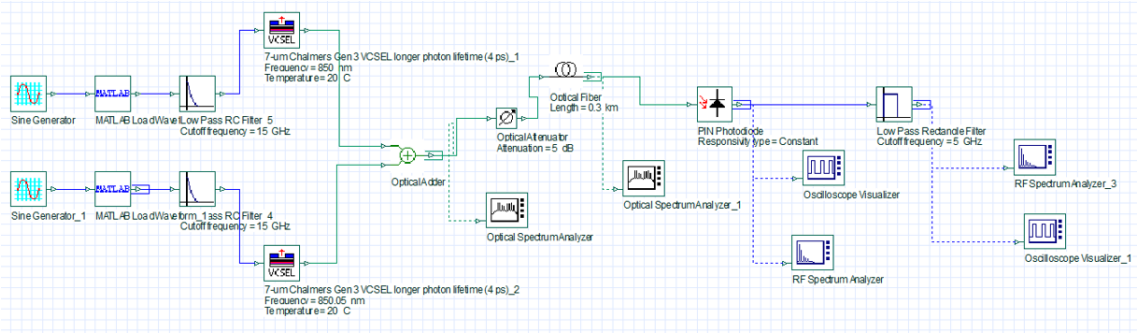

Figure 5.15: VCSEL array with different wavelengths

Figures 5.16 and 5.17 show the output of the PIN photo-detector and then the filtered OFDM signals.

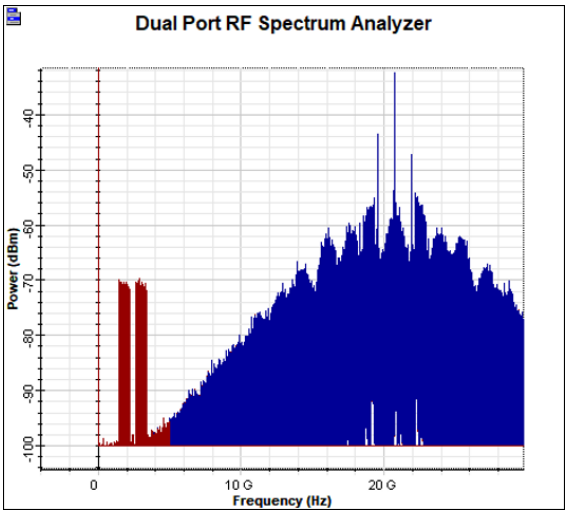

Figure 5.16: PIN photo-detector output wiht OFDM signals and the optical intermodulation distortion

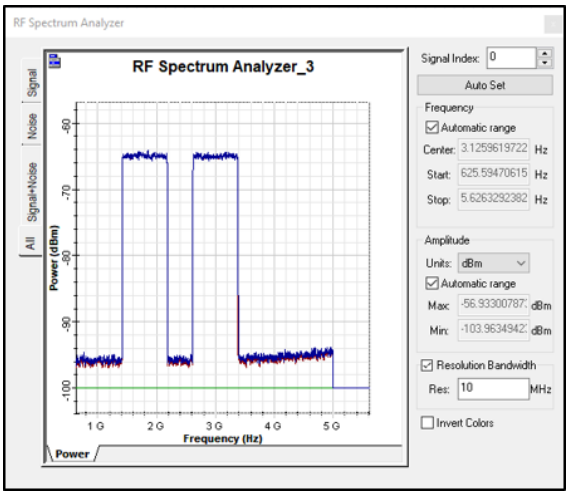

Figure 5.17: Filtered signal out of the PIN photo-detector output

The second workaround would be internally by having a better understanding of the drivers of nonlinearity which allow a better VCSEL design. It is always desired to have an relaxation oscillation frequency much higher than the modulation frequencies which in turn gives possibility to send multiple OFDM signals in the valley region between spatial hole burning and oscillation relaxation.

$$\omega_{RO} = \sqrt{\frac{\mu - 1}{\tau_P \tau_N}} \tag{5.8}$$

where μ is a pump current parameter which is proportional to I/I_{th}, τ_P and τ_N are

the photon lifetime and carriers lifetime respectively.

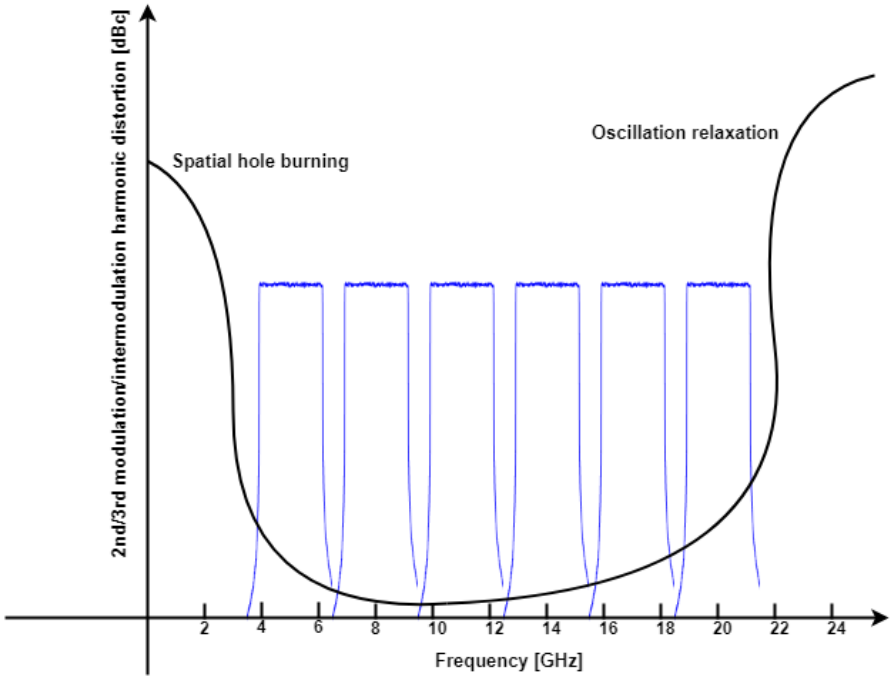

Figure 5.18: High relaxation oscillation frequency VCSEL

The third workaround would be externally using the selective optical feedback where it has been shown that sending Orthogonal Optical Feedback (OOF) back into the VCSEL will lower the second and third harmonic modulation distortions pretty much which in turn increase the modulation frequency and the VCSEL performance, this method will be discussed in more details next chapter.

6

Optical Feedback

6.1 Introduction

Usually, optical feedback associated with undesirable effects along the optical link. Every connection along the optical system introduces a small amount of the light back. It can come from fiber ends, micro-lenses in the fiber and due to some scattering process like Stimulated Brillouin Scattering (SBS). Very small amount of the reflected light can destabilize the laser. However, optical feedback has both advantageous and disadvantageous effects, under certain conditions, it can improve some features of laser, such as narrowing the linewidth, stabilize the Polarization Switching (PS) and suppress the nonlinearities associated to the polarization switching.

6.1.1 Effect of the optical feedback on the VCSEL parameters

The chaotic dynamics of VCSELs get big interest among researchers, especially in secure optical communications [40][41]. Chaos-based optical communications using laser polarization modes intensity gained a lot of interest as well due to encryption capabilities they have [42].

Some of the VCSEL major problems are polarization instability which sometimes known as polarization switching, hysteresis loop, low output power, and relative noise intensity. Polarization switching can occur due to different reasons such as changing the injection current, changing the temperature, optical feedback and an optical injection.

External optical feedback can be used to control instability with VCSELs which improves some VCSEL features such as reduction of threshold current which will reduce the losses inside the cavity as well as the intensity noise [44][45].

The relative intensity noise (RIN) characteristics of VCSEL are an important property in optical communications, it is aimed to have it low as much as possible. Fluctuations in photon density can be controlled by having optical feedback. RIN can significantly be reduced by using Optical Feedback (OF) from -124.8 to -149 dB/Hz [48].

Harmonic distortion can be suppressed using T-shaped polarization optical feed-

back. The power strength of harmonics peaks depends on the polarization direction that pumped back into the VCSEL. Using Orthogonal Optical Feedback (OOF), the second and third harmonics can dramatically be suppressed. RIN level as well depends on the PS position and modulation signal.

VCSEL structure is different from other semiconductor lasers such as distributed feedback laser. In VCSELs, light emitted perpendicularly to the surface of the laser. In VCSELs and due to the very thin active region, one longitudinal mode propagates from the laser and no need to suppress high-longitudinal side-modes.

VCSELs are very good candidate when it comes to Radio over Fiber since coupling efficiency with optical fibers is very high. On the other hand, VCSELs have some problems such as large frequency chirp and polarization instability which cause limitations in data rate speed and limited transmission distance [53].
VCSELs, as mentioned before, are very sensitive to the optical injection and optical feedback due to very short cavity length and high gain [43].

6.1.2 Light-current Curve Characteristics

VCSEL lases in a single polarization mode when operating near threshold current [54]. Due to the circular symmetrical structure, VCSEL can oscillate with orthogonal polarization simultaneously [55]. Polarization stability of VCSEL is essential and critical in most applications and data communications [56]. Light-current curve properties can tell the efficiency of the VCSEL [57] and it considered as one of the essential parameters of semiconductor lasers.

Most VCSELs emit linearity polarized light. However, polarization instability is a common drawback in VCSELs because of weak material and cavity anisotropies which means that polarization insensibility can occur even without external perturbations [37]. On the other hand, if the bias current is increased or external optical feedback is applied, the linearity polarization will change its state to the orthogonal linearity polarization, and this is due to changes in the loss and gain of the orthogonally polarized modes [58], changes in the temperature of the device and the magnitude and direction of the bias current [59].
The position of the PS mainly determined by three factors: The injection current, the electric field and the net gain of the two polarization modes [51].

6.1.3 VCSELs with Optical Feedback

As mentioned before, VCSELs are very sensitive to external optical feedback due to the short cavity and large emitting area they have [60]. Optical feedback usually used in VCSEL to control its polarization properties or enhance the dynamic characteristics of the VCSEL. Schematic setup of a VCSEL subjected to external optical feedback can be seen in figure 6.1 where external plane mirror that has high reflectivity is used to reflect part from the output beam back into the cavity of the laser. Mirror reflectivity and external cavity length are very important parameters

in the optical feedback mechanism. The dynamic characteristics of VCSELs, on the other hand, are dependent on the feedback strength, the external cavity length, and the mirror reflectivity.

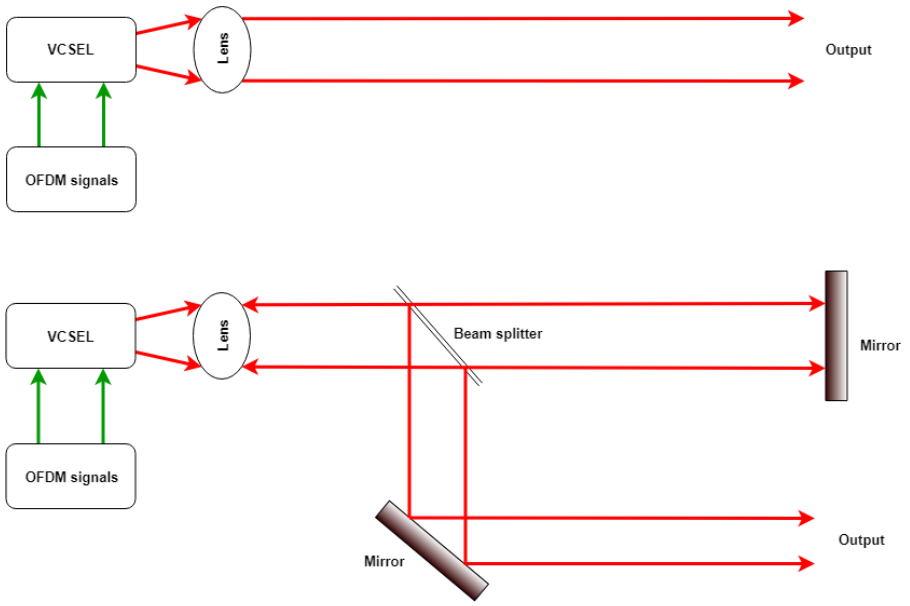

Figure 6.1: Optical feedback scheme for VCSEL.

Optical feedback can be divided into five regimes from weak (-80 dB) to high (-8 dB), figure 6.2:

Regime I, at weak level of optical feedback, the laser line emission can be narrowed or broadened depending on the phase of the reflected beam of optical feedback [62].

Regime II, where a split in the emitted beam is observed, and this is due to the longitudinal mode hopping which depends on the optical feedback strength and the distance of the reflector [63].

Regime III, at an approximately optical feedback level of -45 dB, the laser mode becomes very narrow and the mode hopping is suppressed dramatically.

Regime IV, at optical feedback of -40 dB, the laser linewidth broadens and the coherent distance reduces with increasing the optical feedback strength where the effects of this regime are independent of the phase of the feedback light, this regime sometimes is known as "coherence collapse" [64].

Regime V, a strong optical feedback level is needed to achieve stable operation of the external cavity mode. At very high optical feedback level, around -10 dB, an anti-reflection coating is necessary. In this regime, laser operates on a single longitudinal mode with very narrow linewidth and somehow insensitive of any additional external optical feedback perturbations.

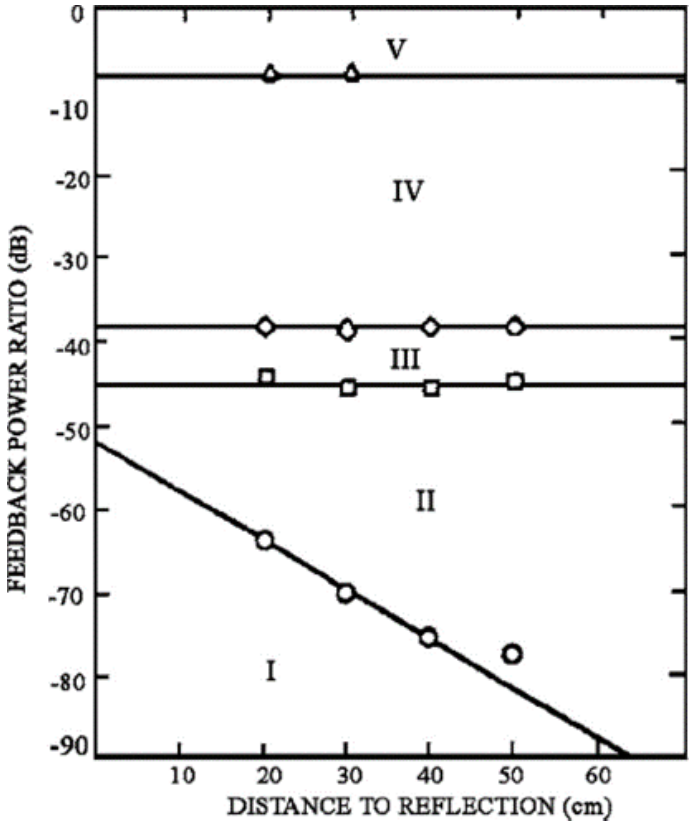

Figure 6.2: Tkach and Chraplyvy diagram, S. Donati, Laser and Photonics Rev. 2012

6.1.4 Relative Intensity Noise of VCSEL

Understanding the intensity noise characteristics is very important for many applications since intensity noise in the output power of lasers occurs due to fluctuations in photon density while carrier density variations result in a frequency noise [47]. The output power fluctuations are proportional to the Relative Intensity Noise (RIN). RIN can be considered as an important measure of the laser dynamics [67].

VCSEL based optical communications plays an important role in providing high-speed and short-range communication links. These features come from the fact that VCSEL has advantages over other types of semiconductor lasers such as small size, high speed, low power consumption, symmetrical circular output, low threshold current, and low-cost [39]. However, the noise level of VCSEL limits their performance in the optical fiber communication and thus causing limitations in the transmission distances and data rates [53][52].

RIN is an important factor to determine the achievable modulation bandwidth in the communication system, and it has been shown that the polarization mode inside the VCSEL plays an important role in defining the noise spectra. That is why it is important to understand and define the effects of RIN at every individual mode of VCSEL [68].

6.1.5 Nonlinearity of VCSEL

Nonlinear behavior of semiconductor lasers is of great interest in many application, especially in optical communication and Radio over Fiber communication since nonlinearity limits the RF dynamics of optical devices [69]. Nonlinearity in VCSELs considered as a major limiting factor in optical analog communications [70].
As discussed before, many physical mechanisms such as relaxation oscillation, spatial hole burning, current leakage, phase coupling, gain anisotropy and birefringence effects can cause a lot of nonlinearities in semiconductor lasers which in turn lead to decrease the power efficiency of VCSEL [50][72].

The nonlinear dynamics can be easily realized under the current modulation in VCSEL due to mode competition and polarization mode switching [74]. It has been shown that high nonlinearity in L-I curve can be noticed when the VCSEL is biased near the threshold current and it increases with increasing the modulation depth and modulating frequency which at the end cause different levels of harmonic distortion [71][73]. Another nonlinear behavior in L-I curve can be observed due to the nonlinear gain saturation of the lasing transition, this will increase the relaxation oscillation damping and reduce the intensity of the output power by reducing the differential gain [75].

6.1.6 VCSEL under Current Modulation

As discussed before, changing in bias current could cause polarization switching, and it has been shown that applying a small signal modulation does not induce a polarization switching, except for the frequency range of up to 100 kHz [76]. The situation is not the same for the large signal modulation, since, at certain frequencies, polarization switching may occur by changing the modulation amplitude. The laser favors the suppressed mode emission depending on the optical feedback and the drive current [65][66].

6.2 Theoretical Analysis of VCSEL

6.2.1 Rate Equations with polarization

We already have discussed the rate equations. However, it was for single mode laser without any referring to the polarization of these rate equations. We have to add the polarization terms to these equations in order to understand the influence of the type of polarization on the nonlinearity of the VCSEL. It would be easier to study the polarization and the optical feedback of the output optical light using the optical field rate equation model rather than Intensity (Photon) rate equation model.

6.2.2 Carrier and Photon Density Dynamics

Again, the most fundamental rate equations are those that describing the carrier development N and the photon development S as a function of time t. The carrier

generation rate $\eta_i I/qV$ should be equal to the carrier combination rate Gv_gS and the loss inside the cavity N/τ_c.

$$\frac{dN(t)}{dt} = \frac{\eta_i I}{qV} - \frac{N(t)}{\tau_c} - G(t)v_g S(t) \tag{6.1}$$

The second rate equation is the photon density, since the source of the photons are both the stimulated and spontaneous emissions. Losses of photons are taken into account by the photon lifetime term τ_p.

$$\frac{dS(t)}{dt} = G(t)v_g S(t) + \Gamma\beta_{sp}R_{sp} - \frac{s(t)}{\tau_p} \tag{6.2}$$

where η_i is the injection efficiency, I is the current density, V is the active volume, q is the unit charge, G is the gain coefficient, τ_c is the carrier lifetime, v_g is the group velocity, Γ is the confinement factor, β_{sp} is the spontaneous emission factor, and R_{sp} is the spontaneous recombination rate. The gain coefficient can be expressed by:

$$G(\mathrm{t}) = g_o \frac{N(\mathrm{t}) - N_\mathrm{o}}{1 + \epsilon S(\mathrm{t})} \tag{6.3}$$

And the gain coefficient assumed to be linear with respect to the carrier density. ϵ is the gain saturation coefficient, g_o is the linear gain coefficient and N_o is the carrier density at transparency. At the steady-state, the gain of laser will be equal to the threshold gain. Same thing for the carrier density, i.e. the carrier density should be equal to the carrier density threshold at the steady-state.

$$G = G_\mathrm{th}, \qquad (I > I_\mathrm{th}) \tag{6.4}$$

$$N = N_\mathrm{th}, \qquad (I > I_\mathrm{th}) \tag{6.5}$$

At the steady-state, the gain should equal to loss which means:

$$G_{th} = \frac{1}{\tau_p} \tag{6.6}$$

The average modal gain is equal to the threshold gain multiplied with the confinement factor:

$$< G >_{th} = \Gamma G_{th} =< a_i > + \frac{1}{L} \ln\left(\frac{1}{R}\right) \tag{6.7}$$

where R is the mirror reflectivity and L is the cavity length. The loss can be expressed by the photon lifetime as following:

$$\frac{1}{\tau_p} = v_g \left(< a_i > + a_m\right) \tag{6.8}$$

(a_i and a_m) are the total losses in the cavity, a_i is the internal losses or the photon losses and a_m is the mirror losses.

$$\Gamma G_{th} = \frac{1}{\tau_p v_g} =< a_i > + a_m \tag{6.9}$$

From the photon density rate equation, the photon density above the threshold can be expressed as:

$$S = \frac{\eta_i (I - I_{th})}{qVG_{th}v_g}, \qquad (I > I_{th}) \tag{6.10}$$

To get the optical output power, the optical energy should be calculated first which is defined in terms of the energy loss rate through the mirrors:

$$E_{in} = ShvV_c \tag{6.11}$$

$$P_{out} = ShvV_cv_ga_m \tag{6.12}$$

Using $\Gamma = V/V_c$ and substituting from eq.6.9 and eq.6.10 , the laser output power can be express as:

$$P_{out} = \eta_i \frac{a_m}{a_i + a_m} \frac{hv}{q} (I - I_{th}) \tag{6.13}$$

Defining the differential quantum efficiency:

$$\eta_d = \eta_i \frac{a_m}{a_i + a_m} \tag{6.14}$$

and substituting it in the output power equation 6.13 gives:

$$P_{\text{out}}(t) = \eta_d \frac{hv}{q} (I(t) - I_{th}) \tag{6.15}$$

The injected modulated current can be written as a sum of the bias current and the modulation current:

$$I(t) = I_{dc} + I_m(t) \tag{6.16}$$

The bias current I_{dc} is time independent and the $I_m(t)$ is time varying which can be expressed as:

$$I_m(t) = I_m e^{if_m t} \tag{6.17}$$

where f_m is the modulation frequency in Hz.

6.2.3 Basic Schemes of the Polarization Optical Feedback

The two main types of optical feedback are selective and preserver polarizations. For the preserve optical feedback, both the polarization components (XP & YP) re-injected into the VCSEL without any type of polarization selection. On the other hand, in the selective optical feedback, only one component (XP or XP) is selected and injected back into the VCSEL. A quarter-wave plate inserted into the external cavity to rotate the optical feedback polarization. The fast axis where the angle is (0°) defined as the XP optical feedback and the slow path where the angle is (45°) defined as the YP optical feedback.

The following figures 6.3, 6.4 show both setups of the optical feedback. In the first figure, the polarization preserve where the polarization of the reflected light is the reflected instantaneous copy of the original emission light. While in the second figure, the polarization selective optical feedback can be seen where the polarization beam splitter is used to split the both XP and YP into two orthogonal cavities which help to select only one polarization back.

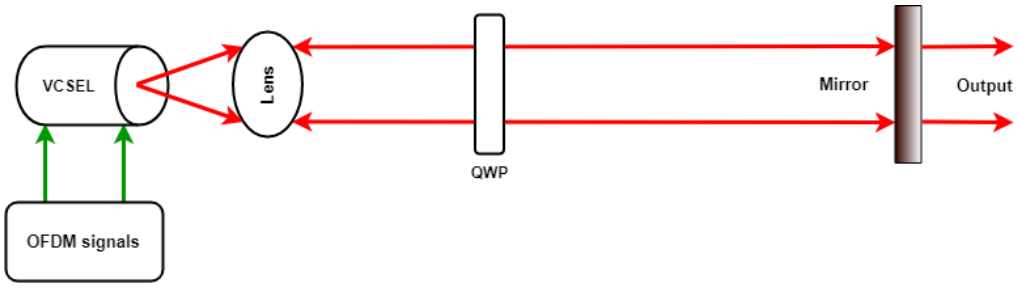

Figure 6.3: Principle scheme of preserve optical feedback

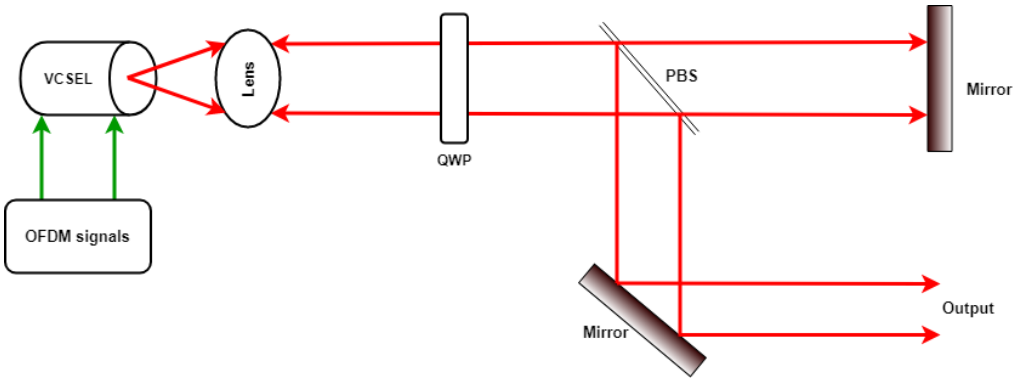

Figure 6.4: Principle scheme of selective polarization rotating optical feedback

6.2.4 The XP and YP Dynamics with VPOF

The usual behaviour of VCSEL is to emit a single polarization mode where the orthogonal mode is highly suppressed when lasing as a stand-alone laser without any external perturbation. The previous rate equations have to be modified in order to be able to describe the dynamical properties.

The optical feedback provided by using high reflectivity mirrors. A part of the light is rotated using quarter-wave plate (QWP) and re-injected back into the VCSEL. The time delay τ can be given by the cavity length L_{ext} and c, the speed of light in vacuum: $\tau = 2L_{ext}/C$.
The polarization angle equals to zero ($\theta_p = 0°$) corresponds to the pure XP feedback and ($\theta_p = 90°$) corresponds to pure YP feedback. Then the rate equations for both polarization modes take the form:

$$\frac{dE_x(t)}{dt} = \frac{1}{2}\left[G_x(t)\left(N(t) - N_o\right) - \gamma_x\right]E_x + k_x E_x(t-\tau)\cos\left(\theta_p\right) + \sqrt{\beta_{sp}\xi_x} \qquad (6.18)$$

$$\frac{dE_y(t)}{dt} = \frac{1}{2}\left[G_y(t)\left(N(t) - N_o\right) - \gamma_y\right]E_y + k_x E_x(t-\tau)\sin\left(\theta_p\right) + \sqrt{\beta_{sp}\xi_y} \tag{6.19}$$

$$\frac{d\phi_x(t)}{dt} = \frac{\alpha}{2}\left[G_x(t)\left(N(t) - N_o\right) - \gamma_x\right] - k_x\frac{E_x(t-\tau)}{E_x(t)}\cos\left(\theta_p\right) - \sqrt{\beta_{sp}\xi_x} \tag{6.20}$$

$$\frac{d\phi_y(t)}{dt} = \frac{\alpha}{2}\left[G_y(t)\left(N(t) - N_o\right) - \gamma_y\right] - k_x\frac{E_x(t-\tau)}{E_y(t)}\sin\left(\theta_p\right) - \sqrt{\beta_{sp}\xi_y} \tag{6.21}$$

The carrier density rate equation after taking into account the components for the optical feedback can be written as:

$$\frac{dN(t)}{dt} = \frac{\eta_i I}{qV} - \frac{N(t)}{\tau} - \left(N(t) - N_o\right) \times G_x(t)\left|E_x(t)\right|^2 + G_y(t)\left|E_y(t)\right|^2 \tag{6.22}$$

$$\Delta\phi(t) = -\Delta\omega_{x,y}t + \omega_{x,y}\tau + \phi_y(t) - \phi_x(t-\tau) \tag{6.23}$$

Here E_{x} and E_{y} are the varying amplitudes of the XP and YP modes respectively, k_x and k_y are the feedback strengths of XP and YP modes respectively, β_{sp} is the strength of the spontaneous emission, $\xi_{x,y}$ is independent Gaussian white noise sources with zero mean and unit variance for XP and YP modes, ϕ and ω are the phase and the angular frequency, respectively.

In a case of preserve optical feedback, both the polarization modes (XP and XY) are used to pass through the external cavity and then re-injected back into the VCSEL. Because of the rotation of the polarization angle, the feedback strength for the XP and YP modes can be written as:

$$k_x = k \times \sqrt{\frac{1 + \cos^2\left(\theta_p\right)}{2}} \tag{6.24}$$

$$k_y = k \times \sqrt{\frac{1 + \sin^2\left(\theta_p\right)}{2}} \tag{6.25}$$

Then the rate equations for the preserve optical feedback can be written as:

$$\frac{dE_x}{dt} = \frac{1}{2}\left[G_x\left(N(t) - N_o\right) - \gamma_x\right]E_x + k_x E_x\left(t-\tau_1\right)\cos\left(\theta_p\right) - k_y E_y\left(t-\tau_2\right)\sin\left(\theta_p\right) + \sqrt{\beta_{sp}\xi_x} \tag{6.26}$$

$$\frac{dE_y}{dt} = \frac{1}{2}\left[G_y\left(N(t) - N_o\right) - \gamma_y\right]E_y + k_x E_x\left(t-\tau_1\right)\sin\left(\theta_p\right) + k_y E_y\left(t-\tau_2\right)\cos\left(\theta_p\right) + \sqrt{\beta_{sp}\xi_y} \tag{6.27}$$

The feedback strength k can be calculated using the feedback ratio F in [61][78]:

$$k = \frac{1 - R_o}{\tau_{\text{in}}} \sqrt{\frac{R_m}{R_o}} \tag{6.28}$$

$\tau_{in} = 2L_{in}n_o/C$ is the internal round trip delay in second. n_o is the refractive index, L_{in} is internal cavity length. R_o is the facet reflectivity and R_m account for the external reflectivity and can be expressed as $R_m = 10^{\text{F}/10}$ (in dB) which is the feedback ratio.

6.3 Nonlinearity Behaviour and Relative Intensity Noise Investigation of VCSEL with VPOF

6.3.1 Introduction

In this section, the nonlinearity behavior of the polarization modes of VCSEL is studied. The dynamic behavior of semiconductor lasers is important to be understood and it received large attention in the research area. Nonlinearity is more important when the VCSEL is modulated and a modulated current injected into the VCSEL [73]. Some of the nonlinear properties that VCSEL exhibit due to direct modulation could be period-doubling, chaos and quadrupling [69][79].

In the application of the communication system when an analog signal sent directly into a VCSEL, the spectral properties of the laser are important characteristics. Variation in temperature can cause additional irregular behavior in the spectral distribution of the VCSEL which affect dramatically the laser dynamics [80].

To improve the linear dynamic of VCSEL, a method based on selective optical feedback could be used. The orthogonal optical feedback can suppress the nonlinearity associated with the type of polarization mode of VCSEL. The injected current and the temperature affect the nonlinearity of the VCSEL, and it has been shown that the nonlinearity behavior increased by increasing the temperature.

On the other hand, the relative intensity noise (RIN) is an important factor to determine the maximum achievable modulation bandwidth in the system. The RIN does not affect the polarization mode in the same way, that is why it is important to understand the effects of RIN on the polarization modes individually.

6.3.2 Frequency Response of VCSEL with OF

In figure 6.5, the frequency response of the polarization modes of VCSEL is plotted. The frequency response of the XP mode with OOF shows that the 3-dB modulation bandwidth is enhanced. The modulation bandwidth of the frequency response of the YP mode with OOF is enhanced as well.

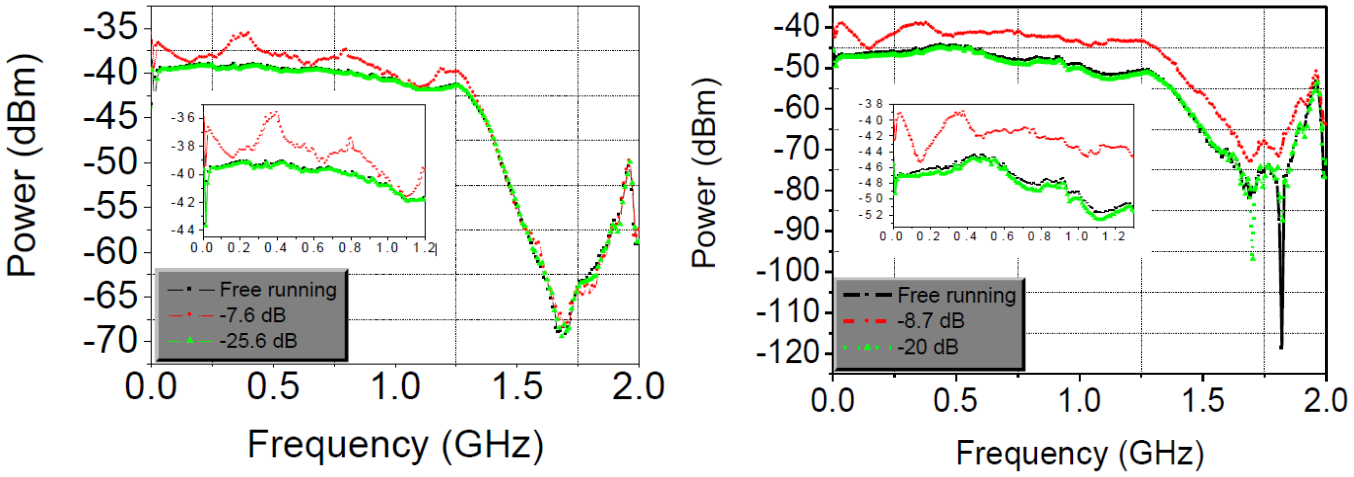

(a) XP mode **(b)** YP mode

Figure 6.5: (a) frequency response of the XP mode,(b)YP mode at free running VCSEL (soled black), -8.7 dB OF (dashed red) and -20 dB (dashed green) with bias current of 3.6 mA. The inset figure displays enlarge scale until frequency of ∼1.2 GHz [37].

6.3.3 Temperature Effects on the Linearity of VCSEL

As discussed before, the temperature can cause further nonlinearities in the semiconductor lasers [73]. Changing the bias current as well will lead to further nonlinearity. In figure 6.6, different values of the bias current I_b and the temperature have been considered. Three values of the I_b are taken into account, 3, 3.6 and 5.6 [mA]. The second and third harmonics are almost constant in a temperature range of 5° to 20°. In case of $I_b = 3$ or 3.6 $[mA]$, increasing the temperature will increase (decrease) the second (third) harmonic which causes to increase HD of the XP mode. In the case of $I_b = 5.6$ $[mA]$, both the second and third harmonics increases with temperature.

6.3.4 Relative Intensity Noise Characteristics

The simulation setup for the RIN measurements can be seen in figure 6.7. A beam splitter is used to split the VCSEL output beam into two paths, one path directed to mirror in order to reflect the light into the VCSEL back. The QWP is used to rotate the XP and YP modes before re-injecting them back into the VCSEL. To be able to rotate the polarization, the QWP was used, the rotating angle starts from 0° to 90°. To control the strength of the optical feedback, a Neutral Density Filter (NDF) is placed between the mirror and the QWP.

An HWP and the PBS are used to adjust the two orthogonally polarized modes where the dominant mode is the XP and the suppressed mode is the YP mode. The PBS will split the two polarizations into two identical photodetectors.
As seen in a previous chapter, there is no polarization switching on the L-I curve of the free-running VCSEL. The consideration was particularly given to rotate the

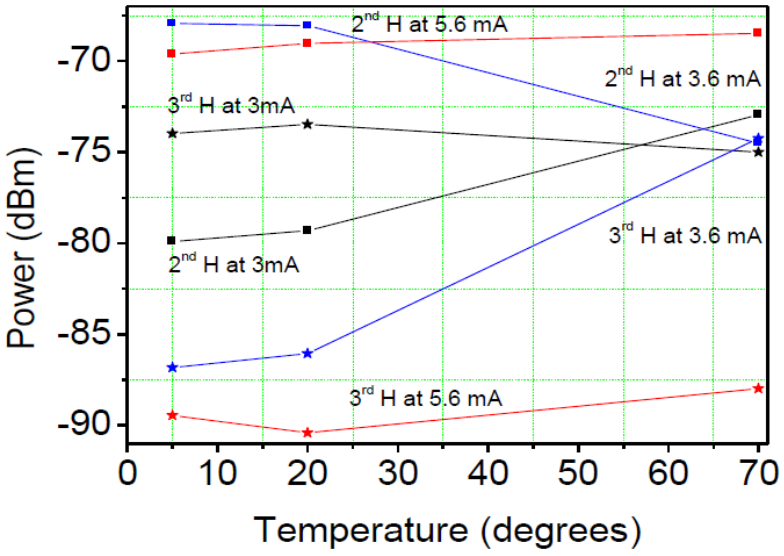

Figure 6.6: the electrical power spectrum as a function of temperature of the 2nd (square) and 3rd (star) harmonic of the dominant mode (XP) at the modulation frequency of 1 MHz and modulation depth of 68% without optical feedback and depending on bias current. The black, blue and red lines indicate to 3 mA, 3.6 mA and 5.6 mA, respectively [37]

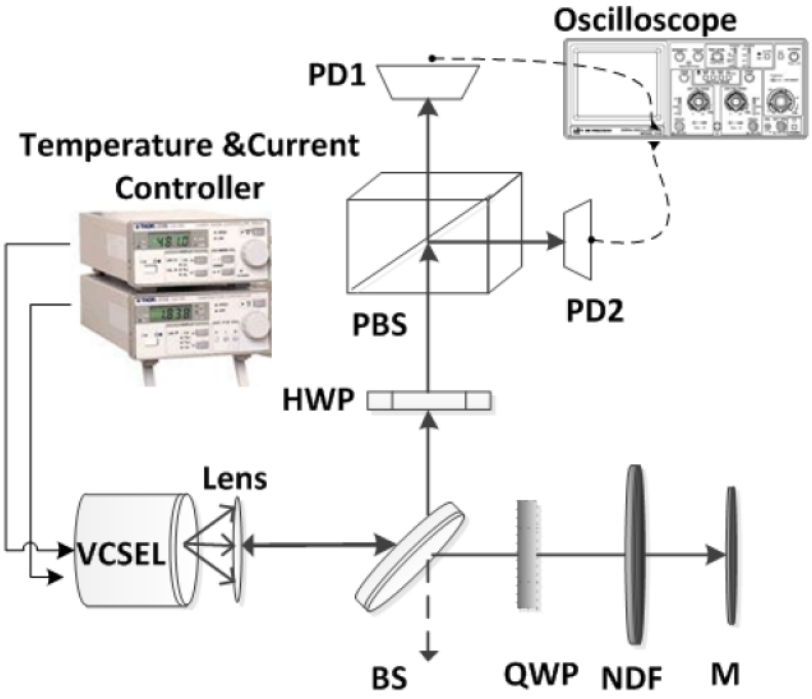

Figure 6.7: Experimental setup to measure RIN of VCSEL polarization modes subjected to VPOF; BS: beam splitter. QWP: quarter wave plate. NDF: neutral density filter. M: mirror. HWP: half wave plate. PBS: polarized beam splitter. PD: photo-detector [37]

θ_p with preserving the polarization and their influences on the polarization-resolved RIN of the VCSEL. Both the bias current and the strength of the optical feedback were fixed because only XP mode has to be emitted. The Relative Intensity Noise (RIN) is defined as:

$$RIN = \frac{\overline{\left(P_o(t) - \overline{P_o(t)}\right)^2}}{\overline{P_o(t)^2}} \tag{6.29}$$

where the $\overline{P_o(t)}$ is the average output power and $P_o(t)$ is the output power of the VCSEL. The RIN is been averaged along the whole considered frequency range. At $\theta_p = 0°$, the polarization-resolved RIN when the VCSEL subjected to strong optical feedback can be shown on figure 6.8, the dominant mode is the XP mode and the YP mode is the suppressed one. At this polarization angle, the RIN of the XP mode is far below the RIN of the YP mode, this means that the two polarization modes are well separated at this angle.

Since the XP mode is the dominant one, the XP mode gain is higher than that of the YP mode. The RIN of the XP mode still lower than that of the YP mode for $\theta_p = 0 \sim 45°$ since in this range, the XP mode still has more optical feedback than the YP mode [49]. After the polarization angle exceeding $\theta_p > 45°$, the RIN of the YP mode starts to be lower than that of the XP mode and YP becomes the dominant mode and this is because of the gain switching that occurs as a result of polarization switching between the orthogonal modes for $\theta_p > 45°$. At polarization angle between 75° to 90°, no changes in the RIN occur of the two modes, and RIN value remains constant for higher values of θ_p. The behavior of the RIN of the XP mode is increasing along the whole $\theta_p = 0°$ to 90° range, while the RIN of the YP mode increases until $\theta_p = 45°$, and then it starts to decrease.

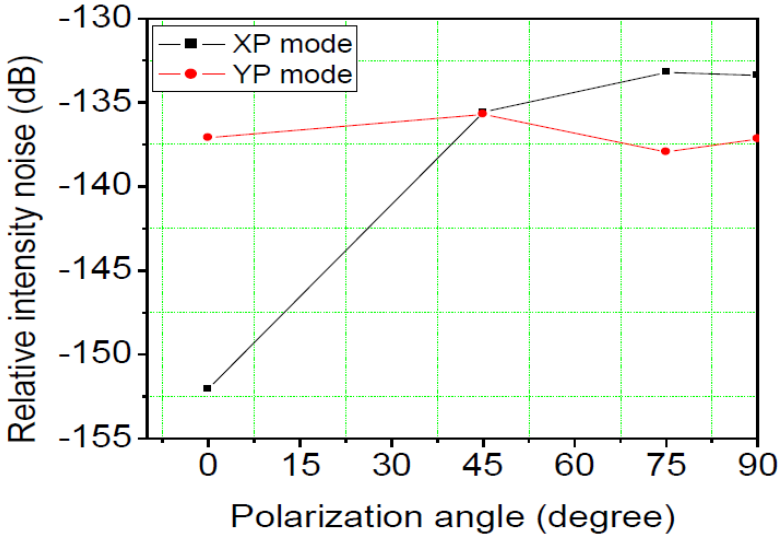

Figure 6.8: Polarization-resolved RIN as a function of polarization angle for XP and YP modes, with the VCSEL subject to -5.5 dB optical feedback level [37]

Figure 6.9 shows the polarization mode intensities as a function of the time. It can be shown that at $\theta_p = 0°$, the XP mode has a higher intensity than the YP mode because the XP is the dominant mode and it has higher gain at this angle. Both modes are widely spaced comparing with other angles ($45°, 75°,$ and $90°$). At $\theta_p = 45°$, both XP and YP modes have almost the same intensity since the XP mode loses progressively the feedback light along with increasing the θ_p and YP mode gaining more feedback [49].

Figures show as well that YP (XP) mode intensity increase (decrease) along with increasing the polarization angle θ_p.

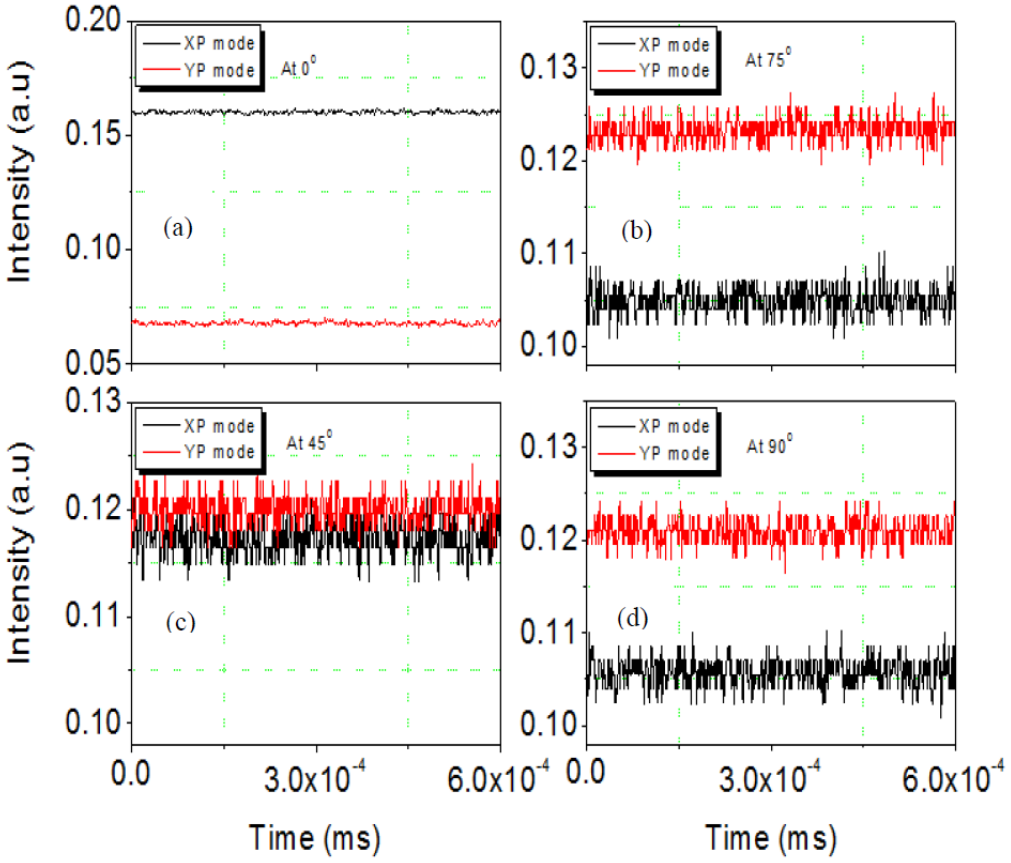

Figure 6.9: Intensity profile of the XP (black) and YP (red) polarization modes of VCSEL with a feedback strength of -5.5 dB, for θ_p of (a) 0°, (b) 45°, (c) 75° and (d) 90°.

As discussed before and due to the polarization switching effect, the RIN of the XP mode become higher than the RIN of the YP mode at $\theta_p > 45°$. The RIN of the XP mode is minimum at $\theta_p = 0°$ while it is a minimum at 90° for the suppressed polarization mode YP. On the other hand, increasing the polarization angle will increase the number of the spectral lines that appear in the spectrum profile.

6.3.5 Suppressing the Nonlinearity of Free Running VCSEL using Selective-Optical Feedback

In this section, the parallel and orthogonal optical feedback employed into a standalone VCSEL with a variable range of optical feedback and different values of the bias current I_b. This will allow to investigate the nonlinearity of the XP and YP modes. It has been shown that the parallel optical feedback will increase the harmonic distortion of the parallel mode of the VCSEL. These products are almost entirely suppressed by using the orthogonal optical feedback [37].

6.3.5.1 Simulation Arrangement and Discussion

Here, a simulated setup is studied where an investigation of the effects of the selective optical feedback on the VCSEL properties has been done. As shown in the following graph, A 850 [nm] VCSEL used in this simulation. This VCSEL has a linear output power over a range of the bias current I_b. VCSEL parameters can be shown in table 6.1.

Parameter name	Value
$k_{x,y}$ (Polarization feedback coefficient)	Variable
β_{sp} (Strength of the spontaneous emission)	10^{-5} ns^{-1}
$\gamma_{x,y}$ (Inverse of photon lifetime for XP & YP mode)	7.692×10^{-11} s^{-1}
τ_x (Feedback delay for XP mode)	6.4 ns
τ_y (Feedback delay for YP mode)	2.6 ns
G_0 (Difference between XP and YP gain coefficients)	5×10^{-13} m^3/s
G_y (Gain coefficient for YP mode)	2×10^{-12} m^3/s
N_0 (Carrier density at transparency)	2.5×10^{24} m^{-3}
$1/\tau$ (Inverse of carrier life time)	1×10^9 ns^{-1}
λ (Wavelength of laser)	850 nm
Δf (Frequency detuning of XP and YP modes)	40 GHz
R_0 (The mirror reflectivity)	0.995
n_0 (The reflective index)	3.5
R_m (The external reflectivity)	$10^{F/10}$
L (Laser cavity length)	2 μm
α (Line-width enhancement factor)	3.0

Table 6.1: Parameter values for VCSEL under study

A modulated current is injected into the VCSEL. To study the third-order intermodulation (IMD3), two sinusoidal signals are injected into the same VCSEL after combining them in one route.

A 50/50 beam splitter is used to split the output beam into two parts. The first part is directed to an optical receiver after passing through a linear polarizer which is used to select the polarization direction of the polarization modes. The second part is directed to a T-shaped external cavity. The light passes a zero-order Half-Wave Plate (HWP), then a Polarization Beam Splitter cube (PBS) is used to direct the orthogonal polarization modes into two orthogonal mirrors M1 and M2 which reflect the light parallelly and orthogonally. The strength of the feedback level can be adjusted using a Neutral Density Filter (NDF). The parallel mirror M1 and orthogonal mirror M2 are used for POF and OOF for the XP and YP mode respectively. The setup of the simulation can be seen in figure 6.10 [37].

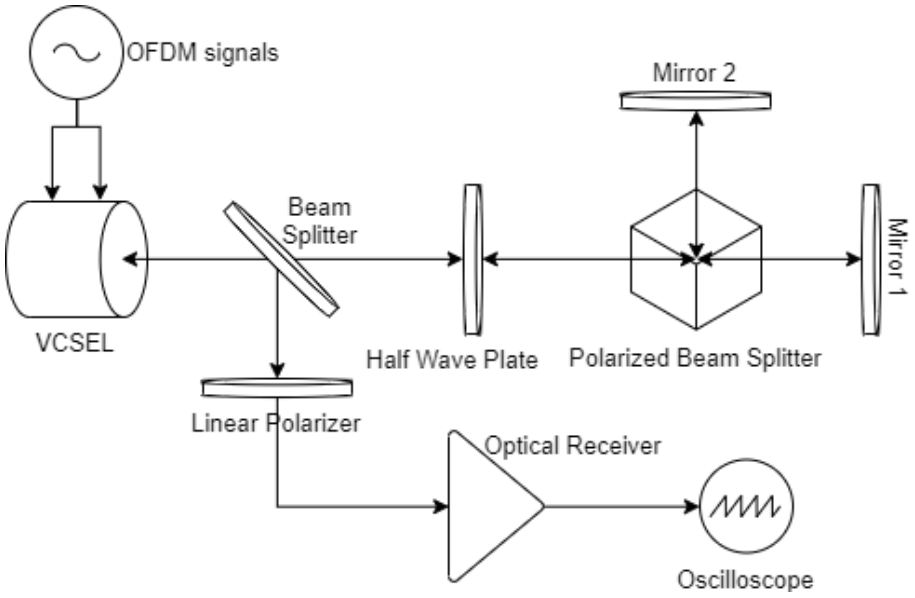

Figure 6.10: Simulation setup to measure power spectrum of the VCSEL with OF

The setup from OptiSystem simulation software can be seen in figure 6.11. It is basically the same as figure 6.10. It started by injecting a sinusoidal signal in the VCSEL, The VCSEL output is split using a power splitter where one of the splitter output goes directly to the photodetector. The second output injected into another power splitter. One output injected into polarization waveplate and then into the polarization splitter. polarization splitter split the polarization into two polarizations, each one injected into mirror, polarization delay and attenuator to block one of these polarizations along with testing different optical feedback polarizations. The reflected signals combined again using polarization combiner which in turn reinjected into a polarization waveplate and its output combined again with the other arm of the second power splitter. The output injected into a linear polarizer and then convert again into electrical signal using photodetector.

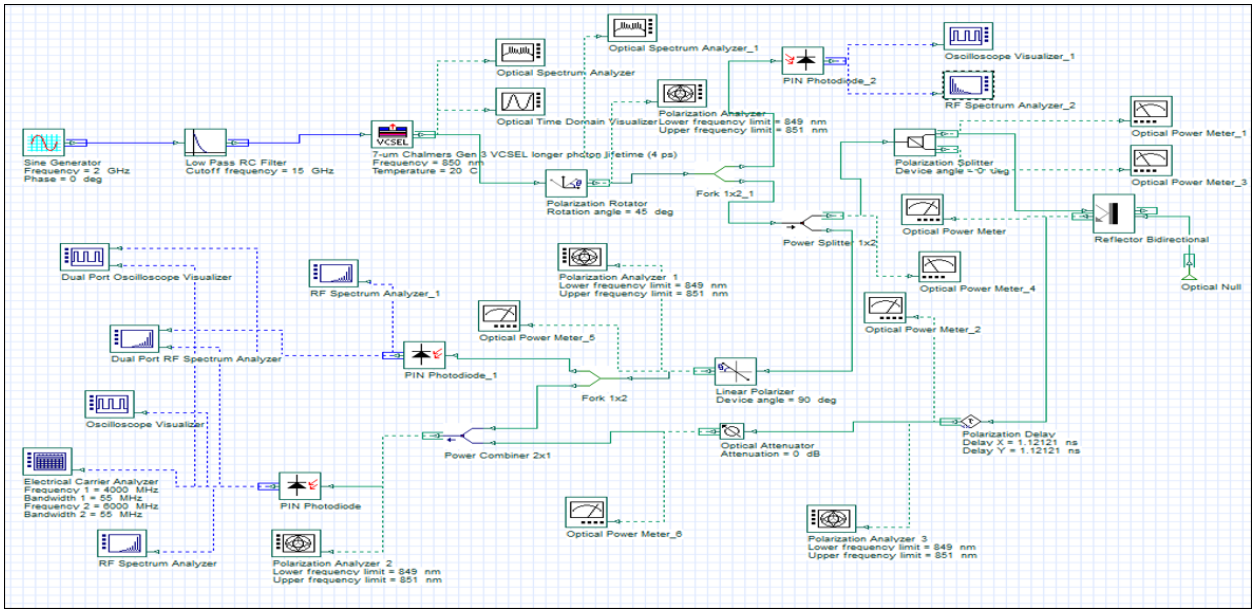

Figure 6.11: Simulation setup in OptiSystem

A stand-alone VCSEL emits two orthogonal polarization modes where XP mode has higher emission strength compared with YP mode emission over the entire range of I_b. In figure 6.12, the polarization-resolved L-I characteristics of VCSEL can be seen.
From the polarization-resolved figure 6.12, the VCSEL starts lasing with XP mode, which is dominant over the whole range of the bias current. YP on the other hand starts lasing after fraction of mA. Increasing the bias current will increase both modes equally, but YP mode will have lower power emission.

6.3.5.2 Harmonics Distortion of VCSEL under Selective-Optical Feedback

XP and YP modes nonlinearities can be characterized by studying the output power spectra and the harmonics power under the polarization-selective optical feedback. In figures 6.13, free-running VCSEL, XP and YP modes spectra are presented. The fundamental harmonic and the 2^{nd} harmonic are clearly distinguished with different peaks power level for both XP and YP modes. As has been discussed before, the harmonic distortion (HD) comes mainly from the nonlinearity characteristics of the L-I curve of the VCSEL. The special hole burning also contributes to the output power intensity profile of the VCSEL [72][77][81]. The high order nonlinearities for the XP mode measurements are dominant when the POF feedback is applied. the HD increases compared to the free-running VCSEL.

On the other hand, when the OOF is applied, the 2^{nd} harmonic is almost entirely suppressed and the HD get reduced compared with that of the free-running case. In the same fashion, the nonlinear behavior is dominant in the YP mode measurements when the POF is applied where the 2^{nd} harmonic is enhanced, when OOF is applied,

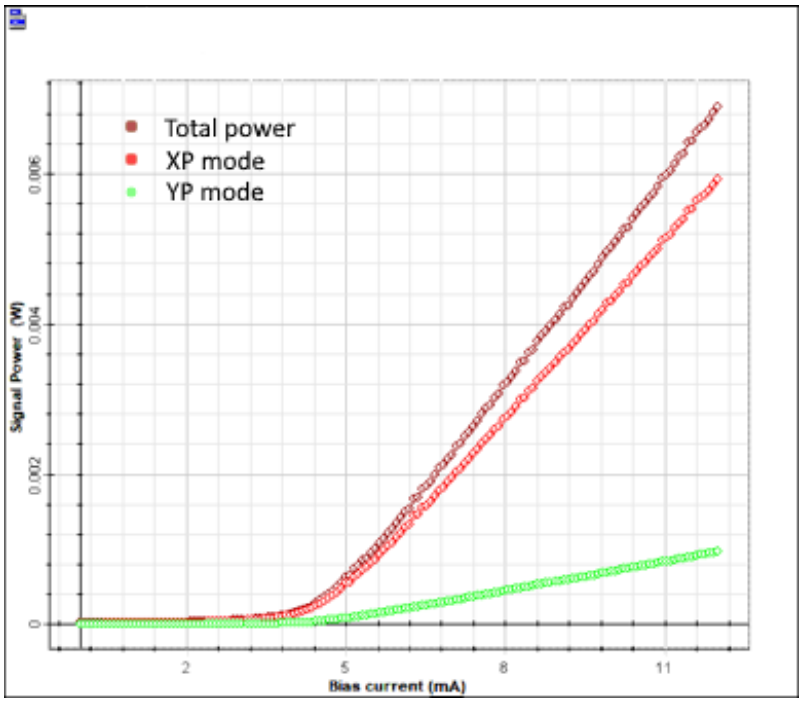

Figure 6.12: Polarization-resolved L-I curve of the standalone VCSEL. Square black and dot red lines correspond to XP and YP mode respectively. The triangle green line refers to the total output power

the 2nd harmonic power is almost entirely suppressed and HD is reduced compared to that of the free-running operation.

By utilizing the orthogonal optical feedback, the dynamic range of the VCSEL is improved and the modulation bandwidth is increased. As shown in figures 6.13, the harmonic distortion strongly depends on the polarization direction of the optical feedback, since the parallel optical feedback cause increase in the power of harmonics of the similar polarization mode of the VCSEL. On the other hand, the orthogonal optical feedback causes dramatic suppression of harmonics of the orthogonal mode of the VCSEL which in turn resulting reduction of nonlinearity characteristics in the output power of the laser mode.

The most two main optical feedback control parameters are the feedback strength and the feedback delay time. Figure 6.14 illustrate the second-order harmonic distortion with respect to the length of the external cavity. The length is counted for using a delay block. It can be seen a periodic behavior depending on the length, at specific lengths, the HD2 get its maximum and it repeat it self periodically. Same thing for the minima where HD2 has its minimum values at these lengths.
Figure 6.15 shows the second-order harmonic distortion with respect to the feedback strength. As can be seen, increasing the feedback strength will decrease the HD2. However, with high feedback strength, it required to have anti-reflection at the upper DBR of the VCSEL where the system ends to be as tow cavities, long and short, where the active cavity is the VCSEL.

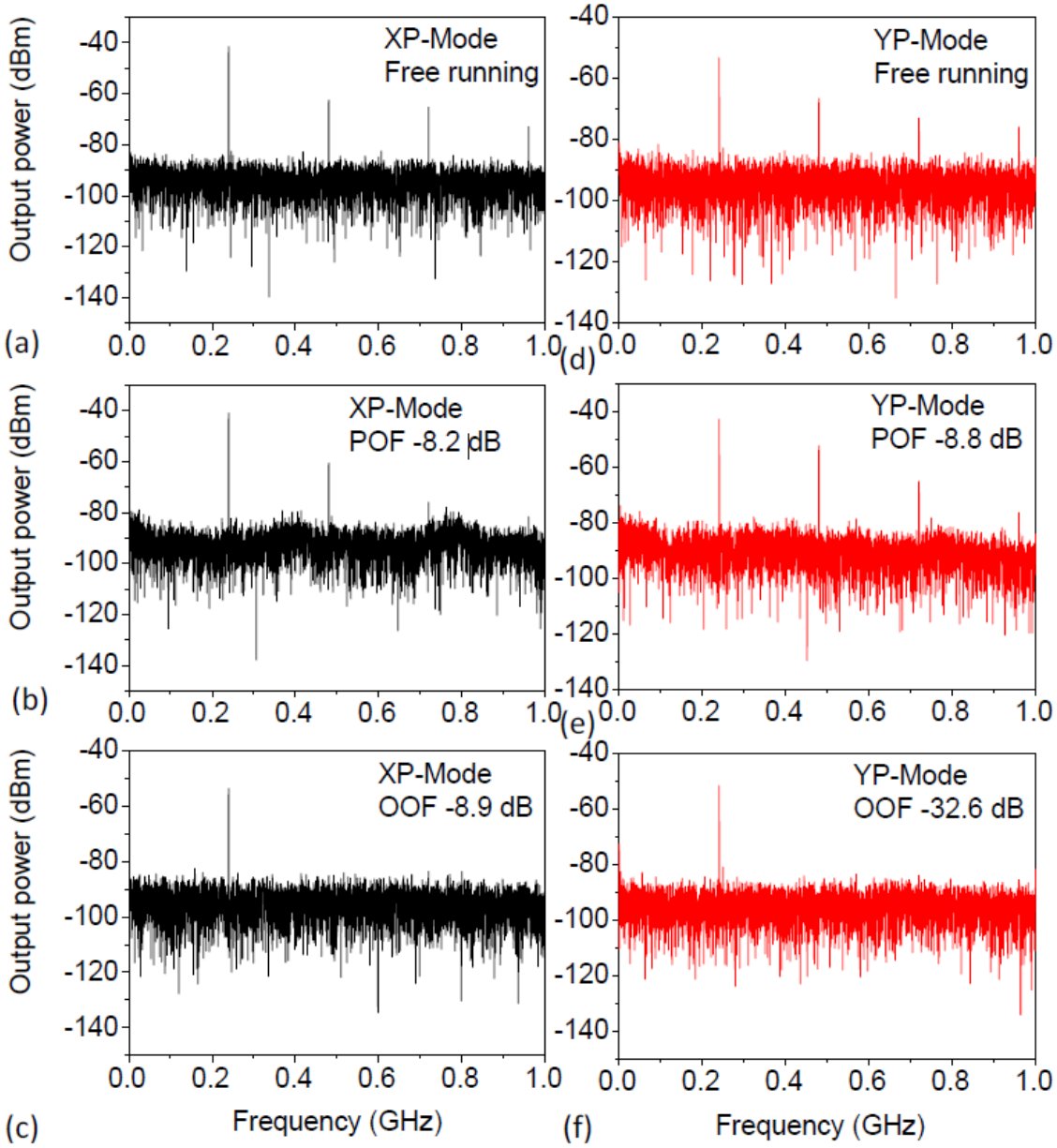

Figure 6.13: Left, the frequency spectrum of the XP mode of VCSEL for: (a) free running, (b) POF of -8.2 dB, and (c) OOF of -8.9 dB. Right, the frequency spectrum of the YP mode of VCSEL for: (d) free running, (e) POF of -8.8 dB, and (f) OOF of -32.6 dB at a bias current of 3.6 mA[37].

To get best result and lowest HD2, lowest dip in figure 6.14 and relativity good value for feedback strength -6 [dBm] could be chose. Setting these values in the simulation along with OOF give results that agree well with the experimental results.

POF will increase the strength of the harmonics and even create new harmonics. However, OOF results to totally suppress HD2 and HD3 as can be seen in figures 6.16 and 6.17.

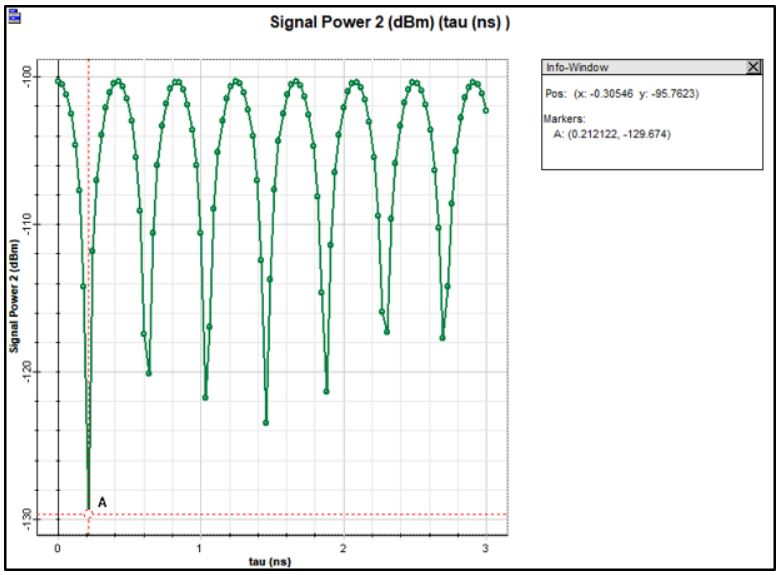

Figure 6.14: HD2 vs external length of the cavity

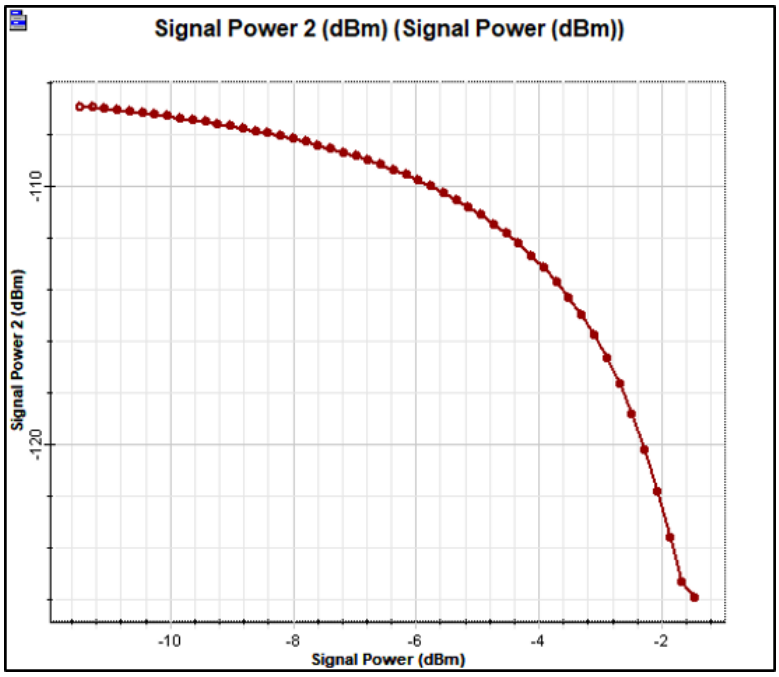

Figure 6.15: HD2 with respect to the optical feedback strength

In [37], an experimental setup and arrangement have been done and it found that for XP mode for the free-running VCSEL case, the 2nd, 3rd and 4th harmonics are ∼21, ∼24 and ∼32 dB respectively. The case of parallel optical feedback (POF) with strength of -8.2 db, the 2nd, 3rd and 4th harmonics increased by ∼2, ∼11 and ∼9 dB respectively. The third case is orthogonal optical feedback (OOF) with strength of -8.9 dB, the harmonics get reduced to the noise floor of -100 dBm.

The red graphs in figure 6.13 illustrate the harmonic spectra of the YP mode. At the free-running VCSEL case, the 2nd, 3rd and 4th harmonics are ∼14, ∼20 and ∼23 dB

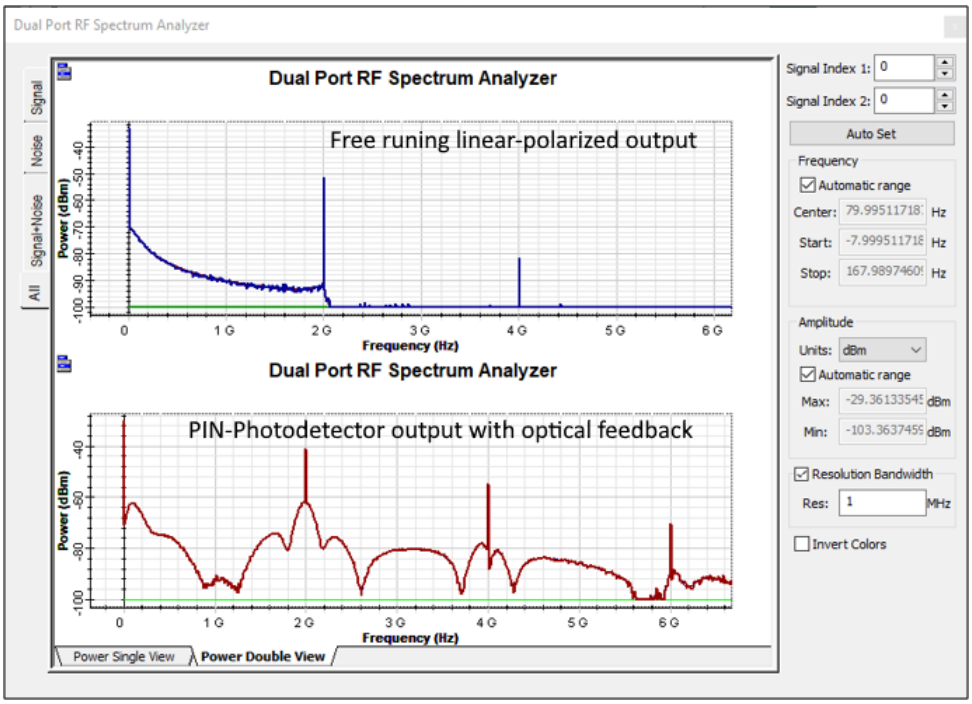

Figure 6.16: Comparison between the free-running to POF output spectrum

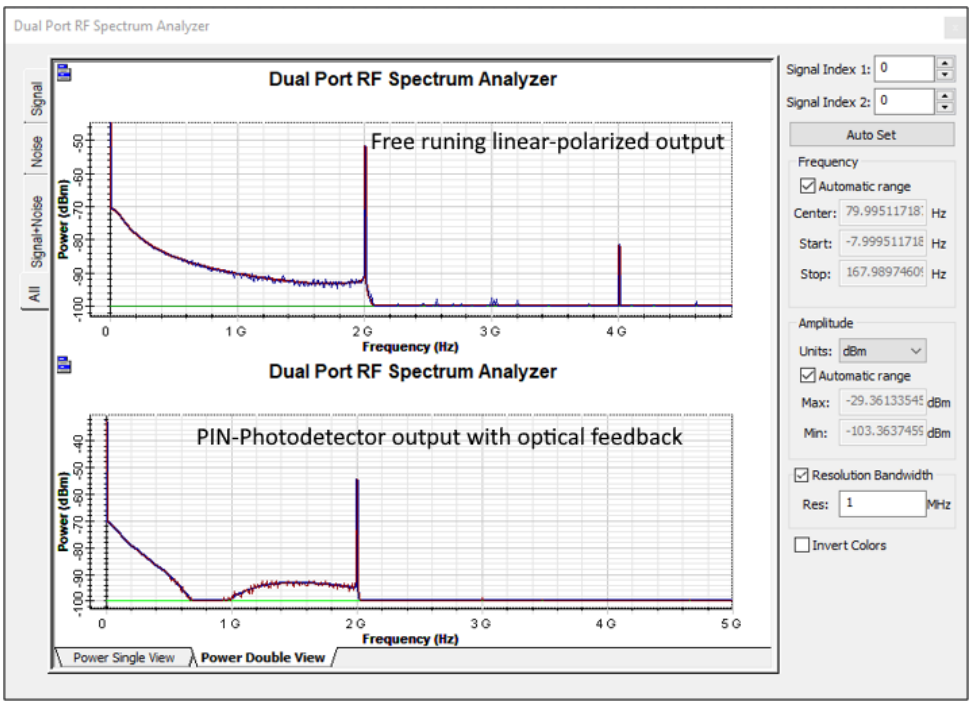

Figure 6.17: Comparison between the free-running to OOF output spectrum

respectively. The case of parallel optical feedback (POF) with strength of -8.8 db, the 2nd, 3rd and 4th harmonics ∼10, ∼23 and ∼40 dB respectively. The nonlinearity increased compared to the free-running case. In the same fashion of XP mode, the third case is when orthogonal optical feedback (OOF) is applied, the harmonics get reduced to the noise floor of -100 dBm.

7

Conclusion and further work

In this thesis, a theoretical study has been done to analyse the behaviour of sending multiple OFDM signals in the same Radio over Fiber system. The study started by understanding how OFDM works and introducing FB-OFDM. Then a study of a Radio over Fiber system, which benefits it can provide and the need of centralizing the signal processing and complexity in the core station and make the base station and antenna unit as simple as possible.

It has been shown that transmitting multiple OFDM signal in a Radio-over-Fiber system will create unwanted harmonics which appear mostly at second, third harmonic and at the third order intermodulation harmonic. The analysis goes further to understand where this nonlinearity comes from. Starting by excluding the nonlinearity comes from the optical fiber since the injected power was too low so no harmonics should generated in the fiber due to nonlinearity drivers in the fiber optic: (SPM),(CPM),(FWM),(SRS) and (SBS).

A theoretical study about how the semiconductor lasers work is done which lead to introduce the vertical-cavity surface-emitting laser (VCSEL) and the benefits the VCSEL can provide. The VCSEL however cause a lot of nonlinearity due to many reasons such as Relaxation oscillation, Spatial hole burning, Gain suppression, Leakage currents, Carrier heating. The major contributions to distortion in VCSELs are the second harmonic distortion (HD2) and the third intermodulation harmonic distortion (IMD3).

Three workarounds have been proposed to alleviates the effect of nonlinearity on the coexistence of multiple signals in the same RoF system. Understanding of the drivers of non-linearity allow a better VCSEL design which could be VCSELs with oscillation frequency much higher than the modulation frequencies. This will allow sending multiple OFDM signals in the valley region between spatial hole burning and oscillation relaxation.

The second one is to design a VCSEL array where each VCSEL has different cut-off frequency than the other VCSELs. i.e. each VCSEL has different minimum distortion at different frequencies. Sending each OFDM signal in each minimum distortion frequency (distortion valley) and then combine all VCSELs output together in one fiber link will protect the input signals from distortion comes from nonlinearity drivers.

The third one is the selective optical feedback where it was shown that sending OOF back into the VCSEL will lower the second and third intermodulation distortions pretty which increases the modulation frequency and the VCSEL performance.

7.1 Further work

Further work could be more understanding about how the optical feedback affects the polarization of the VCSEL and thus more control over the nonlinearity. Implementing an optical feedback system along with optical receiver would give more degree of freedom to control the VCSEL properties and get better quality of output signal of the VCSEL.

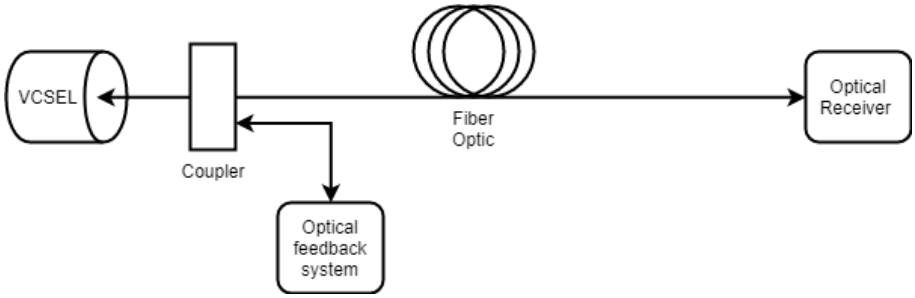

Figure 7.1: Further improvement of utilizing the optical feedback on the VCSEL properties that could applied.

Another further improvement can be to apply Digital Pre-Distortion (DPD) to overcome the nonlinearity of the VCSEL.

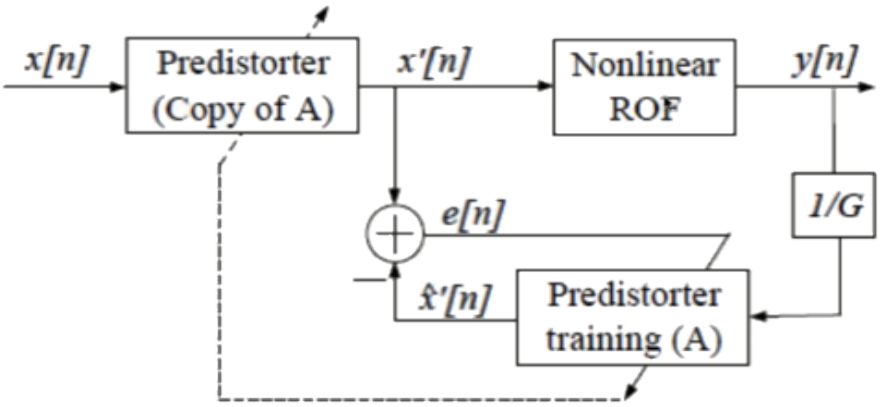

Figure 7.2: Apply DPD to decrease the nonlinearity.

Bibliography

[1] "Ericsson Mobility Report," Ericsson AB, Tech. Rep., November 2018

[2] D. M. Fye, "Design of fiber optic antenna remoting links for cellular radio applications," in 40th IEEE Conference on Vehicular Technology, May 1990, pp. 622-625.

[3] A. J. Cooper, "'fibre/radio' for the provision of cordless/mobile telephony services in the access network," Electronics Letters, vol. 26, no. 24, pp. 2054-2056, Nov 1990.

[4] A. J. Seeds and K. J. Williams, "Microwave photonics," J. Lightw. Technol, vol. 24, no. 12, pp. 4628-4641, Dec 2006.

[5] A. Nirmalathas, P. A. Gamage, C. Lim, D. Novak, and R. Waterhouse, "Digitized radio-over-fiber technologies for converged optical wireless access network," J. Lightw. Technol, vol. 28, no. 16, pp. 2366-2375, Aug 2010

[6] Shieh W, Yang Q, Ma Y. 107 Gb/s coherent optical OFDM transmission over 1000-km SSMF fiber using orthogonal band multiplexing. Opt Express 2008;16:6378–86.

[7] Jansen SL, Morita I, Tanaka H. 10 x 121.9-Gb/s PDM-OFDM transmission with 2-b/s/Hz spectral efficiency over 1000 km of SSMF. In: Opt. Fiber Commun. Conf., paper no. PDP2. San Diego; 2008.

[8] Bulow H. Electronic dispersion compensation. In: Opt. Fiber Commun. Conf., paper no. OMG5. Anaheim, CA; 2007.

[9] Spinnler B, Hauske FN, Kuschnerov M. Adaptive equalizer complexity in coherent optical receivers. In: Eur. Conf. Opt. Commun., paper no. We.2.E.4. Brussels, Belgium; 2008.

[10] Noe´ R. Phase noise tolerant synchronous QPSK/BPSK baseband type intradyne receiver concept with feedforward carrier recovery. J Lightwave Technol 2005;23:802–8.

[11] Savory SJ, Gavioli G, Killey RI, Bayvel P. Electronic compensation of chromatic dispersion using a digital coherent receiver. Opt Express 2007;15:2120–6.

[12] Ip E, Lau APT, Barros DJF, Kahn JM. Coherent detection in optical fiber systems. Opt Express 2008;16:753–91.

[13] Shieh W, Yi X, Ma Y, Yang Q. Coherent optical OFDM: Has its time come? [Invited]. J Opt Networking 2008;7:234–55.

[14] Shieh W, Djordjevic I. place=Burlington, MA, OFDM for optical communications, publisher:Academic Press/Elsevier, year:2010

[15] Hara S, Prasad R. Multicarrier Techniques for 4G Mobile Communications. Boston: Artech House; 2003.

[16] Hanzo L, Munster M, Choi BJ, Keller T. OFDM and MC-CDMA for Broadband Multi-User Communications, WLANs and Broadcasting. New York: Wiley; 2003.

[17] Yi X, Shieh W, Ma Y. Phase noise on coherent optical OFDM systems with 16-QAM and 64-QAM beyond 10 Gb/s. In: Eur. Conf. Opt. Commun., paper no. 5.2.3. Berlin, Germany; 2007.

[18] Takahashi H, Amin AA, Jansen SL, Morita I, Tanaka H. 8 * 66.8-Gbit/s coherent PDM-OFDM transmission over 640 km of SSMF at 5.6-bit/s/Hz spectral efficiency. In: Eur. Conf. Opt. Commun., paper no. Th.3.E.4. Brussels, Belgium; 2008.

[19] Lowery AJ, Wang S, Premaratne M. Calculation of power limit due to fiber nonlinearity in optical OFDM systems. Opt Express 2007;15:13282–7.

[20] Nazarathy M, Khurgin J, Weidenfeld R, et al. Phased-array cancellation of nonlinear FWM in coherent OFDM dispersive multi-span links. Opt Express 2008;16:15777–810.

[21] Pollet T, Van Bladel M, Moeneclaey M. BER sensitivity of OFDM systems to carrier frequency offset and Wiener phase noise. IEEE Trans Commun 1995;43:191–3.

[22] Armstrong J. Analysis of new and existing methods of reducing intercarrier interference due to carrier frequency offset in OFDM. IEEE Trans Commun 1999;47:365–9.

[23] 3GPP TS36211, Physical Channels and Modulation.

[24] Xin Yu, Yu Guanghui, Yan Xiao, Yang Zhen, Xu Jun, Gao Bo. ZTE Corporation Shenzhen,P .R. China

[25] D. Johnson, “The 5G Dilemma: More Base Stations, More Antennas—Less Energy?,” IEEE Spectrum: Technology, Engineering, and Science News, 03-Oct-2018. [Online]. Available: https://spectrum.ieee.org/energywise/telecom/wireless/will-increased-energy-consumption-be-the-achilles-heel-of-5g-networks. [Accessed: 08-Aug-2019].

[26] D. Wake, "Microwave and millimetre-wave photonics for telecommunications," in Microwave photonics, from components to applications and systems, A. Vilcot, B. Cabon, and J. Chazelas ed., Kluwer Academic Publishers, Boston, USA, 2003.

[27] C. Carlsson, H. Martinsson, and A. Larsson, “High performance microwave link using a multimode VCSEL and a high-bandwidth multimode fiber,” in Proc. Microwave Photonics (MWP’01), Long Beach, CA, Jan. 2002, pp. 81–84.

[28] G. Morthier and P. Vankwikelberge, Handbook of Distributed Feedback Laser Diodes. Boston, MA: Artech House, 1997.

[29] J. S. Gustavsson, A. Haglund, C. Carlsson, J. Bengtsson and A. Larsson, "Harmonic and intermodulation distortion in oxide-confined vertical-cavity surface-emitting lasers," in IEEE Journal of Quantum Electronics, vol. 39, no. 8, pp. 941-951, Aug. 2003. doi: 10.1109/JQE.2003.814376. http://ieeexplore.ieee.org/stamp/stamp.jsp?tp=&arnumber=1211139&isnumber=27261

[30] R. Schatz, “Dynamics of spatial hole burning effects in DFB lasers,” IEEE J. Quantum Electron., vol. 31, pp. 1981–1993, 1995.

[31] R. Paschotta, article on ’spatial hole burning’ in the RP Photonics Encyclopedia, https://www.rp-photonics.com/spatial_hole_burning.html. accessed on 2019-08-13

[32] T. E. Darcie, “Subcarrier multiplexing for lightwave networks and video distribution systems,” IEEE J. Select. Areas Commun., vol. 8, pp. 1240–1248, 1990.

[33] K. Y. Lau and A. Yariv, “Intermodulation distortion in a directly modulated semiconductor injection laser,” Appl. Phys. Lett., vol. 45, no. 10, pp. 1034–1036, 1984.

[34] T. E. Darcie, R. S. Tucker, and G. J. Sullivan, “Intermodulation and harmonic distortion in InGaAsP lasers,” Electron. Lett., vol. 21, no. 16, pp. 665–666,

1985.

[35] L. A. Coldren and S. W. Corzine, Diode laasers and photonic integrated circuits, John Wiley & Sons, New York, USA, 1995.

[36] Carlsson, C. (2003). Design and evaluation of vertical cavity surface emitting lasers for microwave applications. Doktorsavhandlingar vid Chalmers Tekniska Hogskola. 1-55.

[37] Al Zaidi, Salam (2016) Optical and electrical characteristics of vertical-cavity surface-emitting lasers for free space optical communications. Doctoral thesis, Northumbria University.

[38] R. S. G. a. L. A. Coldren, "Sub-milliamp threshold vertical cavity laser diodes," Appl.Phys. Lett., vol. 16, pp. 1605-1607, 1991 1991.

[39] A. Valle and L. Pesquera, "Theoretical calculation of relative intensity noise of multimode vertical-cavity surface-emitting lasers," Quantum Electronics, IEEE Journal of, vol. 40, pp. 597-606, 2004.

[40] J. Liu, Z.-M. Wu, and G.-Q. Xia, "Dual-channel chaos synchronization and communication based on unidirectionally coupled VCSELs with polarization rotated optical feedback and polarization-rotated optical injection," Optics express, vol. 17, pp. 12619-12626, 2009.

[41] Y. Hong, P. Spencer, and K. Shore, "Wideband Chaos with Time-Delay Concealment in Vertical-Cavity Surface-Emitting Lasers with Optical Feedback and Injection," Quantum Electronics, IEEE Journal of vol. 4, pp. 236-242, Apr 2014.

[42] M. Sciamanna and K. Shore, "Physics and applications of laser diode chaos," Nature Photonics, vol. 9, pp. 151-162, 2015.

[43] A. Uchida, Optical communication with chaotic lasers: applications of nonlinear dynamics and synchronization. Saitama,Japan: John Wiley & Sons, 2012.

[44] Z. Qin and S. Azouigui, Analysis of coherence-collapse regime of semiconductor lasers under external optical feedback by perturbation method. France: InTech, 2012.

[45] E. Kapon, Semiconductor lasers I: fundamentals. San Diego, USA: Academic Press, 1999.

[46] K. I. Kallimani and M. J. O'Mahony, "Relative intensity noise for laser diodes with arbitrary amounts of optical feedback," Quantum Electronics, IEEE Journal of, vol. 34, pp. 1438-1446, 1998.

[47] L. A. Coldren, S. W. Corzine, and M. L. Mashanovitch, Diode lasers and photonic integrated circuits vol. 218: Wiley. com, 2012.

[48] H. Keang-Po, J. D. Walker, and J. M. Kahn, "External optical feedback effects on intensity noise of vertical-cavity surface-emitting lasers," Photonics Technology Letters, IEEE, vol. 5, pp. 892-895, 1993.

[49] S. Xiang, W. Pan, L. Yan, B. Luo, N. Jiang, and L. Yang, "Polarization properties of vertical-cavity surface-emitting lasers subject to feedback with variably rotated polarization angle," Applied optics, vol. 48, pp. 5176-5183, 2009.

[50] K. Panajotov, M. Sciamanna, I. Gatare, M. Arteaga, and H. Thienpont, "Nonlinear dynamics of vertical-cavity surface-emitting lasers," Advances in Optical Technologies, vol. 2011, pp. 1-16, 2011.

[51] H. Yanhua, J. Rui, P. S. Spencer, and K. A. Shore, "Investigation of polarization bistability in vertical-cavity surface-emitting lasers subjected to optical feedback," Quantum Electronics, IEEE Journal of, vol. 41, pp. 619-624, 2005.

[52] Y. Hong, J. Paul, P. S. Spencer, and K. A. Shore, "The effects of polarization resolved optical feedback on the relative intensity noise and polarization stability of vertical-cavity surface-emitting lasers," Journal of Lightwave Technology, vol. 24, pp. 3210-3216, 2006.

[53] D. Parekh, "Optical Injection Locking of Vertical Cavity Surface-Emitting Lasers: Digital and Analog Applications," 2012.

[54] Y. Hong, P. S. Spencer, and K. A. Shore, "Suppression of polarization switching in vertical-cavity surface-emitting lasers by use of optical feedback," Optics letters, vol. 29, pp. 2151-2153, 2004.

[55] K. D. Choquette, R. Schneider, K. L. Lear, and R. E. Leibenguth, "Gain-dependent polarization properties of vertical-cavity lasers," Selected Topics in Quantum Electronics, IEEE Journal of, vol. 1, pp. 661-666, 1995.

[56] J. M. Ostermann and R. Michalzik, "Polarization control of VCSELs," in VCSELs, ed: Springer, 2013, pp. 147-179.

[57] J.-W. Shi, C.-C. Chen, Y.-S. Wu, S.-H. Guol, C. Kuo, and Y.-J. Yang, "High-power and high-speed Zn-diffusion single fundamental-mode vertical-cavity surface-emitting lasers at 850-nm wavelength," Photonics Technology Letters, IEEE, vol. 20, pp. 1121-1123, 2008.

[58] J. Martin-Regalado, F. Prati, M. San Miguel, and N. Abraham, "Polarization properties of vertical-cavity surface-emitting lasers," Quantum Electronics,

IEEE Journal of, vol. 33, pp. 765-783, 1997.

[59] K. Panajotov, B. Ryvkin, J. Danckaert, M. Peeters, H. Thienpont, and I. Veretennicoff, "Polarization switching in VCSEL's due to thermal lensing," Photonics Technology Letters, IEEE, vol. 10, pp. 6-8, 1998.

[60] H. G. Schuster and K. Lüdge, Nonlinear laser dynamics: from quantum dots to cryptography: John Wiley & Sons, 2012.

[61] R. W. Tkach and A. R. Chraplyvy, "Regimes of feedback effects in 1.5- & #181;m distributed feedback lasers," Lightwave Technology, Journal of, vol. 4, pp. 1655-1661, 1986.

[62] K. Kikuchi and T. Okoshi, "Simple formula giving spectrum-narrowing ratio of semiconductor-laser output obtained by optical feedback," Electronics Letters, vol. 18, pp. 10-12, 1982.

[63] R. Tkach and A. Chraplyvy, "Linewidth broadening and mode splitting due to weak feedback in single-frequency 1.5 μm lasers," Electronics Letters, vol. 21, pp. 1081-1083, 1985.

[64] D. Lenstra, B. Verbeek, and A. Den Boef, "Coherence collapse in single-mode semiconductor lasers due to optical feedback," Quantum Electronics, IEEE Journal of, vol. 21, pp. 674-679, 1985.

[65] J. Paul, C. Masoller, Y. Hong, P. S. Spencer, and K. Alan Shore, "Impact of orthogonal optical feedback on the polarization switching of vertical-cavity surface-emitting lasers," JOSA B, vol. 24, pp. 1987-1994, 2007.

[66] S. Xiang, W. Pan, L. Yan, B. Luo, N. Jiang, K. Wen, et al., "Polarization degree of vertical-cavity surface-emitting lasers subject to optical feedback with controllable polarization," JOSA B, vol. 27, pp. 476-483, 2010.

[67] S. De, V. Pal, A. El Amili, G. Pillet, G. Baili, M. Alouini, et al., "Intensity noise correlations in a two-frequency VECSEL," Optics express, vol. 21, pp. 2538- 2550, 2013.

[68] A. Quirce, A. Valle, C. Giménez, and L. Pesquera, "Experimental study of relative intensity noise of multimode vertical-cavity surface-emitting lasers," in SPIE Photonics Europe, 2010, pp. 772024-772024-11.

[69] S. Yu, "Nonlinear dynamics of vertical-cavity surface-emitting lasers," Quantum Electronics, IEEE Journal of, vol. 35, pp. 332-341, 1999.

[70] C. H. Cox III, E. I. Ackerman, G. Betts, and J. L. Prince, "Limits on the performance of RF-over-fiber links and their impact on device design," Microwave

Theory and Techniques, IEEE Transactions on, vol. 54, pp. 906-920, 2006.

[71] H.-F. Liu and W. F. Ngai, "Nonlinear dynamics of a directly modulated 1.55 μm InGaAsP distributed feedback semiconductor laser," Quantum Electronics, IEEE Journal of, vol. 29, pp. 1668-1675, 1993.

[72] G. Shtengel, H. Temkin, P. Brusenbach, T. Uchida, M. Kim, C. Parsons, et al., "High-speed vertical-cavity surface emitting laser," Photonics Technology Letters, IEEE, vol. 5, pp. 1359-1362, 1993.

[73] G. S. Gordon, M. J. Crisp, R. V. Penty, and I. H. White, "High-order distortion in directly modulated semiconductor lasers in high-loss analog optical links with large RF dynamic range," Lightwave Technology, Journal of, vol. 29, pp. 3577- 3586, 2011.

[74] B. Kuntsevich, A. Pisarchik, and V. Kononenko, "Nonlinear dynamics of a directly modulated semiconductor laser with cavity detuning," Optical and quantum electronics, vol. 37, pp. 675-693, 2005.

[75] M. Giudici, S. Balle, T. Ackemann, S. Barland, and J. R. Tredicce, "Polarization dynamics in vertical-cavity surface-emitting lasers with optical feedback: experiment and model," JOSA B, vol. 16, pp. 2114-2123, 1999.

[76] X.-F. Wang, G.-Q. Xia, and Z.-M. Wu, "Theoretical investigations on the polarization performances of current-modulated VCSELs subject to weak optical feedback," JOSA B, vol. 26, pp. 160-168, 2009.

[77] S. Li, "UWB Radio-over-Fiber System Using Direct Modulated VCSEL," 2007.

[78] X. Li, W. Pan, B. Luo, D. Ma, N. Li, and Y. Wang, "Suppressing nonlinear dynamics induced by external optical feedback in vertical-cavity surfaceemitting lasers," Optics & Laser Technology, vol. 37, pp. 438-443, 2005.

[79] K. Panajotov, M. Virte, M. Sciamanna, M. Tlidi, and H. Thienpont, "Nonlinear dynamics of Vertical-Cavity Surface-Emitting Lasers: deterministic chaos, random number generation and chaotic cavity solitons," 18th INTERNATIONAL SCHOOL ON CONDENSED MATTER PHYSICS, vol. 22, p. 34, 2014.

[80] G. Morthier and P. Vankwikelberge, Handbook of distributed feedback laser diodes: Artech House, 2013.

[81] A. Valle, J. Sarma, and K. Shore, "Spatial holeburning effects on the dynamics of vertical cavity surface-emitting laser diodes," Quantum Electronics, IEEE Journal of, vol. 31, pp. 1423-1431, 1995.